NORTHWESTERN UNIVERSITY

Nanoscale Characterization of Oxide Materials and Interfaces for High Performance Lithium Ion Batteries

A DISSERTATION

SUBMITTED TO THE GRADUATE SCHOOL

IN PARTIAL FULFILLMENT OF THE REQUIREMENTS

for the degree

DOCTOR OF PHILOSOPHY

Field of Materials Science and Engineering

By

Fernando Cuauhtli Castro

EVANSTON, ILLINOIS

December 2018

ABSTRACT

Nanoscale Characterization of Oxide Materials and Interfaces for High Performance Lithium Ion Batteries

Fernando Cuauhtli Castro

The start of the 21^{st} century brought the sweeping proliferation of portable electronics such as laptops, tablets, and smartphones. These technologies were largely enabled by advances in energy storage methods – lithium ion batteries in particular. Society's push for more advanced energy storage applications, such as electric vehicles, stresses the need for lithium ion batteries with improved performance and availability. Reaching new performance heights largely requires developing new materials for the battery electrodes, and understanding the impact of their crystal structure and materials chemistry on the electrochemical phenomena which directly affect battery performance.

The work in this dissertation probes how nanoscale changes to the structure and composition of metal oxide electrode materials drive increases in charge capacity. The challenges and complications these changes bring to the materials system are also examined, especially when undergoing reduction-oxidation reactions due to lithiation and

delithiation. These challenges are most prominent in materials that undergo a conversion reaction with lithium, resulting in large charge capacities but limited reversibility and significant morphology changes. Multilayer nickel/nickel oxide structures are utilized as an anode model system and testing ground for controlling structural evolution, lithiation mechanisms, and kinetics of the conversion reaction. Key to these studies is the deep implementation of electron microscopy imaging and spectroscopy techniques for the characterization of chemical and structural evolution, and their correlation with surface-sensitive x-ray techniques. These same techniques are applied to studying oxygen coordination and electronic structure in lithium-rich intercalation cathode materials. The reactivity and participation of oxygen in charge compensation mechanisms during electrochemical (de)lithiation is carefully considered. Furthermore, an extended methodology of electron energy loss spectroscopy is explored for the study of lithium ion battery materials when limited by constraints in electron beam sensitivity or sample thickness and morphology. Overall, these studies illustrate the diverse and complex electrochemical reactivity of metal oxides that together deepen our understanding of the atomic-scale and nano-scale structure-composition effects on phenomena critical to battery performance.

Acknowledgements

There are many, many people who contributed to my graduate studies that I would like to thank and acknowledge. First of all, I want to greatly thank Professor Vinayak P. Dravid. As a member of his research group, he provided not only the necessary resources and scientific guidance throughout my graduate student tenure, but also had confidence in my abilities since day one. My time as a member of Professor Dravid's research group was truly a special and worthwhile opportunity. I would also like to thank the members of my committee – Professor Sossina Haile, Professor Michael Bedzyk, and Dr. Paul Fenter – for their time, effort, and dedication to the development of young scientific minds such as my own. Paul also acted as director of the Center for Electrochemical Energy Science (CEES), which funded most of my work. I really appreciate his efforts as director for making my research possible, and the additional support he provided to myself and other CEES graduate students.

I have had several significant collaborators during graduate school that deserve acknowledgement, which included both Professor Michael Bedzyk and Dr. Paul Fenter. Moreover, I am fortunate to have been part of the excellent work done by Dr. Guena Evmenenko, Dr. Liang Li, Dr. Lingzi Sang, and Dr. Eungje Lee. Several other CEES graduate students and collaborators deserve high praise, including Robert Warburton, Kimberly L. Bassett, Bruno Nicolau, Dr. Maria Chan, Dr. Chris Johnson, and Dr.

Michael Thackeray. From Northwestern, I would like to thank Dr. Yuan Li, Dr. Vikas Nandwana, Dr. Bruce Buchholz, and Taegon Oh.

One of the primary themes in this dissertation is the use of electron microscopy to solve materials challenges. Many people helped me develop my expertise in these techniques, provided assistance throughout the years, and did all the behind-the-scenes work to keep the facilities up and running. They include Dr. Shuyou Li, Dr. Ben Myers, Karl Hagglund, Eric Roth, Dr. Rainer Bleher, Tirzah Abbott, Dr. Xinqi Chen, Dr. Kai He, and Dr. Xiaobing Hu. Extra-special thanks goes to Dr. Jinsong Wu, who throughout my time at Northwestern was a teacher, mentor, colleague, group-mate, collaborator, sponsor, and technical guru. I wish him the best as he leaves Northwestern, and hope he knows that he made a lasting impression on myself and countless other students. Several post-docs from the Dravid group and EPIC played similar multifunctional roles in my graduate career, and need to be recognized: Dr. Fengyuan Shi, Dr. Sungkyu Kim, Dr. Yaobin Xu, Dr. Qianqian Li, and Dr. Hee Joon Jung. Of course, Dravid group and NU*ANCE* staff members all played an important role in keeping everyone afloat and I cannot thank them enough for all the help: Mary Pat Doyle, Chad Goeser, Ray Bailey, Joyce Park, and Amy Morgan.

Beyond everyone I have already mentioned, I am eternally thankful for all the friends I made during my time in the Dravid group and at Northwestern. To start, I want to thank everyone in the Dravid group, past and present, for fostering a friendly and collaborative research environment. The students and post-docs as a whole are what make our group great. Furthermore, I really want to thank everyone who has been an office mate in Cook 1137 – hands-down had the best office mates I could have ever asked for over many years.

This includes Dr. Fengyuan Shi, Dr. Qianqian Li, Dr. Poya Yasaei, Dr. Roberto dos Reis, César Villa, Jann Grovogui, and Xiaomi Zhang. I especially want to thank Xiaomi for being my oldest friend in the group and definitely my largest sounding board in the group as well.

I also want to thank the close friends I made outside the group: Nick Sather (Dr. Sather, by the time of my defense!), Janak Thapa, (newly!) Dr. Sam Miller, and (newly!) Dr. Matthew Peters. Thanks for all of the camaraderie, Friday lunches, football games, podcast-talk, and late-night debauchery. I also want to thank the continued friendship of my whole UChicago crew, especially Nolan Skochdopole and James Elliott.

Finally, I want to give the deepest thanks to my family, who have been with me, known me, and loved me the longest. My parents – Fernando and Cynthia. My siblings – Quetzalli and Jonathan. My uncle – Guero. The memory of the grandparents that helped raise me so much – Mamá Judy y Papá Rene. And all of the rest of my extended family, back in Mexico. It took a lot of people and circumstances to get me here, and I hope that this degree is one small way of proving that it was all worth it. The entire Lee family also deserves thanks for their support and encouragement during my time in graduate school – especially Fei, Denise, and Li-Lin Lee. I needed the strength of two families at times, and they were always there, too.

Finally (actually finally), I want to thank Gigi Lee. The 11+ years we have been together feel like no time at all. Without your love, support, empathy, and patience, I would not have made it to this point. I love you so deeply.

Dedication

Para mi familia, y para Gigi. ¡Los quiero a todos!

For my family, and for Gigi. I love you all!

Table of Contents

List of Tables

List of Figures

CHAPTER 1

Introduction: The Materials Science of Lithium Ion Batteries and The Role of Electron Microscopy in their Study

1.1. Chapter Overview

Lithium ion batteries have an important place in society as the power source for portable technology and the enablers of new sustainability efforts. However, their capabilities fall short of the needs of many new applications. Improving lithium ion batteries beyond the status-quo requires a deep understanding of the materials science and electrochemistry affecting battery performance, as well as the complex interactions between each individual battery component. The work presented in this dissertation aids to expand this understanding by focusing on the evolving nanoscale structure and composition of lithium ion battery materials. This chapter provides the necessary background and context of the field of lithium ion batteries – the options in available materials, the necessary trade-offs between performance and practicality, and how lithium ion batteries can be studied at the nanoscale.

In particular, Sections 1.2 and 1.3 provide a basic introduction to the history and essential components of lithium ion batteries. Sections 1.4 and 1.5 introduce various classes of anode and cathode materials, and discuss how the structure and chemical composition of these materials broadly affect their performance in a battery. A comparison of the different materials is also provided to motivate the work presented in this dissertation.

Finally, Section 1.6 provides an overview of electron microscopy, the materials characterization technique of choice for analyzing the materials discussed within.

1.2. Historical Origins of Energy Storage and Lithium Ion Batteries

Using batteries as a method of energy storage relies on their ability to convert stored chemical energy into electrical energy, and vice-versa. History places the first discovery of this energy storage phenomenon in the early 1800s, as Alessandro Volta created a 'voltaic pile' of zinc, copper, and salt water soaked cloth that generated a continuous source of electricity.[1] This was in fact, an electrochemical cell that relied on the chemical dissolution of zinc ions into the electrolyte solution and transport of electrons from the zinc disc (i.e. electrode) to the copper disc.

Countless iterations and improvements to similar electrochemical cells were made as the field of electrochemistry evolved in the centuries since then. Most important was the achievement of electrochemical cells that could have their chemical reaction reversed, thus enabling multiple-use batteries that could be charged and discharged. Some notable chemistries still used today include lead-acid, nickel-cadmium, and nickel-metal hydride batteries.[2,3] However, the greatest example of rechargeable batteries to date is the lithium ion battery, which is the primary focus of this dissertation. First actualized in the late 1970s by John Goodenough *et al.*, the lithium ion battery was not commercialized until 1997 by the Sony corporation.[4–6] These kinds of batteries boast the ability to store a relatively large amount of energy, be charged and discharged hundreds of times, and be housed within a low-volume and low-weight package. Since then, the field of lithium ion

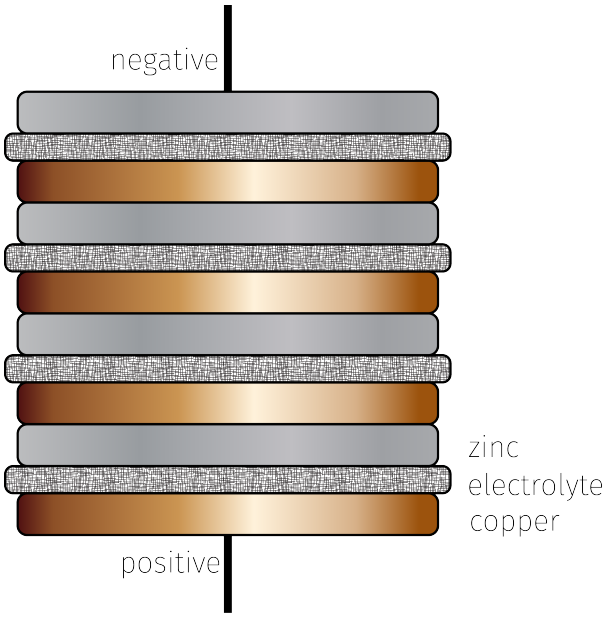

Figure 1.1. Diagram of Volta's Voltaic Pile

battery research has exploded, as new materials systems are explored to advance battery technology and match the increasing demands of their applications.[7–20]

1.3. Functional Properties of Lithium Ion Batteries

1.3.1. Essential Components and Chemistry

All batteries, from Volta's electrochemical cell to the most advanced lithium ion battery, contain three key components:

- cathode
- anode
- electrolyte

These components are made of materials that undergo chemical reactions to generate positively-charged ions and electrons that can power a device. In Volta's pile, the copper

and zinc act as the cathode and anode, respectively. The transport of copper and zinc ions into and out of the electrolyte solution generated electrons that flowed through a circuit.

The first commercialized lithium ion battery system consisted of a $LiCoO_2$ cathode, a graphitic carbon anode, and a electrolyte consisting of a mix of organic liquids.[5] When this battery is charged, electron flow from the power source causes lithium ions to be removed from the cathode and transported to the anode, where they are stored. As a result, this 'charge' reaction converts input electrical energy into stored chemical energy. The reactions occurring at the cathode and anode during cycling are shown in Equation 1.1 and Equation 1.2, respectively. The reverse 'discharge' reaction happens spontaneously when the battery is connected to a complete electrical circuit. The lithium ions leave the anode and return to the cathode. At the same time, electrons travel through an eternal circuit to maintain charge balance, and can be used to do useful work and power an external device.

$$Cathode : \mathrm{LiCoO_2} \underset{\text{discharge}}{\overset{\text{charge}}{\rightleftharpoons}} \mathrm{Li_{1-x}CoO_2} + x\,\mathrm{Li^+} + x\,\mathrm{e^-} \tag{1.1}$$

$$Anode : \mathrm{C_6} + x\,\mathrm{Li^+} + x\,\mathrm{e^-} \underset{\text{discharge}}{\overset{\text{charge}}{\rightleftharpoons}} \mathrm{Li_xC_6} \tag{1.2}$$

Figure 1.2 illustrates the full working battery system, highlighting the ion and electron transport directions towards the different electrodes during charge and discharge cycles.

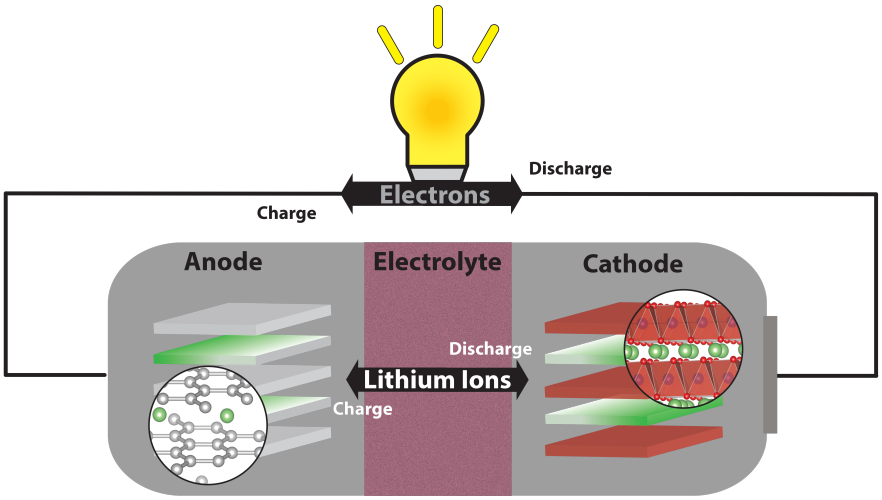

Figure 1.2. Schematic of a Lithium Ion Battery, showing the flow of electrons and Li^+ ions during the charge and discharge cycles.

1.3.2. Key Performance Metrics

There are several important metrics needed to understand the efficacy of the chemical reactions at the anode and cathode, along with overall battery performance. All of these metrics and properties described are intrinsically linked to the choice of materials for use in the anode, cathode, and electrolyte of the battery. The key goal in battery research is to develop new or improved materials with enhanced properties while maintaining compatibility with other important components.

The following sections highlight some of the most pertinent materials properties and metrics.

Electrode Potential. The electrode potential of a material (sometimes referred to simply as its voltage), is measured in volts (V) and describes the energy per unit charge that is available to move charge from one electrode to the other. The potentials are measured for different half-cell reactions describing the reduction-oxidation process of gaining or

losing an electron, and are typically measured versus the standard hydrogen electrode (SHE). However, in the field of lithium ion batteries, electrode potentials are reported with respect to the Li^+/Li half-cell reaction, which has a potential of -3.04 V versus the SHE.[21]

Knowledge of the electrode potential allows one to calculate the change in Gibbs free energy of the system, which grants insight into whether the half-cell reaction of interest will occur spontaneously. This equation is:

$$dG = -nFE \tag{1.3}$$

where dG is the change in Gibbs free energy, n is the number of moles of electrons in the half-cell reaction, F is Faraday's constant, and E is the electrode potential.

The total cell potential of the lithium ion battery is determined by the difference in electrode potentials of the cathode and the anode.

$$E_{cell} = E_{cathode} - E_{anode}. \tag{1.4}$$

The amount of energy stored by a battery is directly proportional to the total cell potential:

$$Energy = Capacity \times E_{cell} \tag{1.5}$$

As such, maximizing the cell potential will maximize the amount of energy that is stored by the lithium ion batteries. Lithium ion battery cathode materials typically have higher potentials vs. lithium while anodes have very low potentials. For example, $LiCoO_2$ has a potential of 4 V vs. lithium and graphite has a potential of 0.2 V vs. lithium for a 3.8 V cell potential overall.[5,22]

The electronegativity of the individual elements and overall composition of the electrode compound affect its electrode potential. Tuning materials structure and composition to achieve improved cell potentials and higher energy storage is one of the challenges facing the battery field.

Charge Capacity and Energy Capacity. The charge capacity of a battery describes how many Li^+ ions can be inserted and extracted from the different electrodes during charge and discharge. This is directly related to electrode composition and crystal structure. It is usually described as either the amount of charge per weight of electrode known as specific capacity or gravimetric capacity, with units mAh/g. However, capacity values are also at times expressed in terms of volume, mAh/L, which may be the more important parameter based on the battery application.

It is possible to calculate the theoretical charge capacity of a material based on its composition:[23]

$$Capacity_{theoretical} = \frac{nF}{3.6 \times M} \tag{1.6}$$

where n is the number of Li per formula unit, F is Faraday's constant, and M is the molar weight of the electrode materials.

Typical gravimetric charge capacities for commercialized lithium ion batteries lie within the range of 100 to 200 mAh/g.[24] Per Equation 1.5, the charge capacity directly affects the energy capacity of battery, which are described either in Wh/kg or Wh/L.

Charge Rate. The charge rate is used to describe how quickly the battery can be charged or discharged, i.e. how quickly Li^+ ions can be inserted and extracted from the electrode. Typically, batteries can be charged at different rates, depending on the potential and current being used to charge or discharge the battery. The rate, commonly referred to as C-rate, is based on the notation of how quickly the battery is charged or discharged compared to 1 hour. For example, a battery that is completely charged in 1 hour was charged at a rate of 1C, while a battery charged in 30 minutes has a rate of 2C. Conversely, a battery charged in 2 hours has a rate of 0.5C.

Often, the materials properties of the electrode dictate the tolerance for fast or slow charge rates. Electronic and ionic conductivites of the different electrode materials play a key role in determining the respective diffusivity values and a sustainable charge rate, in addition to the kinetics of processes and transport at electrode-electrolyte interfaces. Very high charge rates typically result in lowered capacity and cycling lifetimes due to unwanted side reactions or the formation of interfaces which inhibit ion transport.[25,26] It is worth noting that the ionic conductivity of the electrolyte, and its potential window for stability, also affect which charge rates result in the best performance.

Cycling Lifetime and Reversibility. The cycling lifetime and reversibility of the battery represent how many charge and discharge cycles the battery can undergo before significant degradation. This lifetime is affected both by the conditions which the battery is charged, such as charge rate, but also depends on the electrode materials which may be

more or less stable under certain conditions. Cell degradation can occur in many ways, including capacity fade, voltage fade, interfacial instabilities, mechanical failure, loss of electrical contact, thermal runaway, etc.[25,27–29] These degradation mechanisms are often interrelated and depend on complex processes due to both electrode/electrolyte choice and the parameters of battery usage. Understanding what changes in composition or structure lead to the different degradation mechanisms in different materials is yet another major challenge facing lithium ion battery materials.

Often, the coulombic efficiency of a cell is reported alongside the cycling lifetime. This efficiency describes the total amount of charge extracted and re-inserted into the electrodes during the charge and discharge cycles. Current commercialized lithium ion batteries have cycling lifetimes of hundreds of cycles and coulombic efficiencies $> 99\%$. It is imperative for any new material to have cycling lifetime performance on par with this benchmark if it is to have commercial success.

Safety. The safety of lithium ion batteries is a qualitative metric, and is determined by the choices of both electrodes and the electrolyte. The largest safety concerns in batteries root from the choice of electrolyte – usually based on a mix of carbonates – which are highly flammable and have flash points close to room temperature.[3] Physical or thermal abuse of the lithium ion battery can lead to dangerous exothermic reactions that ignite the electrolyte. Mitigating these safety issues requires improved engineering of the battery packaging, but also alternative materials choices. Solid electrolyte materials are actively researched as a safer non-flammable alternative to liquid electrolytes.[30,31,20] Furthermore, anode and cathode materials must be designed to minimize structural and

chemical degradation that can lead to unwanted side-reactions and interactions with the flammable electrolyte.

Sustainability. One of the challenges that lithium ion batteries are likely to face in the future is their ability to be a sustainable source of battery storage. Many of the transition metals commonly used in the cathode materials, such as cobalt, are expensive and rare elements. Lithium itself can only be extracted from rare salt brines in only a few places on earth. As a result, many reports forecast increasing difficulty in extracting the necessary elements for lithium ion batteries and subsequent increases in the cost of raw materials.[8,32,33] Many cutting-edge materials focus on using cheaper and more abundant transition metals, such as iron. Furthermore, alternatives to lithium ion chemistries are being explored, such as sodium ion and magnesium ion chemistry.[34–36]

1.4. Insertion Materials for Lithium Ion Batteries

Battery performance is profoundly affected by the choice of materials for the battery electrodes. The chemical composition and crystal structure of each electrode impacts the reduction-oxidation reaction that converts chemical energy to electrical energy. This section provides background to the relationship between material composition, structure, and overall battery performance for the intercalation batteries described in Equations 1.1 and 1.2.

1.4.1. Lithium Ion Chemistry

The heart of battery chemistry and functionality lies within the choice of cation participating in the key reduction-oxidation reaction. Lithium is the smallest, lightest and

most electropositive metal atom that naturally exists, and the use of Li^+ ions in batteries has a profound effect.[18] Their electropositive nature and use as pure metal anodes would maximize the cell potential and energy storage in batteries. Furthermore, their small size and light weight result in lighter-weight and smaller-volume materials and batteries, providing them a distinct advantage over older battery technology and enabling their use in portable electronics. The small size of the ions also means that Li^+ can be stored in various crystallographic sites of the anode and cathode structure.

Using Li^+ ions as the key battery chemistry also comes with a few distinct disadvantages. Its high reactivity makes the battery system prone to unwanted side reactions during cycling of the battery, and increases the sensitivity of the battery materials to air and moisture exposure.[37,38] Lithium is also a scarce element and faces the sustainability challenges discussed in Section 1.3.2.

1.4.2. Lithium Insertion Cathodes

Layered Intercalation Materials. As mentioned, the battery performance of a material is intrinsically linked to the crystal structure of the electrode materials. Most commercialized lithium ion batteries operate using the insertion chemistry described in Section 1.3.1. The class of insertion cathodes most commonly used have a 'layered' crystal structure. The materials, typically transition metal oxides, have layers of metal-oxygen octahedra forming closed-packed oxygen arrays. These layers of metal oxides are held together by van der Waals forces, and have a large enough interlayer gap to enable insertion and storage of lithium. Insertion materials with the layered structure described are often referred to specifically as 'intercalation' materials.

A prominent example of an intercalation material is $LiCoO_2$ (space group $R\overline{3}m$) as seen in Figure 1.3, which has layers of Co-O octahedra with a distinct interlayer spacing of 4.62 Å.[39] $LiCoO_2$ has a $/sim4$ V potential and, as the material is discharged and charged, Li^+ ions are removed and inserted from the interlayer region of the crystal structure. The 2-dimensional planar structure of the interlayer region allows diffusion of ions along several crystallographic directions contained within the plane, which enable relatively high diffusivity values of Li^+ on the order of $10^{-9}cm^2/s$.[6]

Although $LiCoO_2$ has a theoretical charge capacity of 270 mAh/g, which corresponds to complete lithiation and delithiation of the material (i.e. cycling between CoO_2 and $LiCoO_2$), this charge capacity is not achievable in practice. In practice, only about 0.5 Li per formula unit of $LiCoO_2$ can be removed (i.e. reversibility only exists between $LiCoO_2$ and $Li_{0.5}CoO_2$) before structural degradation to a monoclinic symmetry occurs and the capacity is dramatically reduced. As a result, the usable charge capacity of $LiCoO_2$ is only 140 mAh/g.[40]

Olivine and Spinel Insertion Structures. Reversible insertion and extraction of Li^+ ions from empty sites is possible in materials that do not have a 'layered' crystal structure. Olivine structured materials, such as $LiFePO_4$ (space group Pnma), have a 3-dimensional oxygen packing structure as opposed to 2-dimensional packing in $LiCoO_2$. $LiFePO_4$ also has edge-shared octahedra with PO_4 tetrahedra that form 1-dimensional tunnels oriented along the [010] directions seen in Figure 1.3. The Li^+ ions occupy and diffuse through these tunnels, and reversible cycling of up to 0.6 Li formula units is possible, giving $LiFePO_4$ a specific capacity of 110 mAh/g.[41] This is a lower capacity than $LiCoO_2$, and lithium diffusivity is lower in $LiFePO_4$ due to the 1-dimmensional transport pathways, on the order

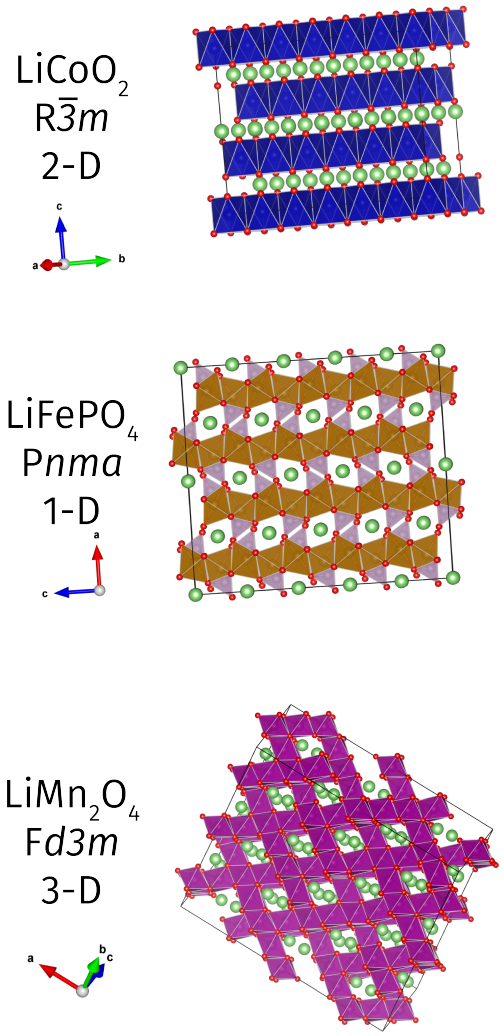

Figure 1.3. Crystal Structures of $LiCoO_2$, $LiFePO_4$, and $LiMn_2O_4$

of 10^{-14}cm^2/s.[42] However, the $LiFePO_4$ cathode has a lower 3.5 V electode potential which allows for more stable cycling with the common organic electrolytes. Usage of Fe instead of Co also makes the electrode material much cheaper and environmentally safer.[41]

Another common crystal structure is the spinel structure (space group F$d3m$),with $LiMn_2O_4$ being one of the most well-known spinel cathode materials. $LiMn_2O_4$ is comprised of a cubic close packed oxygen network and 3-dimensional face-sharing metal oxide

octahedron framework.[43] Li^+ ions are present within this 3-dimensional structure and have diffusion pathways for insertion and extraction in each dimension, again shown in Figure 1.3. $LiMn_2O_4$ has a theoretical capacity of 150 mAh/g, of which 120 mAh/g is achievable in practice.[44] It's diffusivity, despite having 3-d diffusion pathways, is approximately $10^{-11}cm^2/s$– lower than $LiCoO_2$ but higher than $LiFePO_4$.[45] However, it provides more stable cycling performance than $LiCoO_2$, and at a potential of 4.2 V.[44]

1.4.3. Insertion Anodes

Commercialized battery systems also utilize anodes based on insertion chemistry, as described in Equation 1.2. This anode is almost always based on graphitic carbon, which allows intercalation of Li^+ ions in between individual graphene sheets. Li^+ is stored in sites above each C_6 honeycomb ring and forms LiC_6 in the fully lithiated state.[46] Carbon-based materials make excellent anode materials due to their exceedingly low potential of 0.2 V vs. Li/Li^+, which helps maximize the overall cell potential. Furthermore, they have a high theoretical capacity of 360 mAh/g, lithium diffusivities up to $10^{-7}cm^2/s$, high stability, and low cost.[45,47]

1.5. Electrode Materials Beyond Insertion Chemistry

Despite the level of commercialization reached by many of the insertion anodes and and cathodes discussed in the previous section, significant development is still needed to match the energy storage demands of the future. The materials and chemistry research in the field of lithium ion batteries aims towards improving all of the important metrics described in Section 1.3.2. However, increasing the charge capacity and energy capacity

of electrode materials is one of the largest needs for batteries to propagate new technology like electric vehicles and grid-scale storage.[48,49] Immense gains in charge capacity or energy capacity are possible using different chemistries beyond the insertion chemistry discussed so far. This section introduces some of these materials and chemistries.

1.5.1. Conversion Reaction Electrode Materials

An alternative choice to insertion materials are conversion reaction materials, which undergo a fundamentally different chemical reaction than intercalation. Rather than insertion and extraction of Li^+ ions from empty lattice sites, conversion materials have a full chemical reduction-oxidation reaction between the active material and Li^+ ions. This reaction has the general form:

$$MX + nLi^+ + ne^- \underset{\text{charge}}{\overset{\text{discharge}}{\rightleftharpoons}} M + Li_nX \tag{1.7}$$

where M is a metal species, X is the anion coordinated to the metal, and n represents the stoichiometric amount of lithium and electrons needed for the conversion reaction based on the oxidation state of the metal species. As Equation 1.7 shows, the MX compound reacts with Li^+ ions, forming a reduced metal species and a lithiated anion complex.[15] This general conversion reaction typically involves more than one Li^+ ion per formula unit of MX, thereby dramatically increasing the amount of energy storage possible. Theoretical charge capacities 2 - 5 times larger than intercalation materials are possible based on the chemical composition of the material. For example, CuF_2 has a

theoretical charge capacity of 528 mAh/g and MnO_2 has a theoretical capacity of 1233 mAh/g.[50]

A wide variety of cation and anion species can be used for the conversion reaction. These compounds typically use transition metals as the cation, which can coordinate to a wide variety of anions. Changing the composition of the transition metal or the anion effectively tunes the electrode potential vs. Li/Li^+, as described in Section 1.3.2. For example, fluorine is more electronegative than oxygen, and tends to have higher potentials vs. Li/Li^+. As a result, metal fluorides (3 - 4 V potentials) typically are studied as cathode materials. Metal oxides (1 - 2 V potentials) are typically studied as anode materials due to their low experimental potential (< 1 V), but could theoretically be used as either electrode type due to their intermediate potentials.[50–53]

The main challenges that come with the usage of conversion anodes are due to the intrinsic chemical reaction which occurs. Reduction of the MX compound typically results in a large and typically irreversible morphology change.[54,55] Moreover, Li_nX is often a species with limited reversibility due to its thermodynamic stability or worse conductivity, such as Li_2O, that can cause isolation of the metallic species from the rest of the system, causing capacity loss.[56] Moreover, the lithiated electrode typically sees significant volume expansion, often on the order of 100% or larger. These combined challenges result in systems that many times only demonstrate a large first-cycle capacity and their extended cycling occurs with significantly less charge.[15]

1.5.2. Lithium Metal Anodes

Lithium metal anodes are the holy grail of the battery field, as their utilization would enable lightweight batteries with the lowest electrode potential and extremely large storage capacities of up to 3860 mAh/g.[18] These electrodes would function through repeated plating and stripping of Li^+ ions onto the lithium metal anode. However, the lithium metal anode has severe problems with stability. Repeated cycling with a lithium metal anode causes growth of lithium metal dendrites, which pose severe safety risks as they can cause short-circuits and thermal runaway that ignites the flammable electrolyte.[57] Moreover, the chemical reactivity of lithium can lead to many unwanted side reactions that form passivating layers on the electrode, lowering the coulombic efficiency and severely limiting capacity over time.[58] The promise of an extremely high-performing anode material has kept researchers continually working on solutions towards minimizing the issues facing lithium metal anodes.[59–63]

1.5.3. Lithium Alloy Electrodes

It is possible to utilize certain electrode materials that undergo alloy reactions with lithium, rather than conversion or insertion. Some of the most prominent examples are Si and Sn-based anodes, which can be lithiated to various degrees. Equation 1.8 shows the example reaction for Si, where the amount of Li^+ ions able to be alloyed (x) can reach compositions of $Li_{4.4}Si$.[16]

$$\mathrm{Si} + \mathrm{xLi} \underset{\text{charge}}{\overset{\text{discharge}}{\rightleftharpoons}} \mathrm{Li_xSi} \tag{1.8}$$

This lithiated silicon anode can reach theoretical capacities of >3500 mAh/g, depending on the level of lithiation, but also comes with an enormous volume expansion of over 300%.[64] Repeated cycling of these electrodes causes particle fracture and significant capacity loss.[65] Controlling the degree of lithiation and volume expansion in these anodes is one of the most active fields of research on anode materials.[66]

1.5.4. Materials Summary

Figure 1.4 provides a graphical summary and comparison of the insertion and conversion electrode materials discussed, which are the primary focus of the dissertation. Each material class is plotted with respect to the specific capacity and electrode potentials attainable. Overall, conversion materials provide significantly higher charge capacities than insertion materials, but at more intermediate electrode potentials. They also lack the chemical stability and reversibility that provide the key advantage to lithium insertion electrode materials.

1.6. Electron Microscopy Studies of Lithium Ion Batteries

1.6.1. Overview of Electron Microscopy Techniques

Materials characterization of lithium ion batteries is quintessential to understanding changes that occur in the material during battery operation, how these changes affect electrochemical behavior and important performance metrics, and what strategies can be implemented to improve future performance. As such, it is necessary to identify materials crystal structure, morphology, and chemical composition at different degrees of lithiation

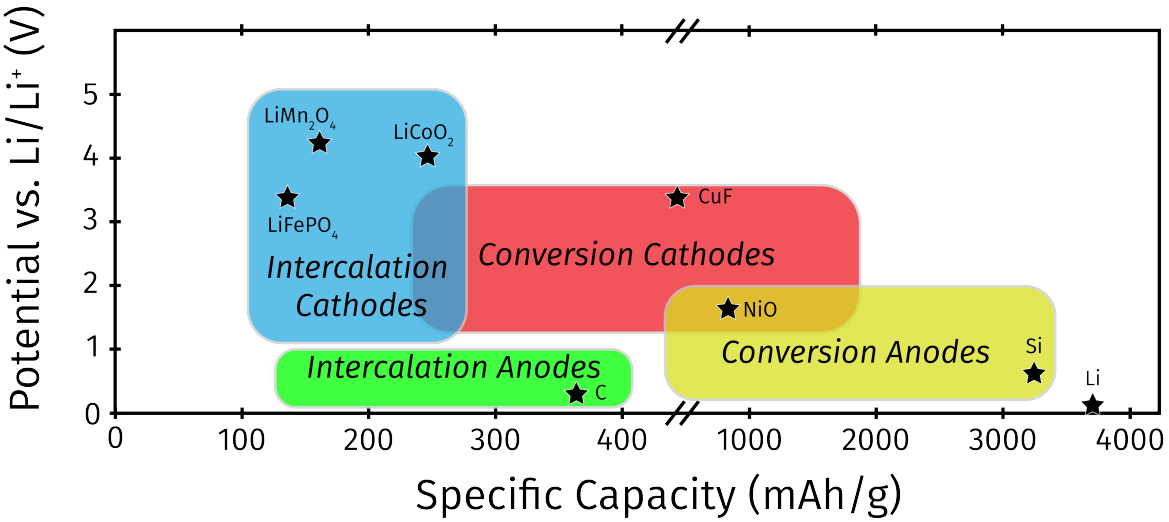

Figure 1.4. Plot of theoretical specific capacity vs. electrode potential for several electrode materials discussed. Figure was adapted from Reference [24].

and delithiation (i.e. states of charge). Often, the phenomena of interest occur at multiple length-scales – from the microscale down to the atomic scale. As a result, techniques that enable high spatial resolution analysis over a wide range of length-scales are very powerful. Electron microscopy characterization fits this bill perfectly, and a wide variety of tools are found in the electron microscopy toolset. Direct imaging of materials reveals key morphological features such as cracking, particle size, grain size, crystal defects, etc. Moreover, several imaging methods are utilized to highlight changes in composition or crystalline defects through different contrast mechanisms. Electron diffraction methods combined with imaging provides information of crystal structure and the spatial distribution of different structural phases. Chemical analysis methods are used to determine elemental presence and distribution in a sample. Electron microscopy in particular routinely conducts this work with sub-nanometer spatial resolution or even with sub-atomic spatial resolution if using an aberration-corrected instrument.

Other materials characterization techniques such as X-Ray Photoelectron Spectroscopy (XPS) and X-Ray Diffraction (XRD) are well-suited to providing bulk information on materials structure and composition, enabling more statistical information and higher through-put analysis. The main downside to these methods are that they can easily miss nanoscale inhomogeneities that can be vital for understanding battery performance. Electrochemical analysis, such as cyclic voltammetry (CV) can provide vital information regarding the reaction chemistry that cannot be ascertained via electron microscopy. However, no direct structure or composition information is provided.

Electron microscopy is a powerful tool and the primary technique utilized in this disseration. However, other materials characterization methods often provide beneficial correlative data and in many cases are necessary for fully solving the scientific problems at hand.

1.6.2. The Electron Microscopy Toolset: SEM, TEM, and STEM

There are three main types of electron microscopy that are used for materials characterization:

- Scanning Electron Microscopy (SEM)
- Transmission Electron Microscopy (TEM)
- Scanning Transmission Electron Microscopy (STEM)

The choice of electron microscope is primarily determined by sample constraints and the depth of analysis needed. SEM is an accessible technique that can be used to study a wide variety of sample sizes and morphologies— from bulk samples several centimeters in size to powder samples with particle sizes on the order of tens of nanometers. As

such, SEM is commonly used to analyze particle size, morphology, surface topography, and the like. Energy Dispersive X-Ray Spectroscopy (EDS) chemical analysis is possible, and Electron Backscatter Diffraction (EBSD) is a common SEM technique to look at crystallographic orientation of a sample over a wide area.[67]

TEM and STEM can collect much of the same information as SEM but with higher spatial resolution and with more advanced analytical capabilites.[68] Figure 1.5 briefly summarizes the capabilities of TEM and STEM, which are discussed in more detail in the following sections of this chapter.

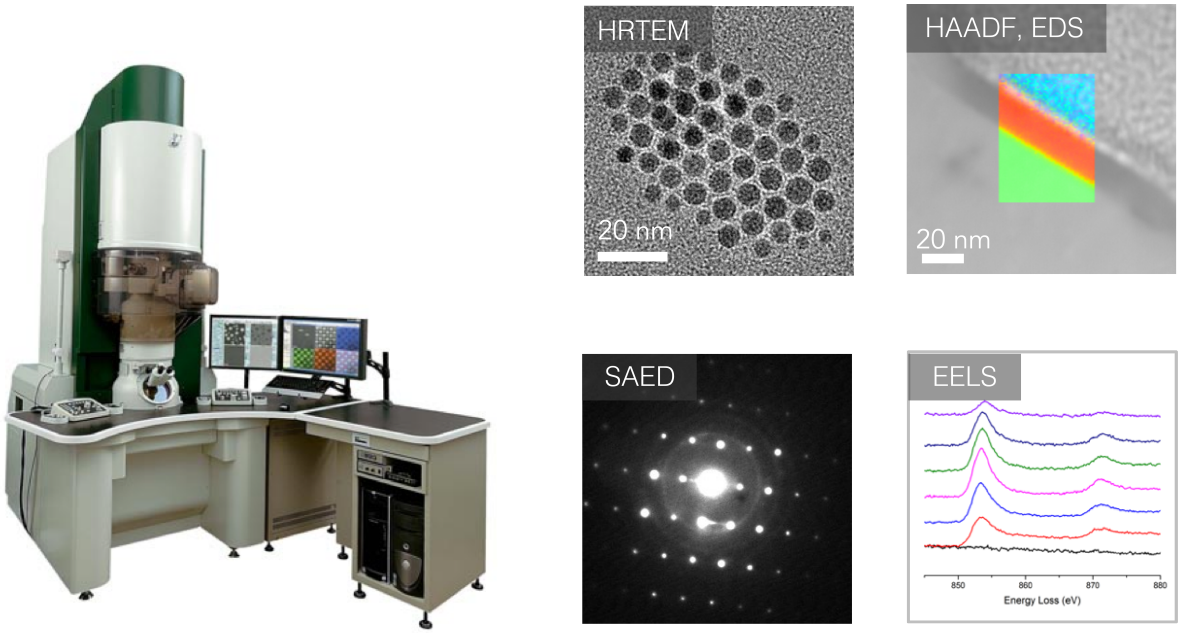

Figure 1.5. The Capabilities of the TEM/STEM. (Left) A JEOL ARM200 aberration corrected TEM. (Right) Examples of different TEM imaging, diffraction, and spectroscopy techniques.

1.6.3. Imaging Modes in TEM and STEM

TEM and STEM have several imaging modes that provide images with different contrast. Combining several kinds of images of the same area can go a long way towards providing a detailed understanding of the material. All of the following techniques can be used to analyze sample morphology and size, down to the atomic scale, but their different contrast mechanisms make them ideal for imaging different kinds of features in the sample. With the advent of aberration-corrected TEM, it is possible to do imaging at the sub-atomic scale with several of the imaging techniques shown.

High Resolution TEM (HRTEM). HRTEM imaging provides micrographs that show features based on phase differences in interfering electron wavefronts, and is commonly referred to as a 'phase-contrast' imaging mode. The advantage of HRTEM imaging is that identification of crystalline lattice planes is straightforward, allowing for the determination of crystal structure and lattice parameter. It is also possible to identify crystalline defects like dislocations and stacking faults.[69]

Bright-Field STEM (BF STEM). STEM imaging provides several different kinds of contrast modes, based on the collection angle of the scattered electrons used to form an image. Electrons that have been only slightly scattered or not at all scattered (i.e. collection angle of < 10 mrad), are collected by a detector to form a BF STEM image. This small-angle scattering of electrons forms images with features based on mass-thickness contrast in the sample or electron diffraction contrast based on changes in lattice structure. As a result, it is an excellent technique for imaging defects in a material.[70]

High-Angle Annular Dark-Field STEM (HAADF STEM). In contrast to BF STEM, HAADF STEM forms images based on electrons that have been scattered to a

large degree (i.e. collection angle > 60 mrad). The angular dependance of electrons that have been scattered to such a degree is based primarily on the atomic number of the element that scattered them. As such, differences in atomic number drive the primary contrast differences in HAADF STEM and it is possible to directly observe compositional inhomogeneities in a sample.[71]

1.6.4. Electron Diffraction

The same electron probe used for imaging a sample can be used for electron diffraction experiments. Selected Area Electron Diffraction (SAED) uses apertures of varying sizes to collect localized structural information from an area as large as several micrometers. In contrast, nanobeam diffraction uses a converged electron probe to collect diffraction information from an area as small as a few nanometers.

Much like XRD, this diffraction information can be used to confirm crystal structure and orientation of a sample, or grains within a sample. Analysis of spacing in the diffraction pattern reveals the lattice parameter, and unique pattern features such as spot-splitting can be used to identify structural defects and crystalline orientation. The degree of crystallinity in the sample can also be qualitatively determined, i.e. if a sample is a single crystal, polycrystalline, or has amorphous regions.[72]

1.6.5. Chemical Analysis in Electron Microscopy: EDS and EELS

TEM and STEM come with the the ability to analyze chemical composition with resolution equal to the aforementioned imaging techniques. STEM in particular provides more control over the area being analyzed as the position of the convergent electron probe can

be precisely moved to an area of interest. This control over the electron probe enables point scans, linescans, and even mapping of the chemical composition in the sample.

There are two primary chemical analysis spectroscopy techniques accessible in the STEM: Energy Dispersive X-Ray Spectroscopy (EDS) and Electron Energy Loss Spectroscopy (EELS). The two techniques provide chemical composition information based on different physical mechanisms— EDS detects x-rays generated by an electron beam while EELS measures scattered electrons.[68] These signals both originate from the interaction of the electron probe in the TEM with the atoms in a sample, as illustrated in Figure 1.6. Electron interactions with the atoms in a sample cause either elastic or inelastic scattering of the incident electron and consequent losses in kinetic energy. All scattered electrons are collected by the EELS spectrometer and are filtered based on the amount of kinetic energy lost, forming an EELS spectrum. These same scattering events often result in the removal of inner-shell electrons from an atom's orbital shell. X-rays are thus generated from the electron transitions to re-fill inner-shell electrons that were lost. These x-rays are detected as EDS signal to identify the elemental composition.

The information provided by the two techniques is complementary. In the context of LIB materials, EDS is a strong technique for studying the composition of transition metals, and some quantitative analysis is possible. However, analysis of light elements can be difficult in EDS, as the absorption coefficients of the light elements generally result in less x-ray signal.[73] Moreover, lithium cannot be detected by EDS as the energy of the lithium K/*alpha* x-rays (54 eV) is too low to be measured by EDS detectors.

EELS on the other hand can readily detect light elements like oxygen and lithium. It is also possible to detect transition metals with EELS, and to use the EELS fine structure

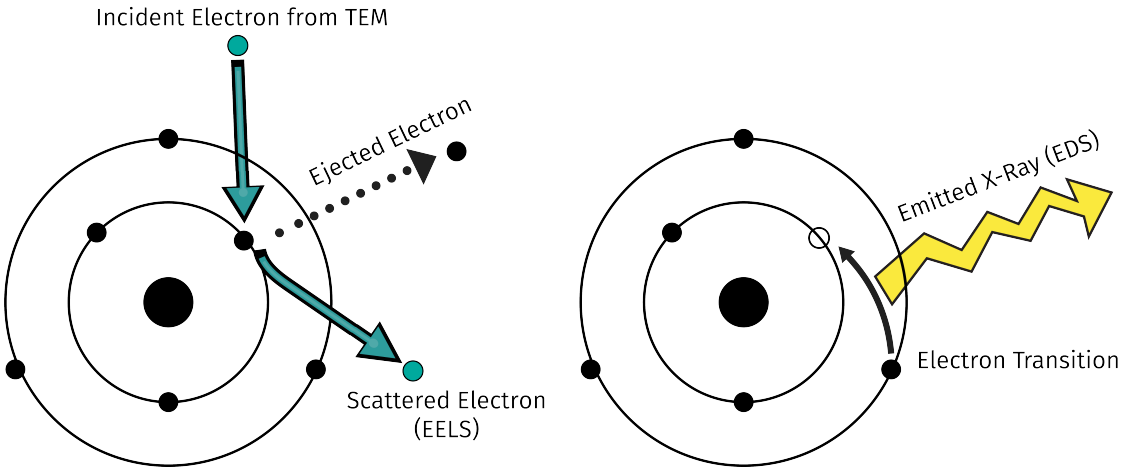

Figure 1.6. Mechanism of Signal Generation for (left) EELS and (right) EDS

to posit detailed chemical information like oxidation state and bonding.[74–78] The primary challenge with EELS comes with the more stringent requirements on sample morphology and thickness compared to EDS – the sample must be necessarily thin and electron transparent (i.e. $<$ 50 - 100 nm) to acquire adequate signal. The EELS spectrometer must also be precisely tuned in order to resolve the spectral features of interest. Moreover, heavy elements tend to have low EELS signal, making EDS the better technique for heavy element analysis.

The Energy Loss Spectrum. Finally, it is necessary to describe the features of the EELS spectrum in more detail to provide necessary context for the work described in this dissertation. As mentioned, the elastic and inelastic scattering mechanisms that occur cause different magnitudes of energy-loss in the incident electrons. These magnitudes of energy loss are generally categorized into different regions in the EELS spectrum as shown in Figure 1.7: the zero loss, valence, low-loss, and core-loss regions.

Each energy-loss region contains different information. The zero-loss region ($0 \sim 2$ eV) is comprised of electrons that have been elastically scattered and lose no energy or very little energy. The resulting zero-loss peak is used to calibrate the EELS spectrum, determine the energy resolution of the spectrum through measurement of its full-width at half-maximum, and estimate sample thickness by comparing its intensity to the remaining EELS spectrum. The low-loss ($30 \sim 100$ eV) and core-loss (100+ eV) spectra contain features that originate from inelastic scattering of the incident electron beam by core-shell electrons in the sample. These regions contain the primary characteristic edges of the elements which provide the detailed chemical information mentioned previously. Features that occur at higher energy losses also have dramatically lower signal intensity (as seen in Figure 1.7), which can make detection and acquisition challenging. The valence EELS region ($2 \sim 30$ eV) contains features from plasmon excitations, interband transitions, and can be used to measure electronic properties of a material like the band-gap. EELS studies of lithium ion batteries typically focus on low-loss and core-loss features and ignore the valence EELS region. Utilizing the valence EELS region for studies on lithium ion battery materials is the main focus of Chapter 4.

1.7. Scope of Dissertation

This dissertation is centered on the challenges facing the development and study of oxides as advanced lithium ion battery materials. New materials chemistries are explored, in addition to new concepts in traditional chemistries. Coupled with the studies of advanced battery materials is the utilization of the wide-ranging electron microscopy toolset and the development of new characterization methods to study nanoscale composition

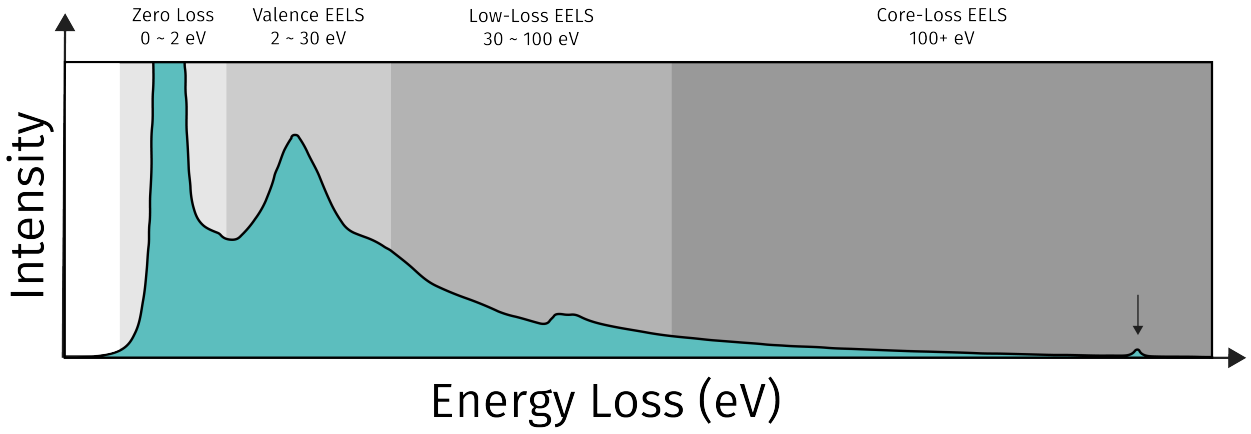

Figure 1.7. Schematic of the Electron Energy Loss Spectrum, with each energy-loss region labelled. The black arrow highlights an example of a core-loss feature with significantly less intensity to compare to other features at lower energy losses.

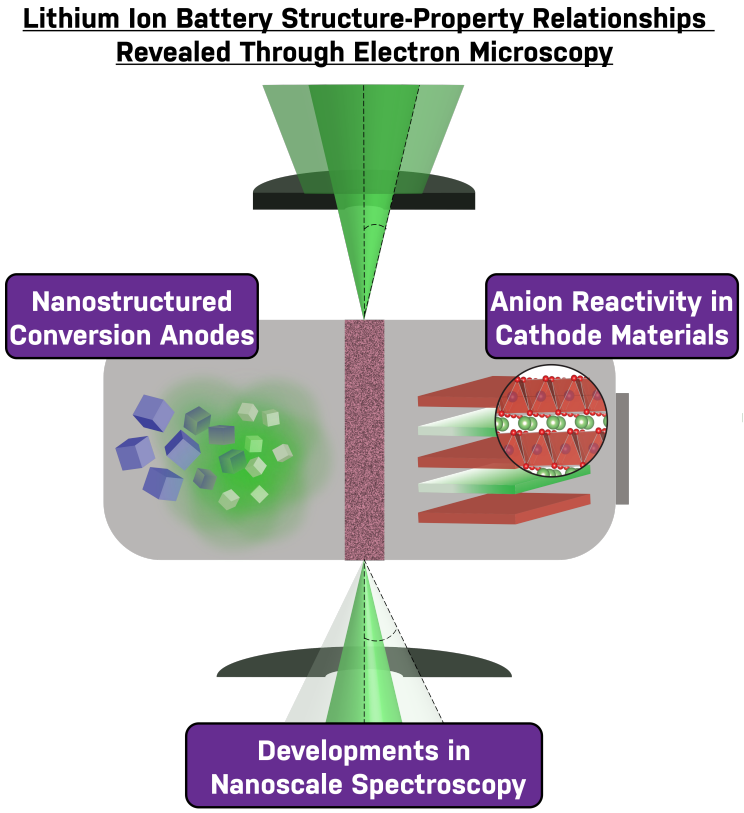

Figure 1.8. Illustration of Dissertation Topics

and structure. This information, when combined with additional electrochemical and x-ray characterization, provides a strong understanding of the electrochemical phenomena at play during the cycling and operation of new materials in battery. Figure 1.8 visually summarizes the projects discussed in this dissertation.

In particular, Chapter 2 works to explore the conversion reaction mechanism and associated electrochemical phenomena. The effectiveness of using a multilayered Ni/NiO structure for improved reversibility of the conversion reaction is considered, as well as the effects of layer thickness and organization on the chemical composition and distribution upon lithiation. A simplified bilayer Ni/NiO system is used to probe structural transformations at relatively high lithiation potentials, and to observe dynamic aspects of the conversion reaction with in-situ TEM.

Chapter 3 explores the possibility of oxygen electrochemistry in the Li-rich cathode material $Li_{2-x}IrO_3$. An integrated computational, x-ray and TEM characterization approach reveal the evolving electronic structure of oxygen during delithiation of Li_2IrO_3 and when oxygen electrochemistry may contribute to additional charge capacity.

Chapter 4 focuses on an extended EELS methodology to study lithium ion battery materials when facing practical sample limitations at the nanoscale. Namely, the valence EELS spectrum region is used to extract complementary information to the characteristic elemental edges.

Chapter 5 discusses brief extensions of the concepts and methods discussed to other important lithium ion battery materials systems, including thiophosphate solid electrolytes, the solid-electrolyte thiophosphate materials, $LiCo_{1-x}Ni_xO_2$, and $LiMn_2O_4$.

Finally, Chapter 6 provides closing remarks and thoughts on the future directions of the fields of lithium ion batteries and electron microscopy.

CHAPTER 2

Lithiation and Conversion in Multilayer Ni/NiO Anode Model Systems

2.1. Chapter Overview

Traditional intercalation electrodes have charge capacities limited by the amount of lithium that can be reversibly inserted and extracted. Major improvements in charge capacity can be made by instead utilizing materials that undergo compete reduction-oxidation reactions with lithium, known as the conversion reaction. However, this change in electrode materials also brings the challenges of significant morphology and oxidation state changes, large volume expansion, and limited structural and chemical reversibility – each of which significantly impede their use as a commercial technology. Electron microscopy plays a large role in the study of these materials, as the conversion reaction generates reaction products and chemical changes at the few-nanometer scale. These nanometric transformations must be understood in order to improve conversion reaction materials.

This chapter focuses on exploring the conversion reaction itself by using a Ni/NiO multilayer structure as a testing ground for electrochemical phenomena and the effects of electrode structure on the conversion reaction. Previous work established the multilayer conversion anode as a strategy for improving reversibility through structural stability.

Here, layer thickness and the overall structure organization are varied and the resulting structure and chemical evolution is characterized using a combination of x-ray and electron microscopy techniques. Imaging and chemical analysis revealed that the layered structure promotes a separation of reaction products and an increased concentration of lithium was found at the layer interfaces. This finding provides insight into lithium transport phenomena through the multilayer structure and the total conversion reaction mechanism. A simplified Ni/NiO bilayer structure was also used to study the conversion reaction process at the theoretically predicted electrode potential, compared to the lower experimental potential for lithiation. The formation of an interfacial metallic layer was observed, which may be one contributor to the overpotentials experienced by conversion materials. Finally, in-situ lithiation TEM experiments are conducted on Ni/NiO nanowires to observe the conversion process directly.

Most of the work described here is adapted from Reference [79] with permission from the PCCP Owner Societies.

Figure 2.1 is adapted with permission from "Morphological Evolution of Multilayer Ni/NiO Thin Film Electrodes during Lithiation. Guennadi Evmenenko, Timothy T. Fister, D. Bruce Buchholz, Qianqian Li, Kan-Sheng Chen, Jinsong Wu, Vinayak P. Dravid, Mark C. Hersam, Paul Fenter, and Michael J. Bedzyk. ACS Applied Materials & Interfaces 2016 8 (31), 19979-19986. DOI: 10.1021/acsami.6b05040". Copyright 2016 American Chemical Society.

Additional work comes from the following manuscript: Evmenenko, G., Fister, T.T., Castro, F.C., Chen, X., Lee, B., Buchholz, D.B., Dravid, V.P., Fenter, P., & Bedzyk, M.J.. "Initial lithiation of NiO thin film electrodes", *in preparation.*

2.2. Introduction

First introduced in the early 2000s, conversion reaction materials have the distinct advantage of having 3 - 5 times larger charge capacities compared to intercalation materials.[51] Conversion materials have the capabilities of being both cathode and anode components in a battery, and can be possible alternatives to both common intercalation cathodes (like $LiCoO_2$) or anodes such as graphite.[80–82,55,83,53] However, conversion materials in general suffer greatly from several reversibility issues intrinsic to the conversion reaction: volume expansion $> 100\%$, reaction products with limited ion and electron conductivity, significant changes to particle morphology, and overpotentials that result in poor energy efficiency.[15] For example, one experiment on the lithiation and conversion of Co_3O_4 nanocubes showed structural breakdown of 5 nm nanocubes into smaller 1 - 3 nm Co metal particles after lithiation. Repeated cycling of this material showed reversibility only between the smaller particle morphology. Furthermore, delithiation and deconversion of the reaction products resulted in only partial reoxidation of Co metal to Co^{2+} in CoO, not the mix of 2^+ and 3^+ states of Co_3O_4.[54]

Conversion materials face a long and uncertain road towards commercialization due to these many challenges. Any strategy for improving conversion materials must improve control over the local environment of the active electrode material in order to minimize volume expansion, maintain ion and electron transport pathways, and enable reversible reduction-oxidation reactions to take place. One proposed strategy to alleviate these issues was to use a multilayered anode structure. This multilayered structure would combine layers of active material alongside "adhesive layers", which together promote structural and chemical stability with cycling. This structure was shown to improve rate capabilities

and cycling lifetimes in silicon-based anode materials.[84,85] The presence of alternating 5 nm layers of Si, held together with 2 nm adhesive layers of Cr_xSi, demonstrated $3x$ expansion in the thickness of the layers but had improved rate capabilities and cycling lifetimes over a pure Si anode. This strategy was also shown to work for prototypical conversion reaction materials, e.g. transition metal oxides, in both Cr/CrO_x and Ni/NiO systems.[86,87] In these cases, the oxide layer acted as the active material while the metallic buffer layer was chosen to promote nucleation of the reaction products. The Ni/NiO structure is particularly useful to study, as it functions as a good model system: Ni and NiO retain a fcc crystal structure and the reduction-oxidation reactions happen between only metallic Ni^0 and Ni^{2+} forms.

$$\mathrm{NiO} + 2\,\mathrm{Li^+} + \mathrm{e^-} \underset{\text{charge}}{\overset{\text{discharge}}{\rightleftharpoons}} \mathrm{Ni} + \mathrm{Li_2O} \tag{2.1}$$

This previous study on Ni/NiO multilayer structures showed that coherent expansion of the Ni/NiO multilayers occurs upon lithiation, with the few-nm thick Ni layers helping initiate conversion at the layer interface while also providing an architecture that confined lithiation to the individual oxide layers.[87]

However, the importance of the individual thicknesses of each layer in the structure is not well understood, nor the overall organization and size of the structure. This work aims to relate these different structure parameters to observable effects on the evolution of the multilayer structure, the chemical distribution after lithiation, and on the reaction kinetics and overpotentials that afflict conversion materials.

Section 2.4.1 begins by analyzing the effect of layer thickness on the electrochemical behavior of the structure. Changes to the multilayer structure and composition after lithiation and conversion are investigated using complementary techniques of X-ray reflectivity (XRR), TEM, and EELS. This approach reveals that there is a critical layer thickness before lithiation of the structure becomes fully impeded, but that when lithiation does occur, there is a phase separation at the Ni/NiO interfaces of Li_2O. Section 2.4.2 continues this work by using a different multilayer organization – a Ni/NiO 2-layer system – to study the conversion reaction after lithiation only to its theoretical potential of 1.8 V rather than its experimental potential at 0.7 V. Early formation of a metallic layer was observed at the interface between the top NiO layer and the electrolyte, which lends insight into the overall conversion reaction mechanism. Section 2.4.3 discusses the use of in-situ TEM techniques to observe the lithiation of similar Ni/NiO structures to understand the material dynamics with real-space data.

2.3. Materials and Methods

2.3.1. Multilayer Film Sample Preparation

Multilayer Films via Pulsed Laser Deposition (PLD). The Ni/NiO multilayer films were grown by PLD on 10 x 3 x 1 mm sapphire α-Al_2O_3 (1–102) substrates. Separate Ni and NiO PLD targets were used to grow the multilayer films with thicknesses of each layer controlled by adjusting the number of laser pulses. Each heterostructure was masked from the bottom nickel layer, providing 3 mm tabs for electrical contact from top spring electrodes.

Preparation of TEM Samples. The cross section samples of the lithiated and partially lithiated thin films were prepared using a FIB system (FEI Helios Nanolab 600 DualBeam FIB/SEM). First, bulk FIB milling techniques were used to isolate the cross-section area of interest. The lamellae were then mounted onto a lift-out TEM grid and further thinned with low energy Ga^+ ions to obtain electron transparent samples with minimal FIB-induced damage.

2.3.2. Electrochemical Characterization

The electrochemical cell used consisted of lithium metal counter and reference electrodes and was fully immersed in a 1 M solution of $LiPF_6$ or $LiClO_4$ in a 1 : 1 ratio of ethylene carbonate and dimethyl carbonate by volume. The choice of salt is known to affect the composition and thickness of solid electrolyte interphase, but was found to not alter structural changes during lithiation at the studied potentials (approximately 0.6 V). A CHI760E electrochemical workstation was used for electrochemical control of lithiation.

2.3.3. X-Ray Reflectivity (XRR) Characterization

Data Acquisition. The in operando XRR experiments were performed at sector 33BM at the Advanced Photon Source (APS) at photon energies of E = 20.00 keV and 17.50 keV. The X-ray beam was collimated to 1.0 x 0.25 mm^2 and the scattered X-ray intensity was acquired with a Pilatus 100k detector. Each sample was fully immersed in a 'transmission-geometry' X-ray compatible electrochemical cell such that the scattering plane aligned along the shorter 3 mm dimension.[84] Full reflectivity data scans were measured in 15 min and were collected repeatedly during electrochemical cycling.

Ex situ XRR studies of lithiated samples after first discharge cycle were done with a Rigaku ATXG diffractometer with E =8.04 keV (λ=1.54Å) x-rays collimated to 0.1 x 2.0 mm^2 spot. All XRR measurements were performed at ambient laboratory temperature.

XRR Curve-Fitting. XRR analysis used the Motofit package with a multiple-slab model that included a sapphire substrate, 1 – 5 Ni/NiO bilayers, and an electrolyte (in-operando) or air (ex-situ experiments). Structural parameters for sapphire and the electrolyte were fixed, whereas the parameters for the buffer and active layers (electron density, interface roughness, and layer thickness) were allowed to vary.

The electron densities were initially estimated based on the chemical composition of the multilayer electrode components.

Compound	Density ρ(g/cm^3)	Electron Density at 17.50 keV ρ_e (e^-/Å^3)	Electron Density at 8.04 keV ρ_e (e^-/Å^3)
1 M $LiPF_6$ in EC/DMC	1.2	0.38	0.38
NiO	6.67	1.97	1.78
Ni	8.90	2.60	2.28
Li_2O	2.01	0.57	0.57
sapphire	3.97	1.18	1.19

Table 2.1. Electron Densities of Bulk Materials

Table 2.1 lists calculated electron densities of bulk materials relevant to this study. For lithiated samples, the structural model included variable electron densities and thicknesses of active NiO-based layers and variable Ni-layer thicknesses with an electron density that was fixed to a value obtained from the analysis of the pristine as-deposited samples. In some cases, the fits made use of a parameter that nominally varies the energy resolution

of the X-ray beam. In this case, this parameter is used as a phenomenological approach to incorporate the lateral heterogeneity of the multilayer structure (e.g., the layer spacing).

2.3.4. TEM/STEM Characterization

HRTEM and STEM imaging were done on all samples using a JEOL 2100F TEM/STEM operating at 200 kV. EELS analysis was done on the same TEM, using a Gatan Enfina GIF system capable of operating with a 1 eV EELS energy resolution, as measured by the full-width at half-maximum of the zero-loss peak.

2.3.5. Sample Preparation and Experimental Setup for In-Situ Biasing in the TEM

Nanowire Synthesis. Ni, NiO, and Ni/NiO nanowires were prepared using a hard-templating method described in Reference [88]. Pure Ni nanowires were obtained using the hard-template method without further processing or sample preparation. Oxidizing the Ni nanowires in the template at 800 °C for 9 hours in air resulted in pure NiO nanowires. Alternatively, oxidation of the Ni in the template at 700 °C for 1 hour resulted in the Ni/NiO 'bilayer' nanowire. After oxidation, the template was etched away as done with the pure Ni nanowires.

All nanowires were dispersed into isopropanol for storage. Simple TEM characterization of the nanowires was done by drop-casting the nanowire solutions onto lacey carbon TEM sample grids.

In-Situ TEM Setup. In-situ biasing in the TEM was carried out using a Nanofactory Instruments STM-TEM in-situ stage connected to an external power source. Separate Au

and W wires were used to mount the nanowires and lithium metal, respectively. Assembly of the in-situ setup was done inside an Ar glovebox, followed by fast transfer into the TEM with a few seconds of exposure to air. The conversion reaction began immediately upon contact of the nanowires with the lithium metal electrode and typically did not need an applied bias.

2.4. Results and Discussion

2.4.1. Effect of Structure and Layer Thickness on Lithiation and Conversion in Ni/NiO Multialyer Films

As mentioned, previous studies of the Ni/NiO layered system showed that it was possible to have complete lithiation of the structure.[87] The multilayer morphology in that study used alternating layers of $\sim$ 2 nm Ni and $\sim$ 6 nm NiO, with a total of 5 Ni/NiO bilayers. After lithiation, a $\sim 2x$ volume expansion was observed, and XRR was used to determine the electron density throughout the thickness of the multilayer structure. This structure change is shown below in Figure 2.1.

A uniform electron density was found between each layer of active material. This electron density matched the theoretical density of a stoichiometric mix of the conversion reaction products Ni and Li_2O, suggesting that the conversion reaction was confined largely to the active NiO layers and that the reaction products were uniformly distributed throughout the layer. This compositional uniformity after lithiation likely contributed to the structural stability observed after extended cycling of the multilayer electrode.

Changing the layer thicknesses of either the Ni or NiO layers would likely have an impact of the degree of lithiation or the cycling rates that are achievable for a given

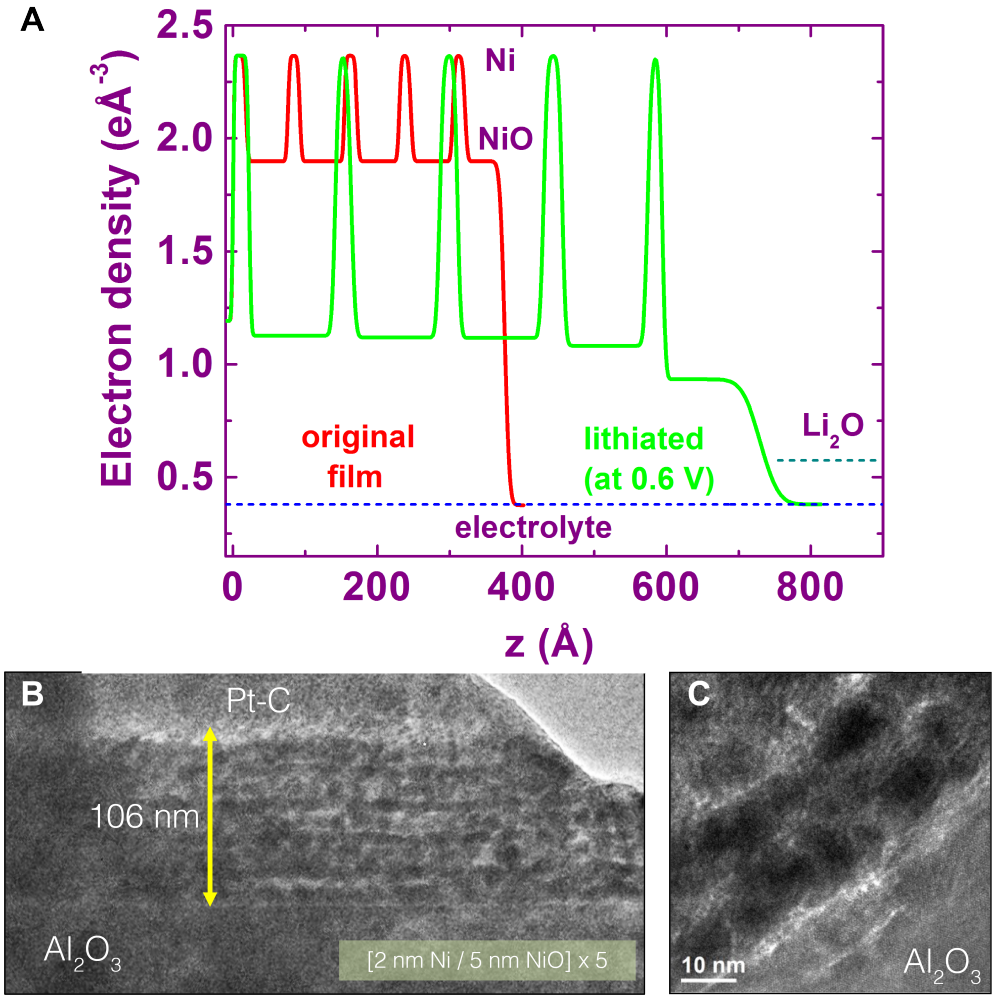

Figure 2.1. 5-bilayer Ni/NiO structure (1 nm Ni and 10 nm NiO layers) fully lithiated to 0.6 V. (A) Electron density profile extracted from XRR for the original structure (red) and the lithiated structure (lime green). (B) HRTEM image of the lithiated structure cross-section, showing complete lithiation of the structure and $\sim 2x$ volume expansion. (C) HRTEM image showing magnified view of bottom few layers of lithiated structure in (B).

multilayer structure. As such, in this study the layer thicknesses and overall number of layers were varied to determine the direct structure-property relationship between overall layer and electrode thickness and behavior during electrochemical lithiation. The first

such variation started with the same overall structure organization of 5 Ni/NiO bilayers. However, thicker $\sim$ 5.5 nm Ni layers were used in combination with 5 nm Ni layers. The multilayer was then electrochemically lithiated using cycling voltammetry (CV) with a half-cell configuration and lithium metal as the reference electrode. The cycling was done using a sweep rate of 0.2 mV/s starting from the open circuit voltage (OCV) of 3.0 - 3.3 V to 0.3 V vs Li/Li^+. Figure 2.2 shows the voltammagram from the first cycle measurement. Lithiation was observed to occur around 0.7 V during the first cathodic scan, as evidenced by the large reduction peak which corresponds to reduction of $Ni^{2+}O$ to metallic Ni^0. However, the total calculated capacity based on the reductive peak estimates that the amount of lithium inserted corresponds to only about 25% of the theoretical capacity expected for a fully lithiated mutilayer structure. Thus, the CV suggests that only partial lithiation of the overall structure occurred.

CV is a powerful method for directly probing the electrochemistry of the 5-bilayer Ni/NiO structure, but changes to the composition and morphology of the structure itself can be studied with both XRR and TEM. Figure 2.3 shows the XRR curves acquired for the pristine multilayer structure as well as from the structure after 1, 2, and 3 CV cycles. There are no obvious shifts of the Bragg peaks seen in the XRR after lithiation, as was observed after complete lithiation in the previous study.[87] However, it is possible to fit the XRR curves and extract the electron density parameter to determine the electron density profile throughout the structure thickness. The analysis of the extracted electron density profiles is shown in Figure 2.4A. The lithiation and consequent conversion of the NiO layers would result in a decrease in the local electron density, down to a density of approximately 1.2 e-/$Å^3$, which corresponds to the stoichiometric mix of Ni and Li_2O.

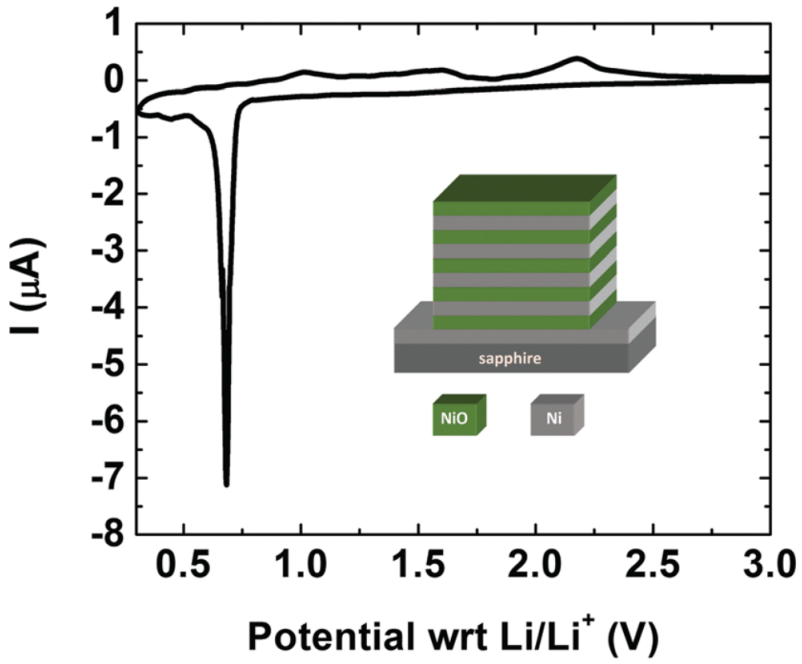

Figure 2.2. First cycle voltammogram of a 5-bilayer Ni/NiO structure (≈ 5.5 nm Ni and 5 nm NiO). A schematic illustration of the pristine 5-bilayer film is inset.

This change in the electron density is only observed at the top of the multilayer stack, meaning that only the top layer of the multilayer was completely lithiated. The electron density profiles also show that the top NiO layer has approximately a $2x$ expansion in the thickness, which is characteristic of a fully lithiated NiO film. However, there is no change to the underlying Ni or NiO layers seen in the electron density profiles in Figure 2.4A, even after 3 full CV cycles. This suggests that the top Ni layer in the stack is totally impeding lithium ion transport to the underlying NiO layers in the multilayer stack.

The XRR data provides useful information through curve fitting of reflectivity curves to extract the electron density profiles. However, the accuracy of these profiles are dependent on the goodness-of-fit of the curves. Therefore, other experimental techniques

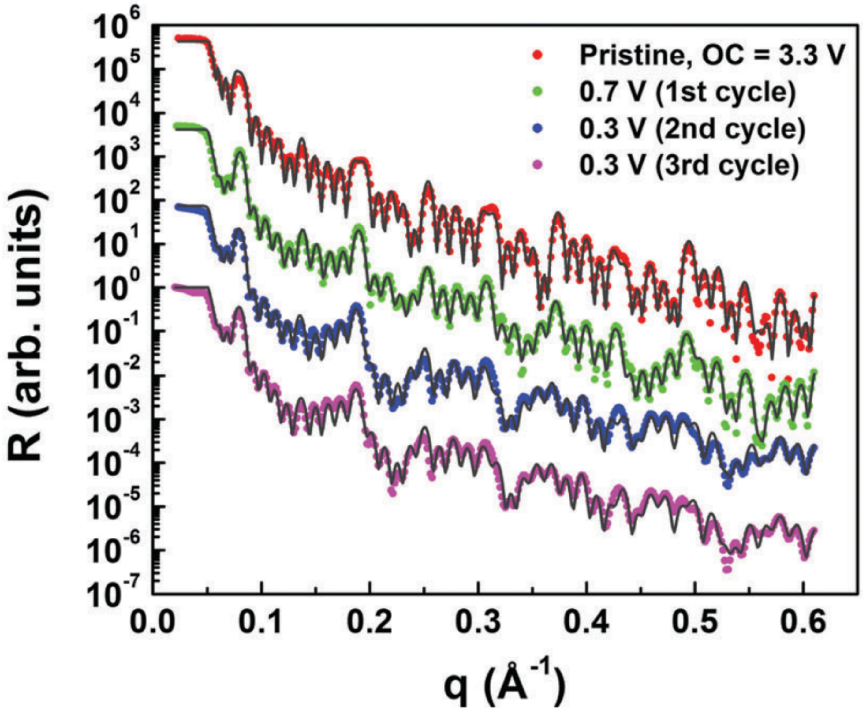

Figure 2.3. Specular XRR data (solid circles) and best fits (solid lines) for the pristine and lithiated 5-bilayer Ni/NiO ($\approx$ 5.5 nm Ni and 5 nm NiO) structures. Each set of experimental and model-fit curves are shifted vertically for clarity.

are needed to fully characterize changes to the multilayer structure after cycling. TEM in particular can provide sub-nanometer imaging and spectroscopic data that can be correlated to the XRR analysis. Figure 2.4B shows a HRTEM image of the full multilayer stack after lithiation. The alternating dark- and light-contrast layers correspond to the alternating Ni and NiO layers, respectively. The measured thickness of each layer corresponds to the expected thickness based on the PLD deposition parameters as well as the XRR analysis. However, the top-most layer of the stack has a lighter contrast than the rest of the NiO layers, which is a result of being the only reacted and lithiated NiO layer. The layer thickness also has the 2-fold expansion seen from the XRR analysis. The total

layer multilayer stack thickness is 56 nm, again showing the minimal, but identifiable, partial lithiation of the structure.

One important feature observable in the electron density profile of Figure 2.4A is the distinct drop in density at the interface between the top Ni and NiO layers. Comparison of this experimental electron density to the theoretical densities listed in Table 2.1 shows that this region has an increased concentration of Li_2O compared to the rest of the reacted layer. There is also a slight increase in thickness of the top Ni layer (< 1 nm) that becomes most prominent after 3 CV cycles. The observation of these two features suggests that there is an important contribution of the Ni layer interface to the conversion reaction that occurs. Additional evidence was shown in the previous study of Ni/NiO multilayers, where TEM and XRR showed increases in the thickness of each Ni layer, likely due to the nucleation and growth of the Ni particle reaction products at the Ni layer interfaces.

Clearly, the layer thicknesses of both the Ni and NiO layers have an effect on the extent of the lithiation reaction and the consequent inhomogeneities observed in the electron density profiles. Two sets of samples were then used to probe the separate influence of the Ni and NiO thickness on the conversion reaction. Electrodes with a 3 layer Ni/NiO/Ni stacking were first analyzed to see at which point the top layer Ni thickness affected lithiation of the underlying NiO structure. 3 samples were prepared with the same bottom Ni/NiO layer thicknesses and varying Ni top layer thickness. These structures are summarized below in Table 2.2.

Figure 2.5 shows the initial cathodic CV scan for each of the 3 different samples, along with the electron densities that were extracted from XRR analysis. Most notably, only two of the three samples were lithiated, while the sample with the 8.9 nm thick Ni layer was

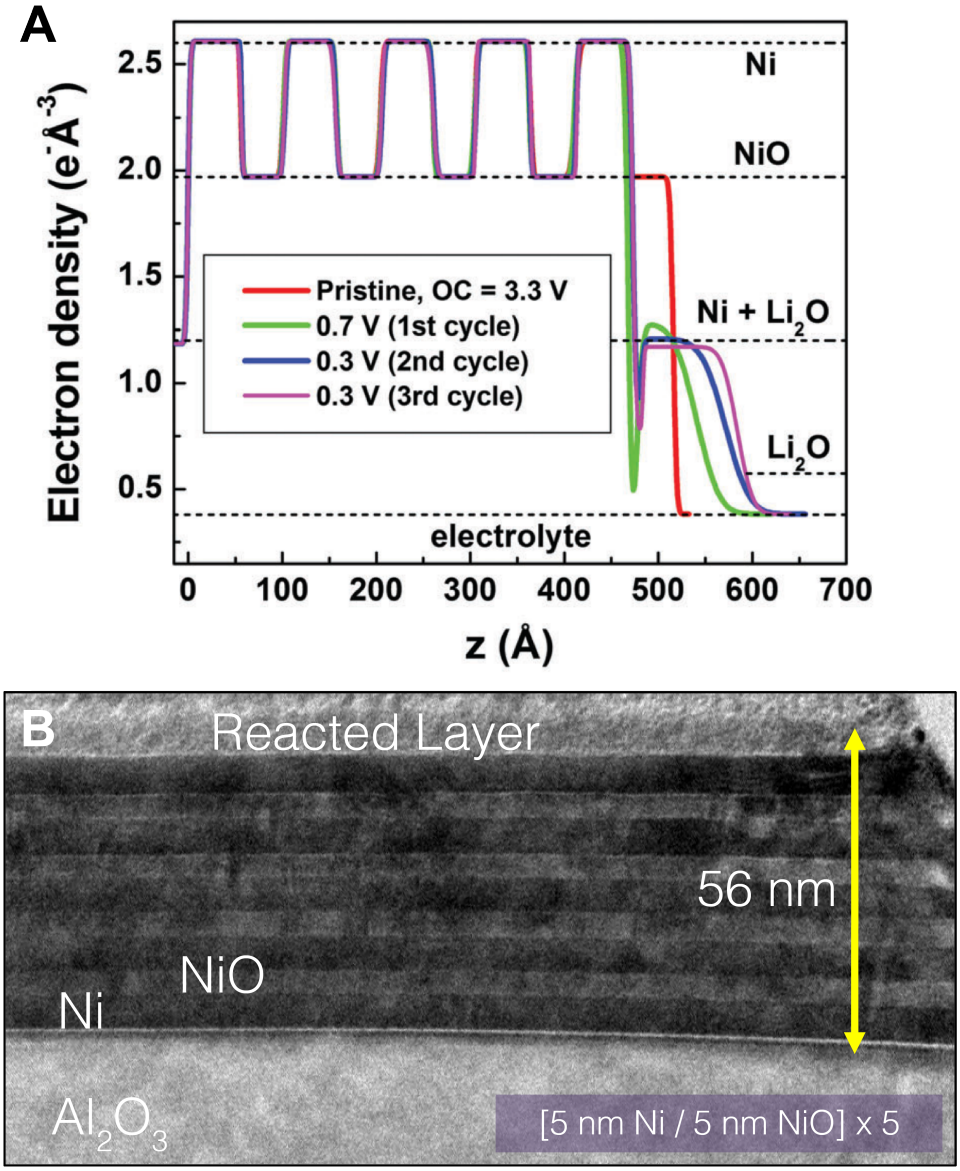

Figure 2.4. XRR and TEM Imaging of 5-bilayer Ni/NiO ($\approx$ 5.5 nm Ni and 5 nm NiO) lithiated to 0.7 V. (A)Electron density profiles obtained from best fits of the XRR data shown in Figure 2.3. Calculated electron densities for the electrolyte, Ni, NiO, Li_2O and expected electron density of the fully lithiated NiO layer (Ni + Li_2O) are shown by dotted lines for comparison, and also tabulated in Table 2.1. (B) HRTEM showing the multilayer structure after lithiation. The overall multilayer structure and thickness is highlighted by the yellow arrow.

Sample	Bottom Ni Layer Thickness	Middle NiO Layer Thickness	Top Ni Layer Thickness
1	5 nm	12.5 nm	3.8 nm
2	5 nm	12.5 nm	6.2 nm
3	5 nm	12.5 nm	8.9 nm

Table 2.2. Summary of 3 layer Ni/NiO/Ni Sample Structures

not lithiated, as might be expected. Only the samples with relatively thin Ni top layers of 3.8 and 6.2 nm showed a significant CV peak Figure Figure 2.5A. The electron density profiles of these two lithiated structures can be seen in Figure 2.5B, and show decreased electron densities in the middle NiO layer indicating the formation of conversion reaction products. In contrast, the 8.9 nm thick Ni top layer sample shows no difference in electron density profile in Figure 2.5C between the pristine (blue) and cycled (lime green) states.

Juxtaposing the electron density profiles of the samples with 3.8 nm and 6.2 nm top Ni layers in Figure 2.5B show two features of interest: the 6.2 nm top layer sample has a lower average electron density in the reacted NiO layer and shows a decrease in the electron density at the top Ni/NiO interface, whereas the 3.2 nm top layer sample has a higher overall electron density but significantly lower electron density at the bottom Ni/NiO interface. Furthermore the Ni layer in this sample additionally shows a decrease in the electron density of the top Ni layer, suggesting some decomposition or change to the top Ni layer. Although lithiation of the lower NiO layers in Figure 2.4 was not observed when the Ni layers were 5 nm thick, lithiation was observed when the top Ni layer was 6.2 nm. This suggests that there is an interplay between the total thickness of the Ni/NiO layers that determine whether lithiation of the whole structure is possible or not. Furthermore, the sample with the thinnest Ni top layer underwent a significant

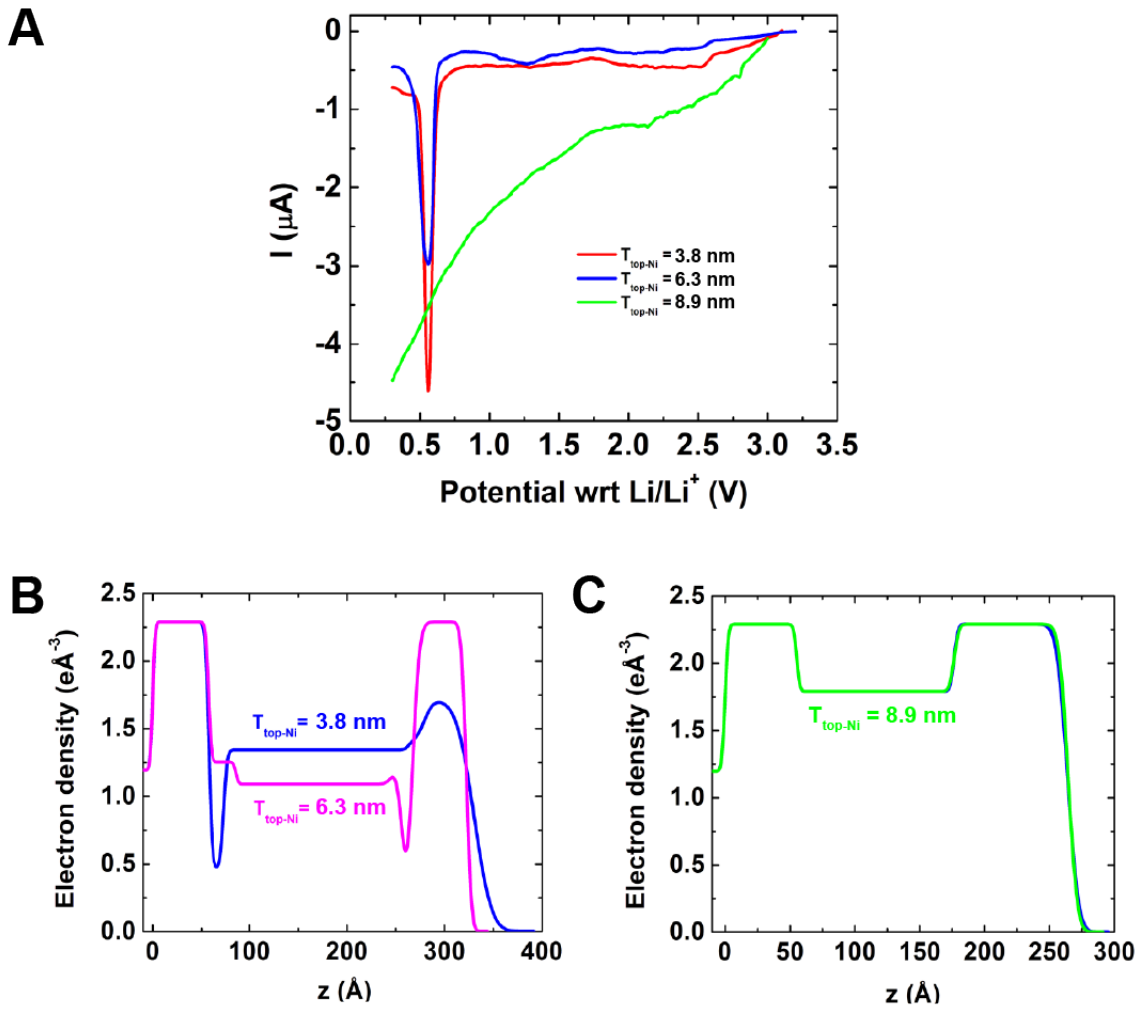

Figure 2.5. Behavior of 3 layer Ni/NiO/Ni films after electrochemical lithiation. (A) First cycle voltammograms of each of the three samples described in Table 2.2. (B) Electron density profiles for the samples with 3.8 nm top Ni layer (blue) and 6.3 nm top Ni layer (pink) after lithiation. (C) Electron density profiles for the sample with 8.9 nm top Ni layer before (blue) and after (lime green) lithiation.

reaction and phase separation between Ni and Li_2O reaction products, given the drastic electron density drop at the bottom Ni/NiO interface and the higher overall electron density throughout the reacted NiO middle layer.

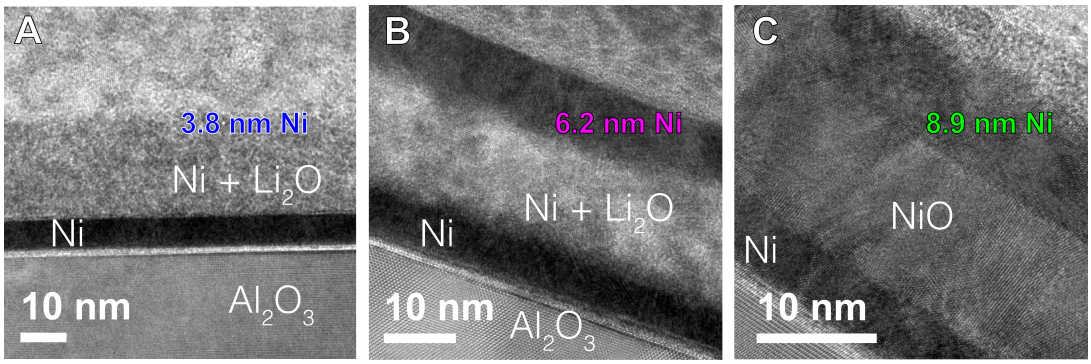

Figure 2.6. HRTEM Images of 3 Layer Ni/NiO/Ni Samples after lithiation to 0.7 V. (A) Sample with 3.8 nm Ni top layer. (B) Sample with 6.2 nm Ni top layer. (C) Sample with 8.9 nm Ni top layer.

Figure 2.6 shows the HRTEM images of the 3 layer samples. The 3.8 nm Ni top layer sample has the largest observable change under TEM. The underlying Ni layer is clearly seen in the image, as the layer with darkest contrast. However, the top Ni layer is not distinguishable against the underlying lithiated NiO layer. This result matches the electron density profile, which shows a decrease in density of the top Ni layer after lithiation, and suggests that there was some deterioration of the integrity of the very thin top layer. In contrast, the sample with 6.2 nm and 8.9 nm top Ni layers clearly have a dark-contrast top layer in the HRTEM image that pertains to the Ni layer. The 6.2 nm top Ni layer sample, seen in Figure 2.6B has an expanded middle NiO layer with mixed bright- and dark-contrast regions corresponding to successful lithiation. The 8.9 nm top Ni layer sample seen in Figure 2.6C on the other hand has 3 distinct even-contrast layers which have thicknesses equivalent to the pristine sample, further supporting the XRR evidence that the sample was not successfully lithiated due to the thickness of the Ni top layer.

In order to determine interdependence between Ni and NiO top layer thickness on the lithiation behavior, a simpler 2-bilayer Ni/NiO multilayer structure was used rather than the 5-bilayer structure shown in Figures 2.1 and 2.4. Four different samples were prepared, with layer thicknesses summarized in Table 2.3. The overall thickness of the NiO layer in the structure was kept the same ($\sim$ 12 nm) was with the 3-layer samples, and the thickness of the middle Ni layer was varied between 1.6 nm and 8.2 nm.

Sample	Bottom Ni Layer Thickness	Middle NiO Layer Thickness	Middle Ni Layer Thickness	Top NiO Layer Thickness
1	5 nm	6 nm	1.6 nm	6 nm
2	5 nm	6 nm	3.7 nm	6 nm
3	5 nm	6 nm	5.8 nm	6 nm
4	5 nm	6 nm	8.2 nm	6 nm

Table 2.3. Summary of 4 layer Ni/NiO/Ni/NiO Sample Structures

Each sample was again cycled to 0.3 V as before to allow for complete lithiation of the structure if the overall layer thicknesses allowed lithiation to occur. Figure 2.7 shows the CV results of each of the four samples. Each sample shows a cathodic peak at approximately 0.7 V as observed in previous structures, however the two samples with the thickest middle Ni layer (5.8 nm and 8.2 nm) have calculated charge capacities of 50% of the theoretical capacity, suggesting that only one of the NiO layers was fully lithiated.

Figure 2.8A shows the electron density profiles for each sample. Overall, the electron density profiles reflect the CV curves for each sample, and reveal the anticipated partial lithiation for the two samples with the thickest Ni layers. For these samples, the top NiO layer shows lithiation through the decrease in electron density, but no change from the pristine NiO electron density in the lower buried NiO layer. In contrast, the two samples

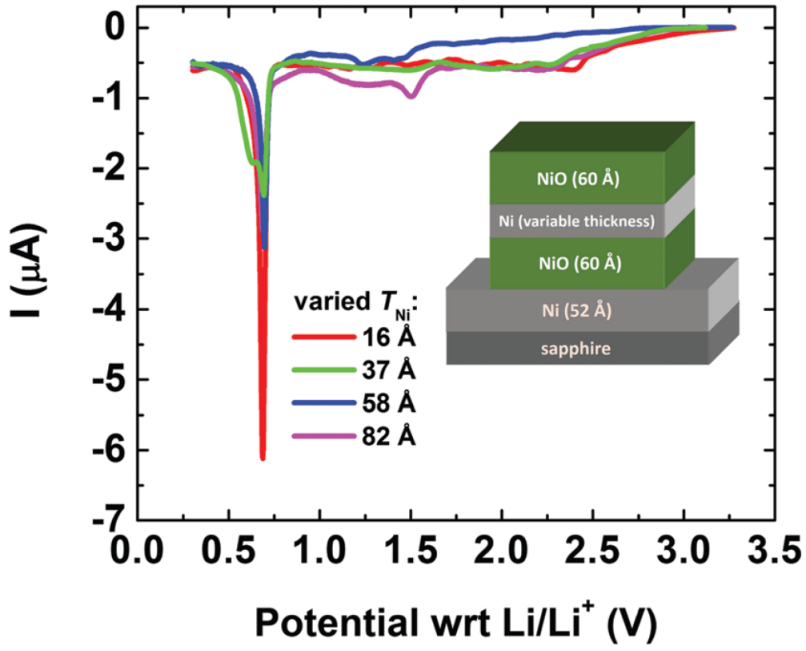

Figure 2.7. First cycle voltammograms for the 4 layer Ni/NiO/Ni/NiO samples listed in Table 2.3. A schematic illustration of the 4 layer samples is inset.

with the thinnest Ni middle layers show complete lithiation and a decrease in the electron density of both NiO layers. The observed reaction peak for these two samples has an asymmetric shape with two peaks at 0.69 V and 0.63 V which seen to correspond two a two-step lithiation process– the top layer being lithiated first and the bottom layer being lithiated only when there is a stronger driving force for lithium transport. However, all four samples show the formation of low electron density regions at the Ni/NiO interfaces in the layers that were successfully lithiated. Furthermore, the two samples that had lithiation in the buried NiO layer show a greater change in the electron density at the bottom-most Ni/NiO interface than in the top Ni/NiO interface. The Ni layers next to these interfaces show a slight increase in thickness after lithiation (<1 nm) which again

suggest the presence of some phase separation between Ni and Li_2O reaction products which result in the unique electron density profiles observed after lithiation.

The TEM analysis shown in Figure 2.4 did not show strong evidence of the formation of these low electron density regions at the Ni/NiO interfaces. Figure 2.8B shows a higher magnification HRTEM image of the sample with the thinnest 1.6 nm Ni layer. Each Ni/NiO layer can be clearly seen in the HRTEM image and, again, the overall structure organization and layer thickness observed via TEM matches the thicknesses determined by XRR and shown in the electron density. However, HRTEM imaging alone does not have the capability of identifying and analyzing the low-electron density regions seen via XRR analysis. However, HAADF STEM imaging provides contrast based on the average atomic number of the compound being imaged, and may reveal the low electron density region via imaging techniques. Moreover, EELS can be paired with HAADF imaging, which provides the ability to detect composition changes in light elements like lithium and oxygen. This combined approach enables the direct study of these low electron density regions in the samples.

As seen in Figure 2.9A, HAADF STEM imaging reveals each layer in the structure, with the brightest layers consisting of Ni, which have the highest average atomic number. This image confirms the general results found by XRR data, namely the two-fold expansion of each oxide layer during lithiation. Precise EELS line scans were carried out to confirm the composition of each layer of the cross-section. Each colored marker in 2.9A corresponds to the colored spectra of the O-K edge in Figure 2.9B. Close attention was given to the O-K edge signal from the lower layer of NiO that underwent conversion to Ni and Li_2O in order to determine changes in composition throughout the thickness of

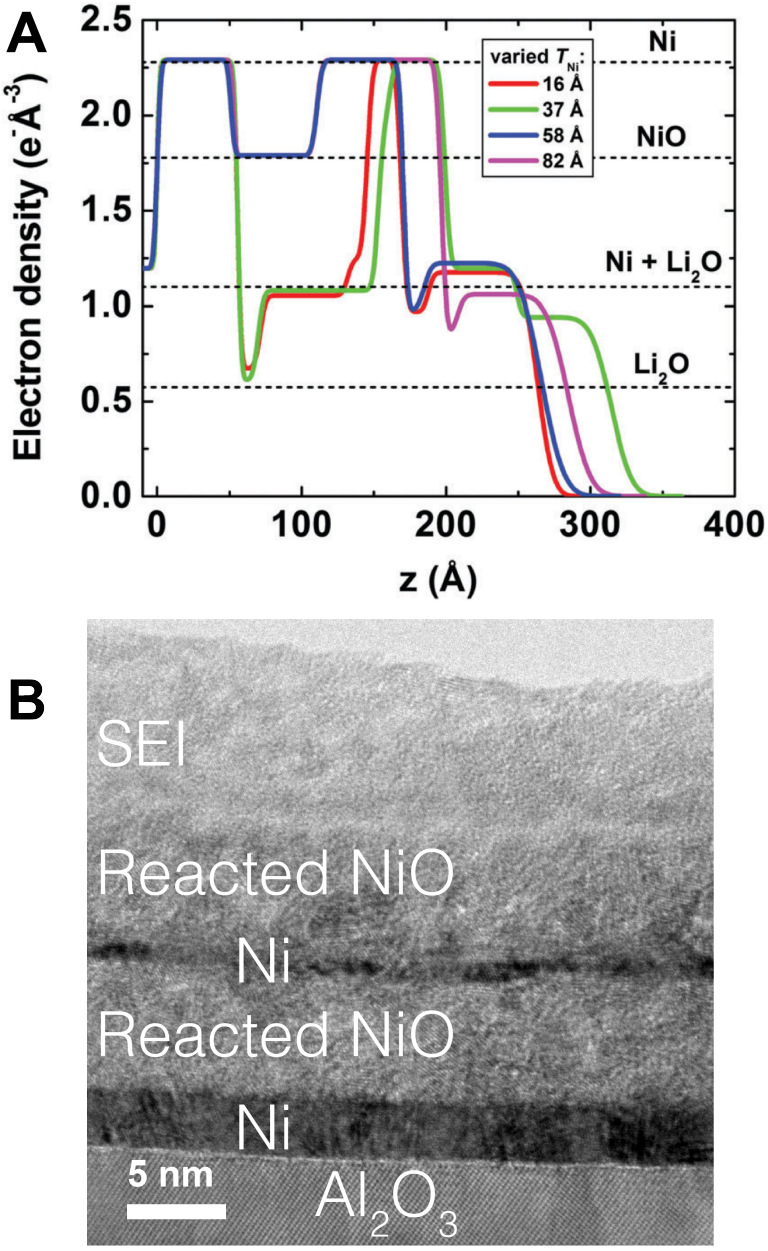

Figure 2.8. Structure of 4-layer (5 nm Ni/6 nm NiO/varied Ni thickness/ 6 nm NiO) samples after lithiation to 0.7 V. (A) Electron density profiles of the 4 layer samples described in Table 2.3. The calculated electron densities for the electrolyte, Ni, NiO, Li_2O and expected electron density of the fully lithiated NiO layer (Ni + Li_2O) are shown by dotted lines for comparison, and also tabulated in Table 2.1. (B) HRTEM image of 4-layer sample (5 nm Ni/6 nm NiO/1.6 nm Ni/ 6 nm NiO) lithiated to 0.7 V.

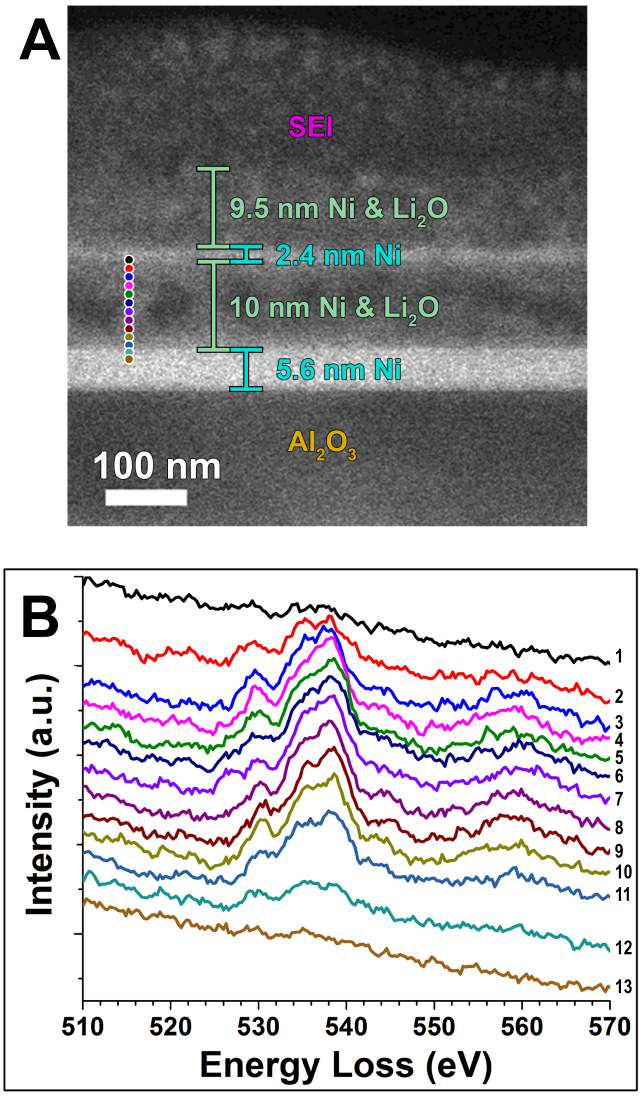

Figure 2.9. Additional analysis of 4-layer sample with 5 nm Ni/6 nm NiO/2.4 nm Ni/ 6 nm Ni structure, lithiated to 0.7 V. (A) HAADF STEM image of sample with thinnest Ni middle layer. The thicknesses of each layer are measured and labelled. Colored circles indicate the position from which EELS spectra were collected. (B) EELS spectra of the O-K edge, with line coloring matching the coloring in the markers from A. Spectra are also numbered from 1 - 13, with spectrum 1 corresponding to the top of the linescan and spectrum 13 corresponding to the bottom of the linescan.

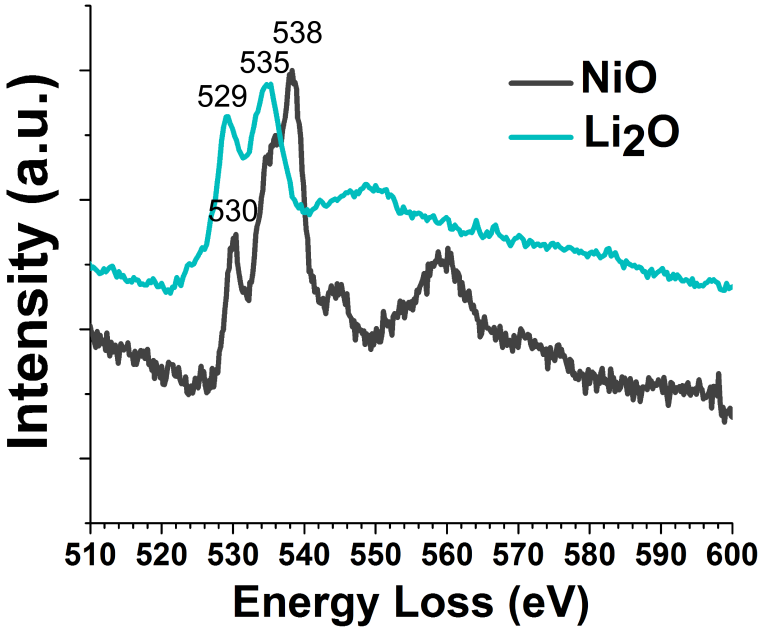

Figure 2.10. Reference EELS spectra of the O-K edge for both NiO and Li_2O. The distinguishing peaks at 538 eV and 535 eV are marked for NiO and Li_2O, respectively. Additional labels are included for the oxygen pre-edge feature in both compounds.

the individual layer. The O-K edge fine structure has distinct features at 535 eV and 538 eV, which can be used to identify and differentiate between Li_2O and NiO, respectively. The difference in fine structure between the two compounds is highlighted in Figure 2.10. Analysis of the Li-K EELS edge is also possible but accurate quantification can be challenging, whereas analysis of the oxygen EELS feature would directly show the presence of Li_2O in the structure. Spectra collected progressively further down in the layer show increasing prominence of the O-K edge feature at 535 eV, suggesting an increasing concentration of Li_2O at the bottom of the layer.

A multiple linear least squares (MLLS) fitting procedure was used to analyze the EELS data from Figure 2.9. This MLLS fitting is typically used for extracting weak edge signals

from the EELS background, isolating signals from overlapping edges in both low-loss and core-loss EELS regions, or mapping elemental compositions.[89–92] The MLLS procedure involves fitting a spectrum with an expression of the form

$$F(E) = AE^{-r} + \sum_{n} B_n S_n(E) \tag{2.2}$$

where the first term is represents the background preceding the edge of interest with a typical power-law function, and the second term represents the summation of the input reference spectra $S_n(E)$ multiplied by the calculated fitting coefficients B_n, and is readily applied using the built-in function found in the Gatan Digital Micrograph software. This MLLS fitting differentiates between oxygen in the different electronic environments of NiO and Li_2O.

The core-loss reference spectra shown in Figure 2.10 were used as the input reference spectra for MLLS fitting of the 13 line scan spectra found in Figure 2.9. Figure 2.11 shows a MLLS fit of the O-K edge from the 8^{th} spectrum from 2.9 (with same spectral color code), which used a fitting range of 532 eV to 550 eV in order to encompass only the primary O-K edge features. This MLLS fit is representative of the kind of fits found for all other line scan spectra. The coefficient values, B_n from equation 2.2, for Li_2O and NiO contributions are plotted in Figure 2.11B for each of the 13 spectra shown in Figure 2.9, with spectrum 1 indicating the first spectrum of the line scan (black-colored line) and spectrum 13 indicating the final spectrum of the line scan (mustard-colored line), at the top and bottom of the lithiated NiO layer, respectively. Most notably, the coefficient value of Li_2O begins to increase dramatically in spectra 10 through 13, signaling

an increase in contribution of the Li_2O reference spectra to the MLLS fit. This suggests an increase in Li_2O concentration close to the interface with the bottom Ni layer. This result is consistent with the X-ray reflectivity data that showed areas of lower electron density close to the interface with the bottom Ni layer seen in Figure 2.9. Additionally, the coefficient values indicate a variable Li_2O composition throughout the converted Ni and Li_2O structure. These results accurately reflect the O-K fine structure evolution seen in Figure 2.9. The presence of the feature at 538 eV, which corresponds to NiO, is unexpected in this region of the sample as it should have been reduced during conversion, but can be attributed to oxidation of the Ni reaction product when exposed to air while handling the sample during preparation and loading into the TEM.

The Ni EELS features were also considered during the analysis. Ni has two characteristic features in EELS: the Ni L_3 and Ni L_2 edges. The intensity ratio between these two sharply-peaked features will change based on the oxidation state of the Ni atoms, as demonstrated in in Figure 2.12A.[78] Figure 2.12B shows the EELS linescan results for the Ni $L_{3,2}$ edges, which extended from the bottom of the middle Ni layer to the bottom of the lower NiO layer, as was shown for the O-K edge in Figure 2.9. A Ni $L_{3,2}$ intensity ratio corresponding to Ni^0 metal is initially seen from the middle Ni layer, which then quickly evolves to an intensity ratio that corresponds primarily to Ni^{2+}. Just as NiO features were seen in the O-K edge EELS signal after lithiation, these results suggest the presence of NiO in the layer even after lithiation. However, this finding is likely due to the fact that there is some oxidation of the cross-section sample during handling and transfer into the TEM, as the TEM corroborates the structural evolution seen via XRR, and the XRR shows the decrease in electron density corresponding to a mix of Ni and Li_2O in the

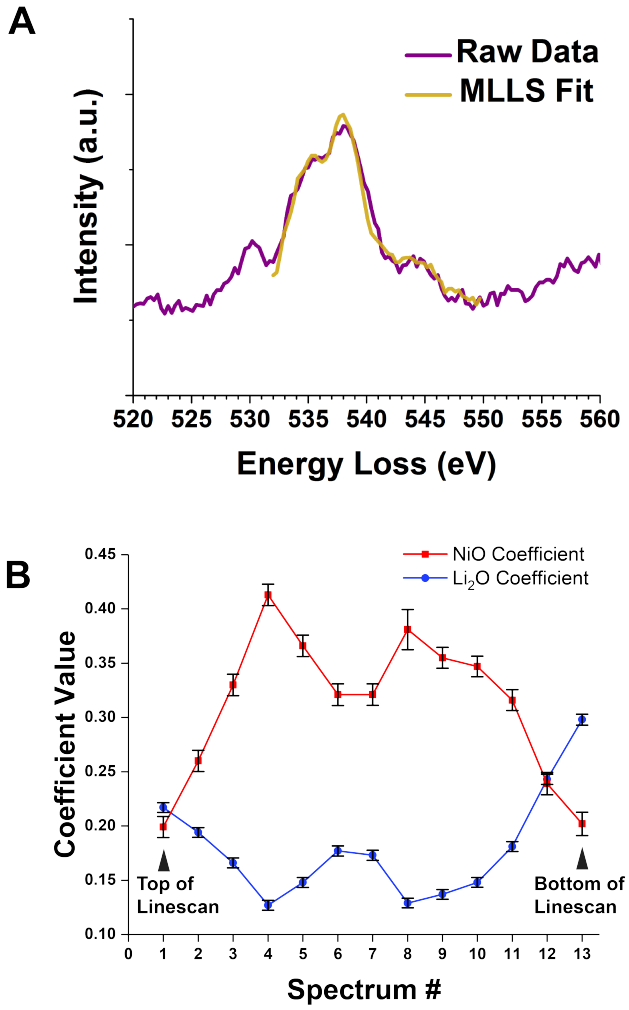

Figure 2.11. MLLS fitting results of O-K EELS linescan from 4-layer sample with 5 nm Ni/6 nm NiO/2.4 nm Ni/ 6 nm Ni structure, lithiated to 0.7 V. (A) The raw O-K edge from the 8^{th} spectrum from Figure 2.8 (burgundy line) with MLLS fit (mustard line) overlaid. (B) Plot of MLLS fitting coefficient (B_n) described in Equation 2.2 for each EELS spectrum.

sample. Nevertheless, the O-K edge analysis is still able to identify the presence of Li_2O and changing concentration suggested by the electron density profiles.

Additional CV analysis was used to relate changes in the multilayer structure, e.g. layer thickness, to the lithiation kinetics of the electrode. Figure 2.13A shows the first

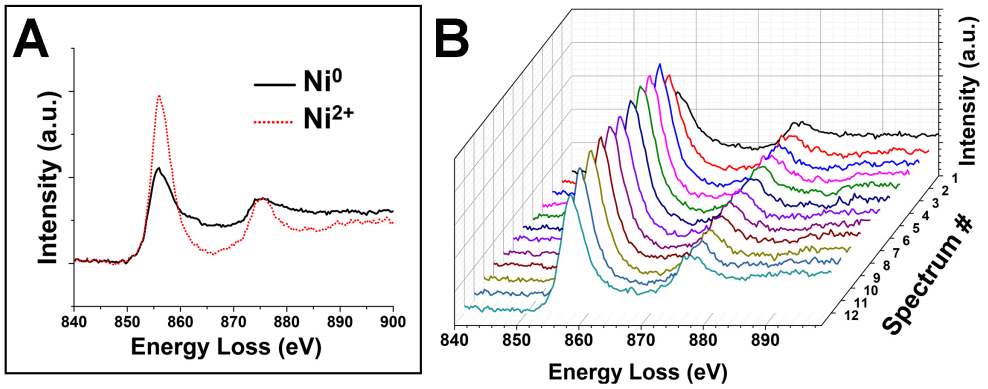

Figure 2.12. EELS analysis of Ni $L_{3,2}$ Edges. (A) Comparison of Ni $L_{3,2}$ edges for Ni^0 metal and Ni^{2+} showing the difference in peak ratios. (B) EELS linescan of the Ni $L_{3,2}$ edge from the middle Ni layer through the bottom of the buried NiO layer.

lithiation CV curves of four 2-bilayer electrodes, each with a morphology of the the thinnest Ni top layer sample described in Table 2.3, with voltage scan rates from 0.1 to 0.55 mV/s. For each scan rate, similar charge capacities are achieved, which ranged from 8 - 9 $\times 10^{-4}$ mAh. Although the lineshape and full-width at half-maximum of each reduction peak were approximately the same, there is an evolution in the peak current that is observed. Plotting the peak currents for each scan rate shows a linear trend seen in Figure 2.13, with a slope of 0.089 C/V. The change of peak current with sweep rate can also be calculated based on Equation 2.3 below:[93]

$$I_p = \frac{n^2 F^2 A \Gamma v}{4RT} = Sv \tag{2.3}$$

where n (number of electrons transferred in redox) = 2, T (temperature) = 293 K, R (the ideal gas constant) = 8.314 J/K mol, F (Faraday's constant) = 96,485 C/mol,

$A\Gamma$(number of moles of active material) = 1.25 $\times 10^{-8}$ mol. The calculated value gives a change of 0.05 C/V, which is close to the experimental results. This linear relationship between sweep rate and peak current thus implies that the lithiation process overall is limited by the surface reactions at the liquid-solid interface rather than diffusion through the overall film structure.

Overall, tuning the multilayer structure showed that there are critical thickness levels above which lithium transport is impeded throughout the structure. The Ni layer thickness plays the most important role, as Figures 2.5 and 2.6 showed that lithiation does not occur in the NiO layer when the top Ni layer is much larger than $\sim$ 7 nm. However, the combined Ni/NiO layer thickness matters as well, as only partial lithiation was observed in the case of 5 nm Ni/ 5 nm NiO 5-bilayer system seen in Figure 2.4. These findings suggest a critical combined Ni/NiO thickness of $\sim$ 7 nm at the potentials that the anode was cycled to. The overall structure thickness in many of the films studied is larger than 7 nm, so this metric better describes the limit of consecutive very high Ni density regions before lithium is blocked.

In addition, this multilayered structure showed the formation of low electron-density Li-rich regions at the Ni/NiO interfaces, and some accompanying expansion of the Ni layers as well. As such, it is possible that the interfaces are promoting the conversion reaction to occur at these interfaces, and that some lithium build-up at these interfaces also occurs during the lithiation process.

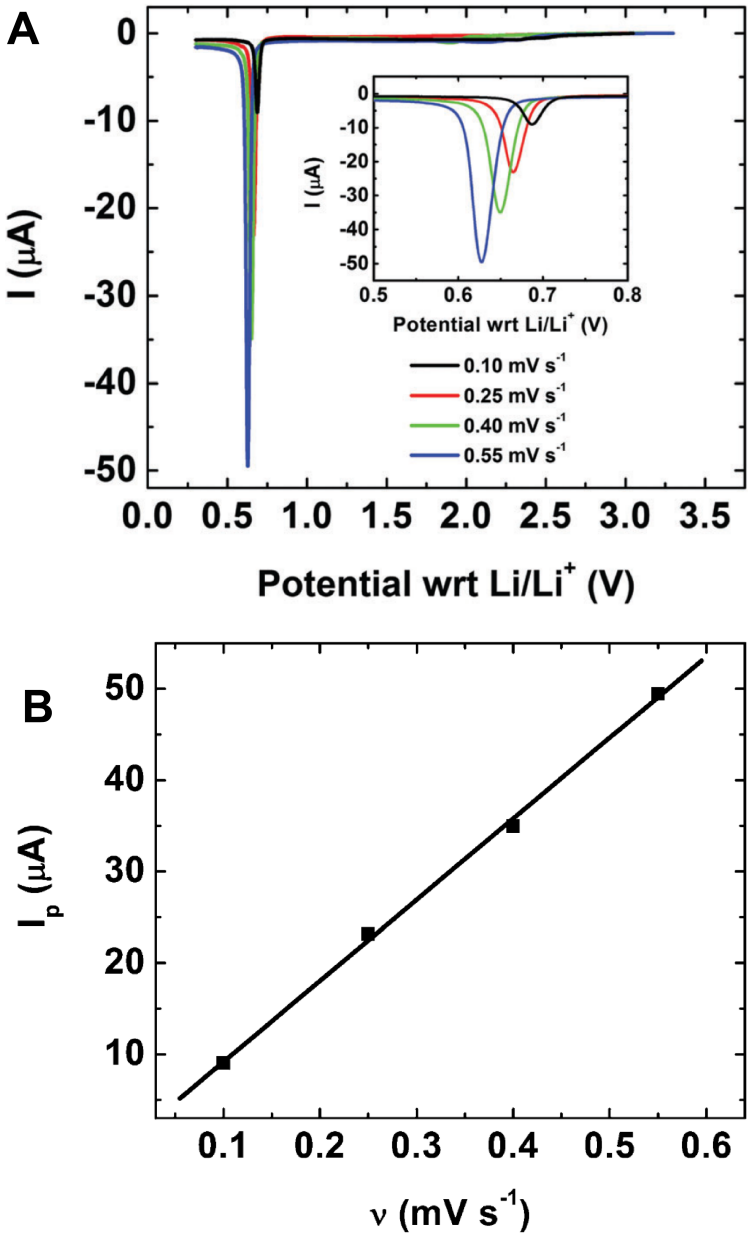

Figure 2.13. Electrochemistry of 2-Bilayer Ni/NiO samples (5 nm Ni/6 nm NiO/ 1.5 nm Ni/6 nm NiO) samples with varying scan rate. (A) First discharge voltammograms of 2-bilayer Ni/NiO electrodes with scan rates in the range of 0.1 to 0.55 mV/s. Voltammograms in the region of the reduction peak potential are shown in the inset. (B) Scan rate-dependence of the peak current for 2-bilayer Ni/NiO electrodes.

2.4.2. High Potential Lithiation of Ni/NiO Films

Varying multilayer structure and layer thickness showed a direct and observable relation to the degree of lithiation in the electrode and the overall cycle stability of the electrode. The other strong challenge facing conversion reaction electrodes is the overpotentials that they suffer from compared to intercalation based electrodes. That is, there is a difference between the voltage at which an electrochemical reaction should happen based on thermodynamics, and the experimental voltage at which an electrochemical reaction is observed. In many cases, this potential difference is > 1 V.[15] For example, NiO has a theoretical potential for lithiation of approximately 1.8 V vs. lithium, but undergoes lithiation closer to 0.7 V as observed in Section 2.4.1. It is possible that the same Ni/NiO bilayer system could be utilized to closely study the lithiation process throughout the overpotential range and better understand the relationship between morphology and electrochemistry in these conversion materials.

A single Ni/NiO bilayer structure was used to study the 'high-potential' behavior of NiO around 1.8 V in order to observe morphological changes to the NiO layer and also at a single Ni/NiO interface. The primary film structure analyzed consisted of a 4.9 nm Ni bottom layer and 6.7 nm NiO top layer. An additional sample was also examined which had a 4.9 nm Ni layer and 1.9 nm NiO top layer. These bilayer structures were cycled using CV from the open circuit voltage ($\sim$3.2 V) to 0.3 V using a sweep rate of 0.1 mV/s. Their first discharge CV behavior is shown in Figure 2.14 The reduction peak for both samples occurs at different potentials, with the 6.7 nm NiO sample showing NiO reduction at 0.7 V as previously observed, and the thinner 1.9 nm NiO layer showing an asymmetric peak and some evidence of reduction happening at 0.5 V.

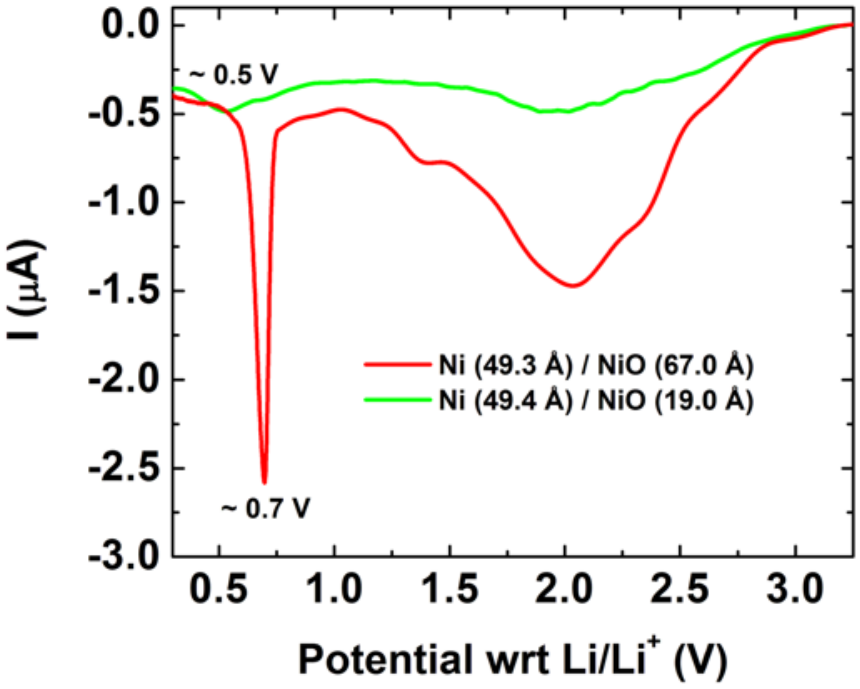

Figure 2.14. First discharge cyclic voltammograms of Ni/NiO Bilayers (5 nm Ni/6.7 nm NiO and 5 nm Ni/1.9 nm NiO). The reduction peak indicating the onset of lithiation is indicated for both bilayer structures.

XRR analysis was conducted on these two bilayer samples in-operando in order to study their evolution during the first electrochemical discharge cycle. Electron density profiles were extrated from the fitted XRR spectra, and are shown in Figure 2.15. The Ni/NiO bilayer with the thin 1.9 nm NiO top layer shows a change in the morphology early on in the discharge cycle, at high potentials indicated in Figure 2.15A. Steady changes to the electron density of the top NiO layer eventually result in a flat profile with electron densities expected for complete lithiation and conversion of the layer. There is a strong change in the electron density at the Ni/NiO interface during the discharge cycle as was previously observed in other multilayer samples. In contrast, the thicker NiO top layer sample shows only a minimal change in the electron density at high potentials, as seen in

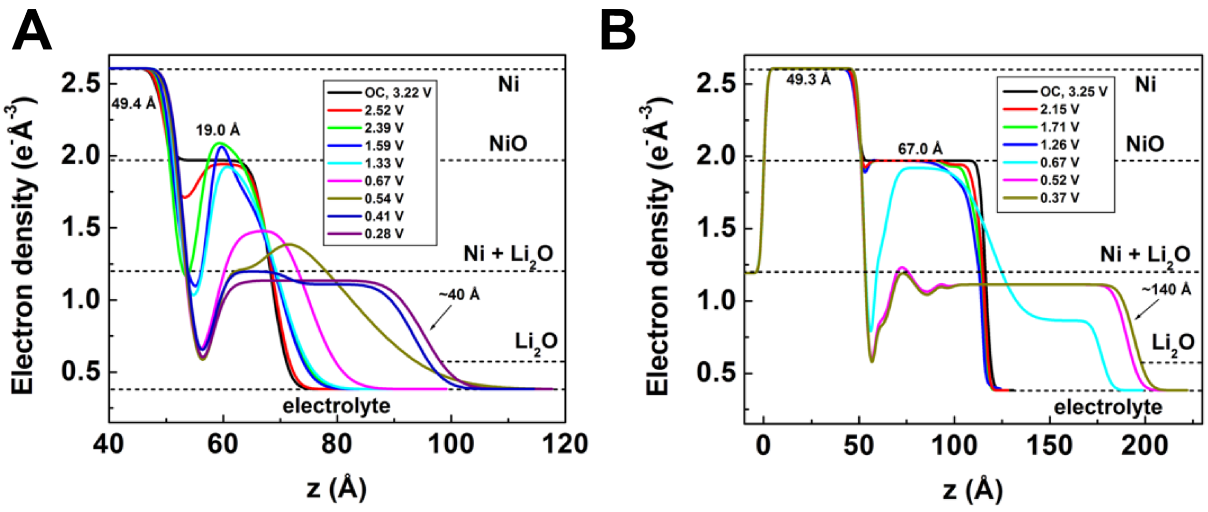

Figure 2.15. XRR analysis of bilayer Ni/NiO structures (5 nm Ni/1.9 nm NiO and 5 nm Ni/6.7 nm NiO) during the lithiation process. (A) Electron density profile for 5 nm Ni/1.9 nm NiO. (B) Electron density profile for 5 nm Ni/6.7 nm NiO. Calculated electron densities for the electrolyte, Ni, NiO, Li_2O and expected electron density of the fully lithiated NiO layer (Ni + Li_2O) are shown by dotted lines for comparison and were tabulated in Table 2.1.

Figure 2.15B. At approximately 0.7 V, the same low electron density region at the Ni/NiO is observed to form, with deeper cycling resulting in a similar flat profile expected for a fully lithiated sample. In both cases, the electron density at the NiO surface is shown to begin decreasing at potentials much higher than the potential for significant lithiation, suggesting some surface reaction that occurs early on, which may play an important part in the lithiation behavior of the bilayer films and NiO as a conversion anode in general.

Cross-section samples of the 5 nm Ni/6.7 nm NiO bilayer film were studied via TEM characterization to corroborate the X-ray reflectivity studies. This sample showed slower changes to the electron density during cycling, likely due to the thicker NiO layer, and was more amenable to precise analysis at high potentials. Figure 2.16A shows the overall

morphology of the bilayer film after electrochemical cycling to 1.7 V. The Ni and NiO layers were measured to be approximately 5 nm and 8 nm thick, respectively. A rough layer, < 1 nm thick, was observed at the interface between the NiO layer and the solid-electrolyte interphase (SEI) that had formed on top of the film. This layer is marked by a white arrow in Figure 2.16A. Interestingly, the position of this interfacial layer corresponds with the region of lower electron density that was observed via XRR. EELS characterization in both the low-loss and core-loss regions was carried out to confirm the composition and chemical state of the bilayer film structure after lithiation.

Figure 2.16B shows the Ni $L_{3,2}$ edges, which can be used to determine the Ni oxidation state, as previously discussed. Calculation of this intensity ratio gives the NiO (Ni^{2+}) layer a L_3/L_2 ratio of 1.58 whereas the Ni (Ni^0) layer has a L_3/L_2 ratio of 1.35. The calculated L_3/L_2 value of the interfacial layer was 1.49, suggesting it has a lower oxidation state than Ni^{2+}. However, the Ni L_3 edge of the interfacial layer has a more intense tail feature (860 eV - 870 eV) which is strongly characteristic of Ni^0.[94] Overall, TEM images together with EELS characterization suggest that the rough interfacial layer is Ni^0 rich compared to the NiO layer underneath it. Falling electron densities in the same region revealed by XRR in Figure 2.15B would suggest the initial formation Ni and Li_2O reaction products that together have a lower electron density than NiO. As such, the two characterization methods suggest that the observed changes in morphology and composition are the initial processes of NiO conversion.

The presence of lithium in the structure was also confirmed by observing the lithium K edge signature in the low-loss EELS region at 55 eV. Figure 2.17 shows a HAADF STEM image of the bilayer structure. The Ni and NiO layers can be easily distinguished

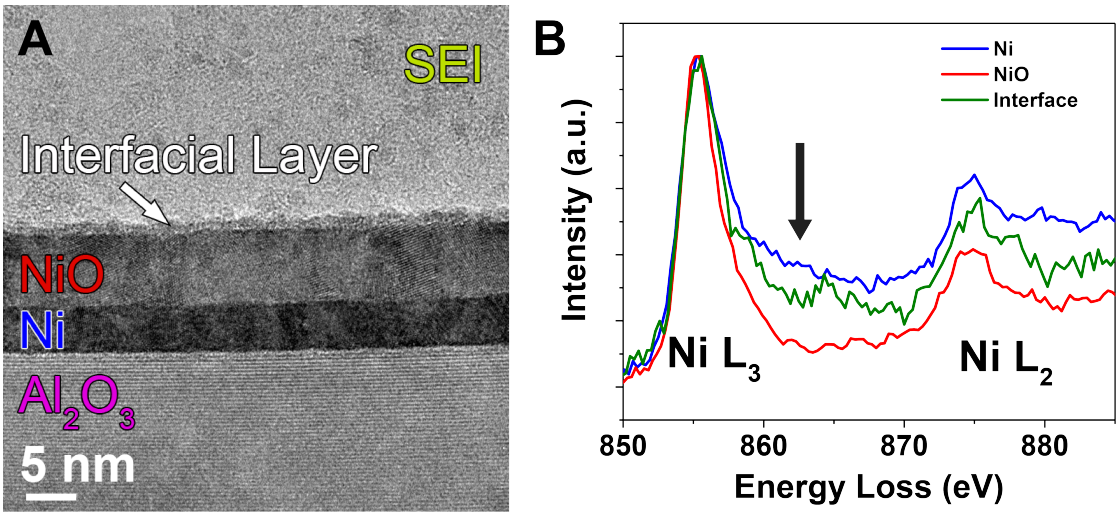

Figure 2.16. TEM and Ni EELS analysis of Ni/NiO Bilayer (5 nm Ni/6.7 nm NiO) cycled to 1.7 V. A) HRTEM image of cross-section morphology, showing the <1 nm interfacial layer that formed. B) Core-loss EELS spectra of the Ni L $_{3,2}$ edges collected from the Ni (blue), NiO (red), and interfacial layers (green) in the cross-section. A black arrow marks the high intensity tail of the Ni L_3 edge that is characteristic of Ni^0.

as the bright and dark layers respectively, as the difference in average atomic number strongly affects image contrast in HAADF STEM. An EELS linescan was collected across the entire bilayer film structure as marked by the green line in Figure 2.17A. The spectra collected from each layer region were integrated to maximize EELS signal and are shown in Figure 2.17B. This approach reduces the spatial resolution of the EELS linescan, making analysis of the interfacial layer not possible, but the increased signal does reveal presence of Li in the structure. The SEI layer clearly shows a strong lithium K edge with a fine structure suggesting LiF.[75] Furthermore, the NiO layer shows the presence of Li with a small feature at 60 eV that corresponds to the maxima in the Li K edge. Reference spectra of this energy region for NiO before and after lithiation are shown in Figure 2.18. This reinforces the in-operando XRR findings that in addition to the formation of an

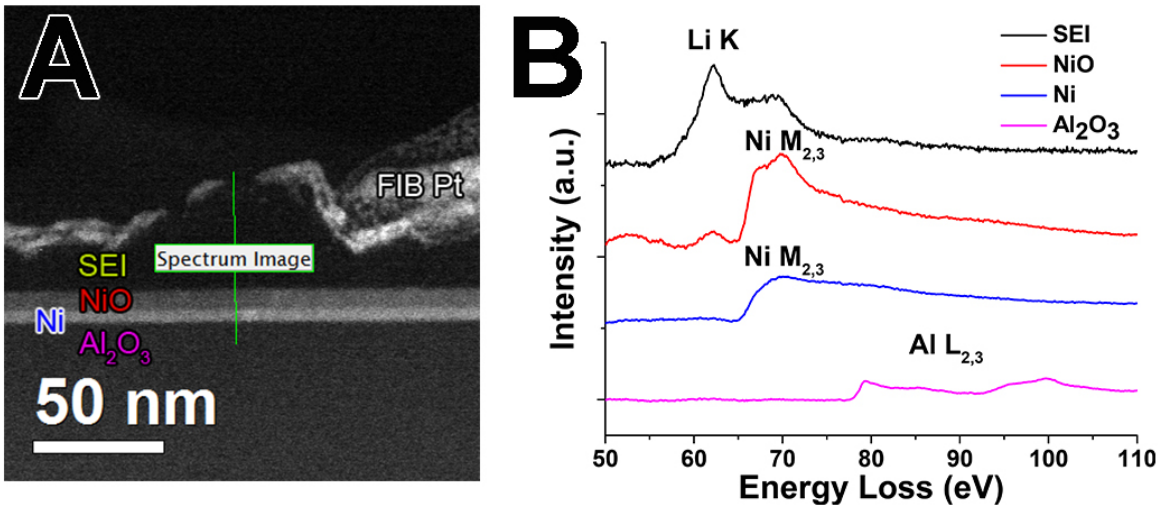

Figure 2.17. STEM and EELS analysis of Ni/NiO Bilayer (5 nm Ni/6.7 nm NiO) cycled to 1.7 V. A) HAADF STEM image of the Ni/NiO bilayer cross-section. The green line marked "spectrum image" denotes the range of the EELS linescan. B) Integrated low-loss EELS spectra of the different film layer regions.

interfacial layer at 1.7 V, there is some diffusion of Li into the NiO layer before significant conversion occurs.

The combined XRR, TEM, and EELS analysis here showed overall the presence of structure and composition evolution in the Ni/NiO bilayer at high potentials ($\sim$ 1.8 V) even though complete lithiation and conversion happens primarily at much lower potentials. In specific, there is the formation of a very thin $<$ 1 nm interfacial layer that is rich in Ni metal. EELS also shows evidence of Li insertion into the NiO top layer without any noticeable conversion occurring. These observations match the decrease in electron density observed via XRR analysis. This result further highlights the complex conversion reaction mechanism and its effects on electrode structure at various points of electrochemical cycling. It is likely that the formation of any interfacial layer early in the

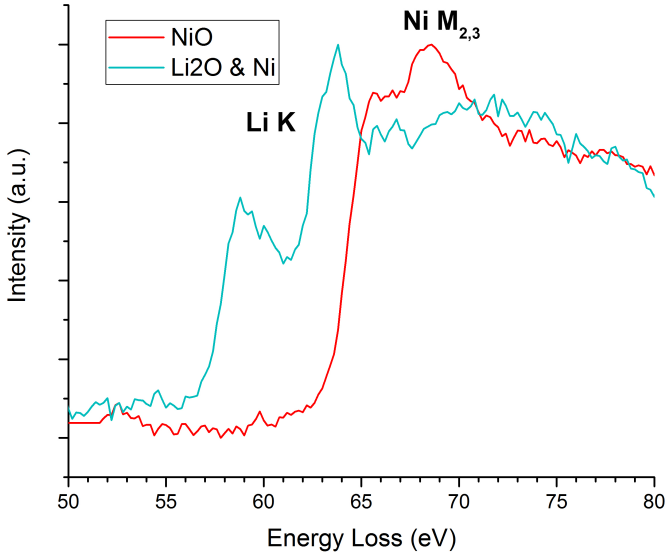

Figure 2.18. Comparison of Low-Loss EELS region of NiO bilayer before and after lithiation. The lithium K edge which emerges after lithiation is easily distinguishable from the nickel $M_{2,3}$ edge in the same energy region. The fine structure of the nickel edge also changes after reduction.

electrochemical cycle inhibits lithiation and contributes to the electrode overpotentials. However, more work is needed to understand the complete reaction mechanism.

2.4.3. Observation of Lithiation and Conversion in Ni/NiO with In-Situ TEM

The work presented so far featured XRR and TEM characterization of Ni/NiO multilayer structures together to deeply understand the reaction mechanism and conversion process. However, the TEM analysis of these multilayers was solely done ex-situ, after lithiation to different potentials. Observing the lithiation and conversion of these multilayer structures could reveal additional nanoscale reaction mechanisms that are not detected using solely x-ray based techniques. It actually is possible to do in-situ experiments using TEM to probe the lithiation and delithation reaction inside the microscope and in real time. There

is a wide body of literature that has done in-situ TEM biasing experiments on lithium ion battery materials, including NiO nanosheets.[95–97]

The in-situ lithiation experiment is done by using a specialized in-situ TEM sample holder that allows one to add an electrical bias to a sample to prompt a reaction. Figure 2.19 shows a schematic of the holder used for these experiments. Typically, the active material of interest is mounted to a conductive Au wire that is connected to the holder. Pure lithium metal is then mounted to a W wire and attached to the holder through a piezoelectric stage. This stage enables nanoscale motion to bring the active material and lithium metal into contact and start the lithiation reaction. The in-situ holder used has an 'open-cell' geometry that lacks the presence of a liquid electrolyte necessary for operation of a real battery. Removing this liquid electrolyte adds a degree of separation between the observations and the real battery phenomena, but also removes several complex technical issues that come with using liquids inside the TEM. Nevertheless, the electrolyte in the system is generally understood to be the Li_2O surface oxidation layer that forms on the lithium metal during brief air exposure from handling.

Conducting in-situ experiments also requires a sample that is electron transparent and has a compatible morphology for the holder. The FIB cross-section samples that were examined in previous sections are not optimal, as the region of interest is very small and challenging to locate, and the lithiation process cannot be easily controlled to match the top-down mechanism observed in the bulk multilayer sample. On the other hand, nanowire samples are often used for in-situ experiments because of the ability to locate many different regions of interest, and observe the reaction clearly proceed in one sample direction.[98–100]

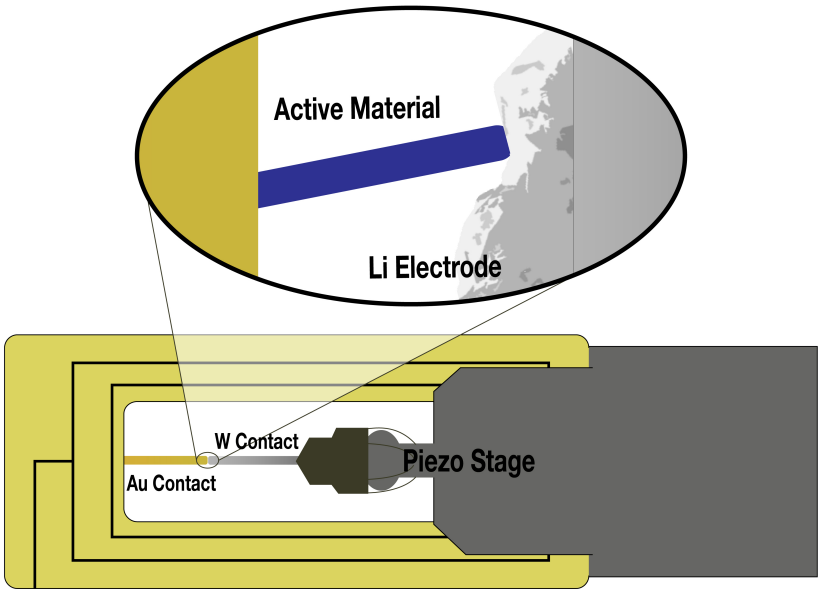

Figure 2.19. Schematic of the In-Situ Electrical Biasing TEM holder used. The holder has an open-cell geometry, and direct contact between lithium metal and the active material enables the reaction of interest to proceed.

It is possible to synthesize nanowires with transition metal or transition metal oxide compositions using a templating synthesis method. This method uses an anodized aluminum oxide (AAO) porous template with a deposited metal electrode. The electrode promotes electrochemical deposition of various transition metals into the pore lengths, and the entire template can be then etched away to leave the nanowires behind. The pore width of the AAO template is tunable and defines the nanowire diameters, with the pore length and deposition parameters affecting the nanowire length.[88] This method is summarized in Figure 2.20A.

Figure 2.20B shows Ni nanowires synthesized using the AAO template method, with a $\sim$ 50 nm width and 3 - 5 micron lengths. SAED patterns confirmed the Ni structure, along with EELS. The Ni nanowires can be oxidized in the template to generate NiO nanowires, which are shown in 2.20C and also show a NiO composition via SAED. The

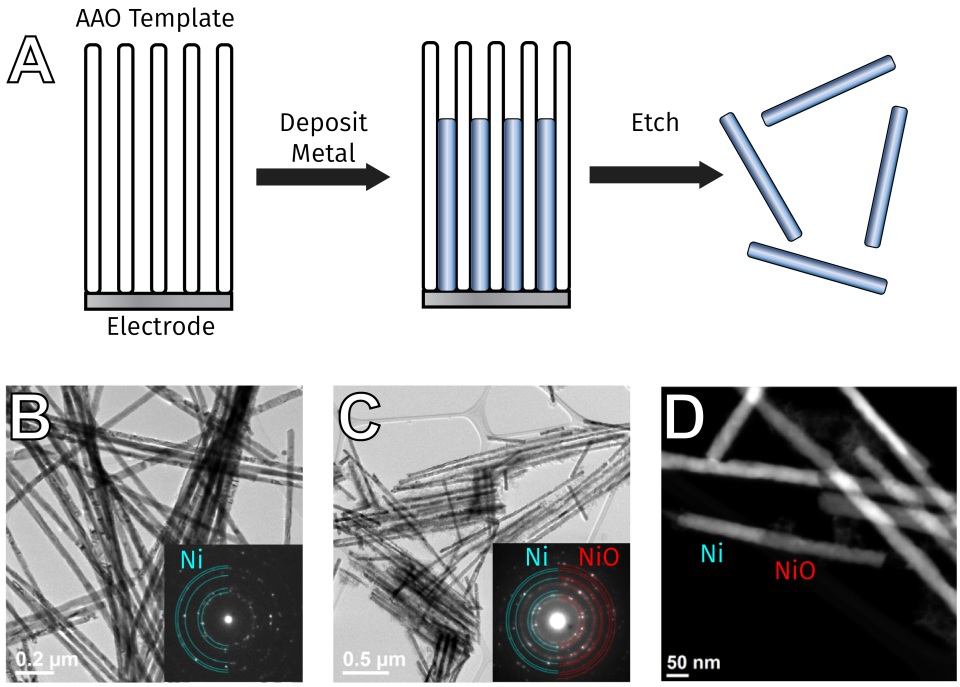

Figure 2.20. Template Synthesis and Characterization of Transition Metal and Transition Metal Oxide Nanowires. (A) Template synthesis process. (B) TEM image of Ni and (C) NiO nanowires. SAED patterns are inset in both figures to confirm their structure. (D) HAADF STEM image of NiO/Ni nanowires, highlighting the contrast difference in composition.

oxidation parameters can be also turned to form NiO/Ni nanowires with two different compositions along the length of the nanowire. This nanowire composition is shown in Figure 2.20D, with notable image contrast in the HAADF STEM image.

The Ni/NiO nanowires shown in Figure 2.20D were loaded into the in-situ biasing TEM holder to observe the lithiation and conversion reaction in the 'bilayer' nanowire. Figure 2.21A shows the NiO/Ni nanowire that was identified and isolated for the in-situ experiment, with dimensions of ∼560 nm in length and 35 nm in diameter. Again, the HAADF STEM image showed the distinct contrast difference between the two halves and confirmed the composition. The lithium electrode was positioned to come into contact

with the NiO end of the nanowire and begin the lithiation process. Figures 2.21B,C show HRTEM images of the nanowire after the conversion, with Figure 2.22 showing the dynamic progression of the nanowire lithiation. Lithiation begins rapidly, with the nanowire quickly losing its uniform contrast corresponding to a NiO composition. As the conversion process proceeds, a dark and speckled contrast forms in the lithiated regions, corresponding to the formation of Li_2O and $\sim$ 2 nm Ni metal particles. As the nanowire becomes increasingly lithiated, the diameter expands and some buckling or shearing of the nanowire is observed after 31 seconds in Figure 2.22B. Furthermore, there is a clear conversion reaction front that proceeds along the length of the nanowire, which is marked by black arrowheads in 2.22. However, there is expansion of the nanowire diameter ahead of the conversion reaction front that suggests the presence of lithium diffusing along the surface of the nanowire ahead of the observed conversion reaction front, as marked by a red arrowhead in Figure 2.22C.

As the reaction front approaches the Ni segment of the nanowire, the NiO region along its path shows intense dark contrast regions that can be seen in Figure 2.22C-G. This contrast is caused by the buildup of stress and the formations of dislocations as lithium enters the structure and begins the conversion reaction.[98] This contrast also becomes more prominent as the reaction front approaches the NiO/Ni interface, as the rigid Ni region does not allow for stress in the nanowire to be relaxed by much of the bending and bucking that is observed in 2.22C-I. The conversion reaction front also transforms from having a flat interface with the unreacted NiO region to having a 2-pronged reaction front first observed in 2.22E. These features resemble the 'finger-modes' reported in the lithiation of NiO nanosheets, which occur as a result of the stress buildup in the nanowire surface. It

was also noted that there is an 'incubation time' of $\sim$ 100 s for this reaction mechanism to occur, which is consistent with the 108 s reaction time where the 2-pronged reaction front was first observed.[55]

It was expected that the NiO/Ni interface may promote heterogeneous nucleation of Ni particles, causing a conversion reaction at the interface before the remainder of the bulk conversion reaction front reached the interface. Figures 2.22G,H show the moments where the reaction front approached the NiO/Ni interface. Although there are regions of the pronged reaction front in contact with the NiO/Ni interface (marked by the red arrowhead), there is no observed speckled contrast indicating conversion at the interface before the bulk reaction front had reached the interface. There are some dark fringes or striations observed in Figure 2.22G at the NiO/Ni interface, but the cause of these features is uncertain. The bulk reaction front quickly reaches the NiO/Ni interface afterwards, as seen in Figure 2.22H. Continued lithiation of the NiO/Ni nanowire shows surface diffusion of lithium onto the Ni region of the nanowire in Figures 2.22J-L, which is marked by the red arrowhead. There is some speckled contrast that appears at the surface of the nanowire, indicating lithiation and conversion of a thin oxide surface layer on the Ni region of the nanowire. However, additional lithiation ($>$ 100 s more) causes only surface deposition or plating of lithium.

Figures 2.21B,C show images of the NiO/Ni nanowire sample after lithiation and conversion. The overall nanowire showed significant buckling and bending of the NiO region as it underwent the conversion reaction, giving it a curved shape as seen in 2.21B. There was no significant expansion in the nanowire length, however there were regions of the reacted NiO region with diameters between 50 - 70 nm compared to the initial 35

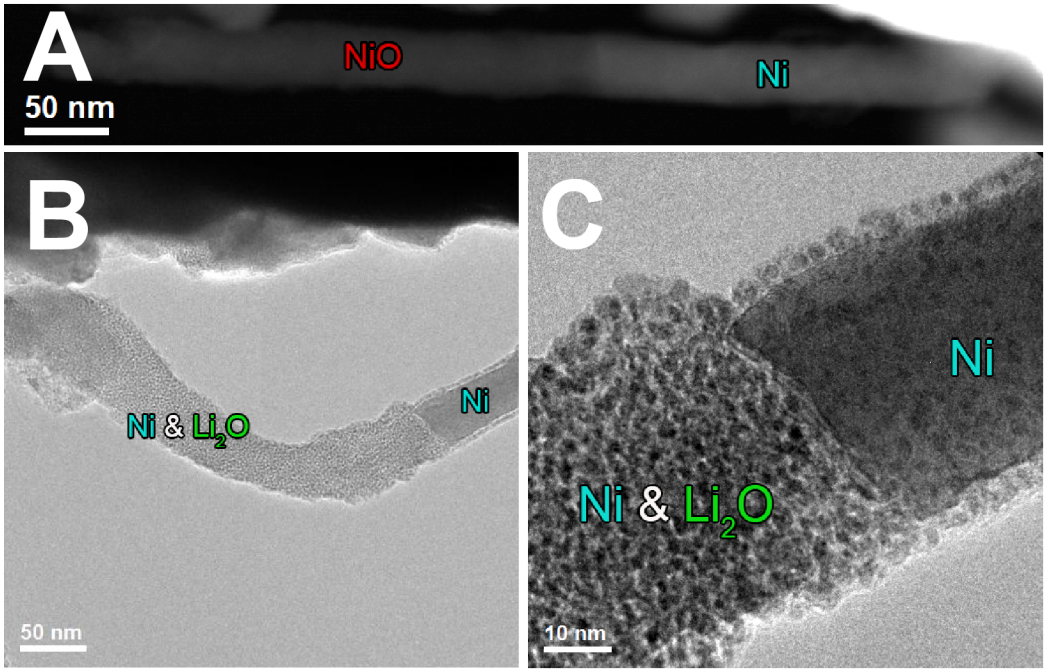

Figure 2.21. In Situ Lithiation of Ni/NiO Nanowires. (A) HAADF STEM of the Ni/NiO nanowire before lithiation and conversion. (B) HRTEM image of the entire Ni/NiO nanowire after lithiation. (C) HRTEM image of the Ni/NiO interface after lithiation.

nm diameter of the pristine nanowire– near 100% expansion in diameter, consistent with the results of the multilayer stacks in previous sections of this chapter. This doubling of the nanowire diameter translates into a near 400% volume expansion along the length of the nanowire (approximated as a cylinder). Figure 2.21C highlights the NiO/Ni interface after lithiation and conversion, which shows a high density of Ni nanoparticles with sizes ranging from 2 - 4 nm.

The observed lithiation mechanism and presence of a 'pronged' reaction front echoes previous literature and suggests that this reaction mechanism is generalized to various sample morphologies. Although there was no early conversion observed at the NiO/Ni interface of the nanowire, surface diffusion of lithium was observed ahead of the bulk reaction

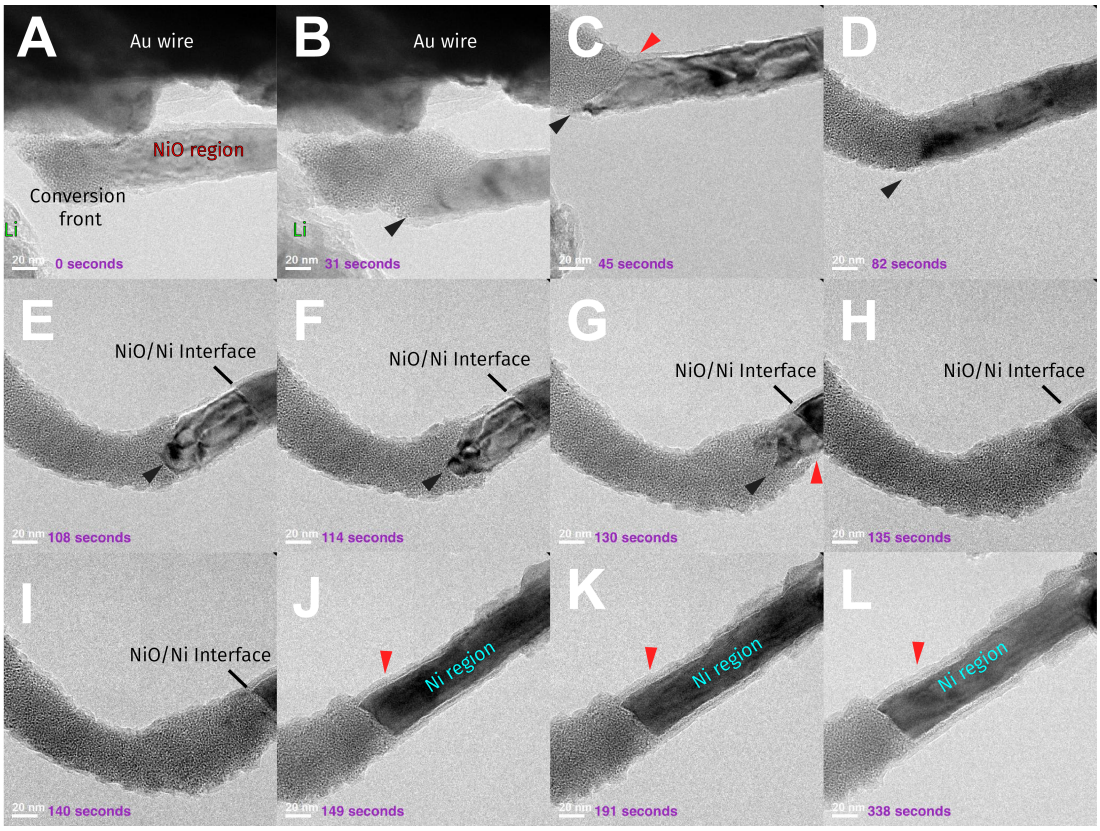

Figure 2.22. In Situ Lithiation Front Progression Through Ni/NiO Nanowire. (A-L) HRTEM images showing the progression of the reaction front during lithiation. The reaction time is marked for each image. Black arrowheads mark the progression of the reaction front through the nanowire. Red arrowheads mark regions of interest discussed in the text.

front. It is possible that this observation can help explain the high-potential formation of an interfacial layer in the NiO/Ni bilayer structure discussed in Section 2.4.2. Moreover, the large degree of buckling and bending in the free standing nanowire lends credence to the effectiveness of the multilayer structure controlling expansion/contraction of the electrode and improving overall cycling stability. Nevertheless, the NiO/Ni nanowire is distinct from the multilayer structures discussed in the previous chapters. Surface diffusion of lithiation likely plays a much larger role in this in-situ experiment, and the

presence of a liquid electrolyte is not accounted for. Moreover, the NiO/Ni interface formed resembles more the NiO bulk conversion phenomena than the nanoscale confined NiO interdigitated layers in the structure. This could be more closely matched by using nanowires with a Ni-core and NiO-shell morphology, which can also be attained using the AAO templating method. Lastly, spatial and temporal resolution of these experiments would improve with aberration corrected microscopy and enhanced high-speed cameras.

2.5. Summary and Outlook

This section focused on studying the conversion reaction as an alternative materials chemistry for lithium ion batteries with significantly larger charge capacities. Unfortunately, the conversion reaction brings significant challenges that must be understood at a fundamental level – structure and morphology degradation limit ion and charge transport, and can affect reaction kinetics and lithiation potentials. These changes have direct relationships to sub-par battery performance. Understanding these fundamental electrochemical phenomena would benefit not only the conversion reaction but energy storage and conversion materials systems in general.

The multilayer structures described here prove to be effective at enabling reversibility through structural stability, but more work needs to be done to understand the chemical contribution to cycling performance. A combined XRR and TEM approach showed the layered structure evolution caused by lithiation. Significant volume expansion was observed, as expected. But the limits for lithium transport were drawn and the separation of lithium at the interfacial layers showed the layered structure's ability to promote the conversion reaction at the interface.

The simplified Ni/NiO bilayer structure was used to observe structure and composition evolution that occurs early in the lithiation process, at the theoretical lithiation potential. The formation of a thin interfacial layer could help explain some of the overpotentials that afflict the conversion materials.

Probing the conversion process with in-situ TEM showed different lithium transport mechanisms at play – both surface diffusion of lithium and the uneven multi-pronged reaction front that proceeded through the NiO/Ni nanowire. It is clear that these kind of effects are likely at play in the multilayer structure, and that further studies are needed to more closely match the electrochemical environment found during lithiation of the multilayer structure.

Overall, these findings do suggest that multilayered structures could be a good way of controlling the anode, as the multilayered structures retained their morphology for the most part. In comparison, the NiO/Ni nanowire showed volume expansion in multiple directions and significant bending and buckling as it had no significant morphological control in place. The varying elemental distribution in the multiayer structure also highlights the need for simple oxide systems like NiO, which already have complex reaction mechanisms despite their chemistry being 'simple' at face value (see Equation 2.1).

The prospects for conversion materials remain hazy. The route to commercialized technology requires mastery over the chemistry, processability, *and* manufacturability. To date, progress is needed in all three categories. The strategy of utilizing a multilayered structure is a good starting point for improving cyclability performance, but improvements are needed to form this architecture on a cost-effective and conducting substrate with higher-throughput methods than PLD. Moreover, the anode composition must be

optimized to balance sustainability and battery performance. The Ni/NiO system is a good model for studying the conversion reaction, but is not the optimal battery material system. Driving further improvements in intercalation materials still is a promising and necessary route towards achieving higher performance batteries.

CHAPTER 3

Structure Evolution and Oxygen Electrochemical Activity in Lithium-Rich Li_2IrO_3

3.1. Chapter Overview

Alternative materials chemistries like the conversion reaction discussed in Chapter 2 provide significant theoretical gains to charge capacity. However, performance gains can still be achieved in more 'traditional' intercalation materials by increasing the stored lithium content or better utilizing the full range of reactivity of each chemical species in the compound. To this end, one class of intercalation materials, known as Li-rich materials, increase the amount of lithium stored in the crystal structure by including lithium ions in both the interlayer gaps and the metal oxide layers themselves. Moreover, the additional lithium storage in these materials enables the possibility of oxygen oxidation as part of the charge compensation mechanism – a phenomenon which does not readily occur in standard intercalation materials like $LiCoO_2$.

This chapter explores the phenomenon of oxygen reduction-oxidation reactions in the model system Li_2IrO_3. This model system is isostructural with Li_2MnO_3, one of the commonly studied Li-rich materials, but does not have the structural degradation issues that occur upon delithiation, making it a stable material for analyzing changes in the electronic states of oxygen. A combination of characterization methods are used to probe these changes in oxygen, including DFT calculations, TEM, EELS, and X-Ray Absorption

Near Edge Spectroscopy (XANES). Each technique provides correlative data to show the phases of delithiation where oxygen oxidation and contribution to charge capacity may be expected. In particular, removal of 1 Li formula unit to yield $LiIrO_3$ results in the formation of oxygen hole states but no oxygen oxidation until higher levels of delithiation above 4 V. This work further emphasizes the need for multiple analytical methods to develop a deeper understanding of materials and electrochemical phenomena.

The work described here is part of the following manuscript: Li, L., Castro, F.C., Park, J.S., Li, H., Lee, E., Boyko, T.D., Freeland, J.W., Yao, Z., Fister, T.T., Vinson, J., Shirley, E.L., Wolverton, C., Cabana, J., Dravid, V.P., Thackeray, M.M., & Chan, M.K.Y.. Probing Electrochemically-Induced Structural Evolution and Oxygen Redox Reactions in Li-Rich Layered Cathode Materials, *in preparation*.

3.2. Introduction

The most used and widespread lithium ion battery materials are based on intercalation chemistry, as discussed in Chapter 1, which enable long cycling lifetimes and good energy density.[6,10] However, their practical charge capacity is often much lower than their theoretical capacity, as it is directly linked to the amount of lithium that can be reversibly inserted and extracted from the crystal structure. For example, the practical charge capacity of $LiCoO_2$ is less than half of its theoretical capacity, as removal of more than 0.5 Li from $LiCoO_2$ causes structural instability and irreversible phase transformations that lead to capacity or voltage decay which severely hinder their performance.[101–104]

As such, increasing the lithium content in a material, or improving how much lithium can be reversibly extracted, will both lead to improved charge capacities. Li-rich transition

metal oxides are one class of electrode materials that have been actively explored for increasing the lithium content and improving stability in the electrode.[105–109] These oxides generally have a form of $Li_{1+x}M_{1-x}O_2$. They have the same layered crystal structure as normal intercalation materials, but with an excess of lithium ions that occupy the interlayer gaps in the layered structure in addition to lattice sites within the metal oxide layers. This excess lithium leads to an increase in charge capacity, but can also cause unwanted phase transformations in the materials due to migration of transition metals to lattice sites in the interlayer gaps or sliding of layers to have a different stacking order.[109–112]

Li-rich materials are also of interest due to their reported ability of having the oxygen anions participate in the charge compensation after removal of a lithium ion, in addition to oxidation of the transition metal species. This compensation mechanism may have some increase in the charge capacity available to the electrode materials, but often happens concurrently with irreversible oxygen loss from the electrode.[113] DFT calculations have suggested that this additional oxygen chemistry occurs due to Li-O-Li bonds that form when lithium ions occupy lattice sites in the oxide layers. This Li-O-Li bonding scheme generates O $2p$ lone pairs that can be more easily utilized in redox processes compared to standard layered intercalation materials.[114]

Li_2MnO_3 is one of the most studied Li-rich materials, and suffers from the degradation issues mentioned during cycling.[115,112] On the other hand, Li_2IrO_3 is isostructural with Li_2MnO_3 but has better cycling stability. Literature reports show that Li_2IrO_3 can reversibly cycle 1 Li formula unit without migration of the Ir atoms outside of the oxide

layers, and that there is possible formation of O-O dimers upon delithiation which indicate oxygen oxidation ($2\ O^{2-} \rightarrow {O_2}^n$, where $n = 1, 2, 3$).[116] Li_2IrO_3 is not a practical battery material due to the high cost of Ir, but is a good model system to study the oxygen reactivity thanks to its structural stability with delithiation.

This chapter describes a combined TEM, DFT, and X-ray characterization approach to study the structural evolution of Li_2IrO_3 alongside changes to the oxygen electronic structure that may indicate oxygen oxidation. In particular, DFT calculations show the structural transformation of $Li_{2-x}IrO_3$ during delithiation, which matches the experimental voltage profile and is confirmed via TEM. XANES and EELS are combined to probe the evolution of Ir-M and Li-K edges during delithiation, along with a deep analysis of the O-K edge fine structure. The O-K edge shows the formation of a split pre-edge peak which is also seen via DFT calculations. These results suggest varying oxygen activity based off of changes to the electronic structure. Namely, oxygen holes form early in the delithiation procedure but oxygen oxidation, and additional charge capacity, only occur at higher degrees of delithiation (charging $>$ 4 V). Using this result, it may be possible to tune future electrode compositions to better utilize oxygen oxidation and deliver additional charge capacity.

3.3. Materials and Methods

3.3.1. Synthesis Methods

Li_2IrO_3 powder samples were prepared by solid-state synthesis. Stoichiometric amounts of lithium carbonate (Li_2CO_3) and iridium oxide (IrO_2) were thoroughly mixed with a mortar and pestle. The precursor mixture was pressed into a pellet and fired in air at 950

$^{/}circ$C for 2 days. The heating rate was 2 $^{/}circ$C /min, while the cooling rate was not controlled.

3.3.2. Electrochemical Characterization

Electrochemical characterization was conducted with 2032 type coin cells assembled in an Ar-filled box. A homogeneous slurry containing Li_2IrO_3 powder (84 wt %), carbon black (8 wt %), and polyvinylidene difluoride binder (8 wt %) was prepared with an N-methyl-2-pyrrolidone solvent and coated on aluminum foil. The electrode laminate was dried in a vacuum oven overnight, and electrode discs (12.7 mm in diameter) were punched out for coin cell tests. The typical active material loading was 3 mg/cm^2. A lithium metal disc was used as the anode, and the electrolyte was 1.2 M lithium hex-afluorophosphate dissolved in a 3:7 mixture solvent of ethylene carbonate and ethyl methyl carbonate . The electrochemical charge-discharge tests were conducted at 25°C in a temperature-controlled chamber.

3.3.3. Density Functional Theory (DFT) Calculations

DFT calculations were performed to model the structural and thermodynamic properties of $Li_{2-x}IrO_3$. They were done using the plane wave code VASP27 with projector augmented wave (PAW) potentials for core electrons.[117] Due to the large computational load in sampling the configurational spaces of $Li_{2-x}IrO_3$, the soft version of the oxygen PAW atom potential supplied by VASP was used, in conjunction with a kinetic energy cutoff of 353 eV. Various types of exchange-correlation functionals were evaluated, including the standard generalized-gradient approximation (GGA) with the parametrization of

Perdew-Burke-Ernzerhof (PBE), and modified functionals with dispersion (van der Waals) corrections. The on-site Coulomb interaction was accounted for by adding a Hubbard-U term, with a U value of 1.0 eV adopted from a previous study.[118,119]31 All calculations were spin-polarized. The Brillouin-zone integration was performed using a Γcentered grid with a k-point spacing less than 0.35 $Å^{-1}$ in the reciprocal space. The electronic energies near the Fermi level were smoothed using the Gaussian smearing technique with a smearing width of 0.05 eV. The lattice parameters and positions of all atoms were allowed to relax until the total-energy difference between two consecutive self-consistent iterations was less than 10^{-4} eV. The structures of $Li_{2-x}IrO_3$ on the constructed convex hull (x=0, 1 and 1.5) obtained with PBE + U were further relaxed using the Heyd-Scuseria-Ernzerhof (HSE) screened hybrid functional, including spin-orbit coupling(SOC).[120] The density of states (DOS) of these three structures were computed accordingly.

The XANES simulations were performed using the OCEAN package that implements the Bethe-Salpeter equation (BSE), which is built upon a DFT ground-state calculation.[121] The ground-state charge density, and the wave functions used in core-hole screening and BSE calculations were obtained using the Quantum Espresso package.[122] The local-density ap-proximation (LDA) was used as the exchange-correlation functional. Norm-conserving pseudopotentials from the ABINIT distribution were used, in conjunction with a cutoff energy of 952 eV.[123] The size of the k-point grid used to solve the Kohn-Sham states was 6×4×6 for pristine (24-atom cell) Li_2IrO_3, and was adjusted according to the size of other simulation cells. A 12×9×12 k-point grid yields essentially the same result for pristine Li_2IrO_3. The screening calculations for all the structures used a 2×2×2 k-point grid. The number of unoccupied bands used for the BSE calculation

was 500, and the screened core-hole potential calculation included 800 bands. It should be noted that the number of bands influences the range of energies in which the spectra are reliably simulated. When 800 and 1200 bands were used for the BSE and screening calculation, respectively, no obvious differences in the spectra were found in the energy range up to 40 eV above the edge. Only dipole-allowed transitions were considered. The photon polarization vectors were set at [100], [010] and [001], and the final spectrum of each structure was obtained by averaging the spectra generated from using each of the polarization vectors.

3.3.4. X-Ray Characterization

XANES were performed for pristine and cycled samples in the electron (surface) and fluorescence yield (bulk) modes at beamline 4-ID-C of the Advanced Photon Source. Samples were transferred from a glovebox into a transfer container and then an X-ray absorption chamber via an argon environment. This was done in order to maintain a clean sample. During the measurements, the oxygen K edge was energy calibrated using a Sr_2RuO_4 reference measured simultaneously with the sample XAS. For the Ir M_3 edge, the energy reference was the Mo L edge. Iridium L_3 spectra were measured on cycled laminates using transmission-mode x-ray absorption spectroscopy at sector 10BM of the Advanced Photon Source. Samples were sealed using aluminized mylar to minimize oxygen and moisture exposure.

3.3.5. TEM Characterization

TEM analyses were done using a JEOL 2100 FasTEM, equipped with a Schottky field-emission electron gun operating at 200 kV. This TEM is equipped with a Gatan GIF camera system for high resolution TEM imaging. The JEOL 2100 was also operated in STEM mode to conduct HAADF STEM imaging and EELS. EELS were collected using a Gatan Enfina EELS spectrometer. The energy resolution for the EELS was 1.0 eV, based on the full-width half-maximum value of the EELS zero-loss peak. Furthermore, a convergence angle of 8.4 mrad and collection angle of 14 mrad were typically used in spectra acquisition. After electrochemical cycling, the cells were disassembled in a glovebox, and the active material was rinsed of electrolyte. TEM samples were prepared by scraping $Li_{2-x}IrO_3$ off the current collector and onto a copper-mesh TEM grid with a lacey carbon support film. Typical step sizes for the EELS linescans shown were 5 nm.

3.4. Results and Discussion

3.4.1. Structure and Cycling Behavior of $Li_{2-x}IrO_3$

Li_2IrO_3 has a monoclinic C2/m crystal structure, with layered metal oxide octrahedra as with other layered intercalation materials. However, its Li-rich nature also originates from the lithium atoms that are present within the octrahedral planes in the 2a Wyckoff positions as seen in Figure 3.1. Li_2IrO_3 has a distinct ABCABC oxygen stacking sequence known as O3 stacking, which transforms in to a ABABAB O1 stacking sequence during significant delithiation due to the sliding of oxide layers. Delithiation of the structure is possible down to a $Li_{0.5}IrO_3$ stoichiometry, at which point all lithium in the 2a Wyckoff

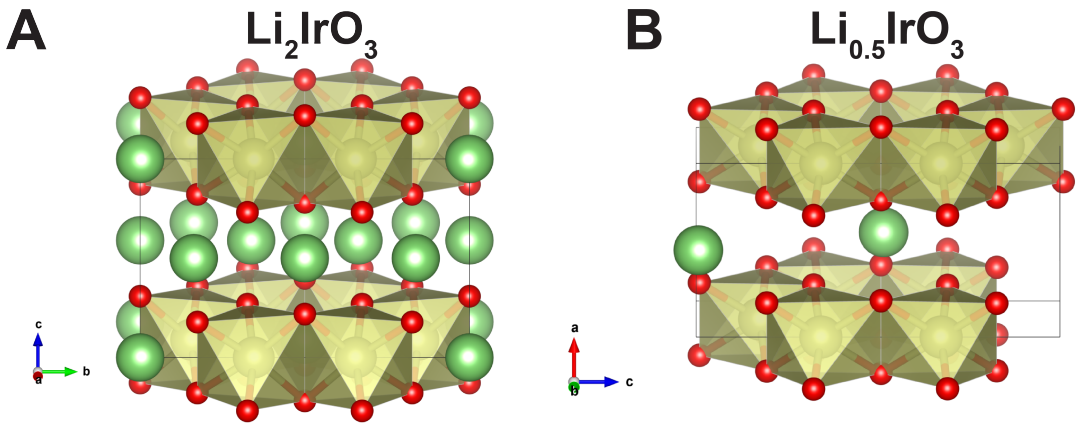

Figure 3.1. Crystal Structure of $Li_{2-x}IrO_3$ Iridates. (A) Li_2IrO_3. (B) $Li_{0.5}IrO_3$. Iridate octahedra are colored tan. Lithium atoms are colored green and oxygen atoms are colored red.

positions has been removed, and the remaining lithium atoms occupy only the 2c Wyckoff positions in the interlayer gap.

Li_2IrO_3 was electrochemically cycled to varying states of charge in order to examine changes in the oxygen content and chemical state in the structure. Figure 3.2 shows the voltage profile of the lithiation and delithiation cycles, with Roman numerals indicating the different states of charge that were investigated and will be discussed later. Cycling occurred between 2.0 V and 4.6 V using a C/20 rate, giving a first-cycle charge capacity of 160 mAh/g indicating removal and insertion of 1.5 Li units. Overall, two main plateaus were observed in the voltage profile, at 3.5 V and 4.1 V indicating two separate electrochemical processes. This electrochemical performance is consistent with what was previously reported in the literature.[116]

A combination of DFT and TEM analysis was done to determine the chemical change and structure evolution of $Li_{2-x}IrO_3$ during different states of charge. Namely, DFT calculations determined the theoretical voltage profile that closely matched the experimental

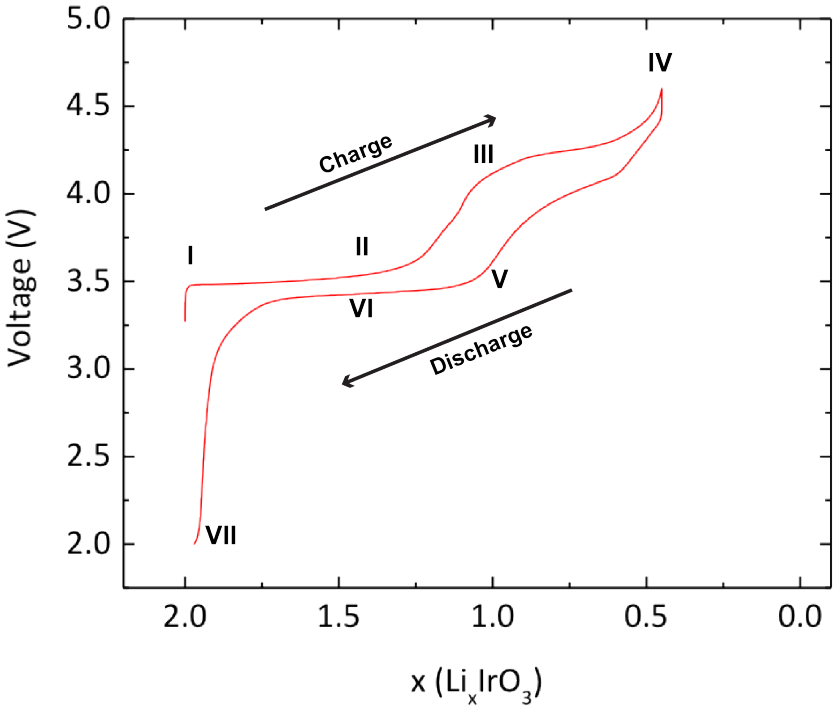

Figure 3.2. First Electrochemical Discharge and Charge Cycles for $Li_{2-x}IrO_3$. Roman numerals mark the states of charge discussed in the main text.

one. These calculations predicted that the first plateau in the voltage profile (marked II) corresponded to delithiation and removal of 1 formula unit of Li to leave an $LiIrO_3$ stoichiometry ($x = 1.0$ in $Li_{2-x}IrO_3$) while the second plateau (III) corresponded the onset of additional delithiation of 0.5 Li formula units to result in a $Li_{0.5}IrO_3$ stoichiometry ($x = 1.5$).

TEM and electron diffraction were used to confirm the experimental structure of $Li_{2-x}IrO_3$ at the first and second plateaus of the voltage profile and to identify any significant change in the particle morphology after cycling. Figure 3.3 shows low magnification and HRTEM images of particles from regions I, III, and IV in the cycling curve, which

should corresponds to Li_2IrO_3, $LiIrO_3$, and $Li_{0.5}IrO_3$. These images show that there is bulk-level homogeneity in the particles, and no observable defects such as cracking, structural degradation or decomposition. However, these images show particles in their first delithiation cycle. Closer examination with HRTEM images again shows minimal signs of defect formation and no signs of amorphization structural degradation that is sometimes observed.

Selected Area Electron Diffraction (SAED) of each of the three particles examined in Figure 3.3 showed the structural evolution of the $Li_{2-x}IrO_3$ particles during cycling. This analysis is presented in Figure 3.4. The pristine Li_2IrO_3 particle displayed a single-phase crystalline orientation relatively close to what was identified as the [001] zone axis of the Li_2IrO_3 C2/m structure, as expected. The SAED pattern was collected from two grains that were rotated with respect to each other, resulting in two sets of spots with the same zone axis but slightly different rotational orientations. As lithium is removed from Li_2IrO_3, the structure evolution shows a change in stacking from O3 to O1 when more than 1 Li unit is removed. The particle cycled to position III was found to have a single-phase $LiIrO_3$ structure, also as expected based on previous literature and DFT calculations. The particle cycled to position IV in the voltage profile is expected to have 1.5 lithium formula units removed and a $Li_{0.5}IrO_3$ structure. However, differentiating between $Li_{0.5}IrO_3$ and $LiIrO_3$ can be difficult because many of the diffraction rings for both phases have very similar d spacings. This condition is shown in Figure 3.4C, which was derived with the calculated diffraction ring spacings for $Li_{0.5}IrO_3$ (green) and $LiIrO_3$ (red). Some diffraction spots could not be attributed to $Li_{0.5}IrO_3$, but had d-spacings that matched with the $LiIrO_3$ [101] and [103] diffraction ring spacings (marked with red

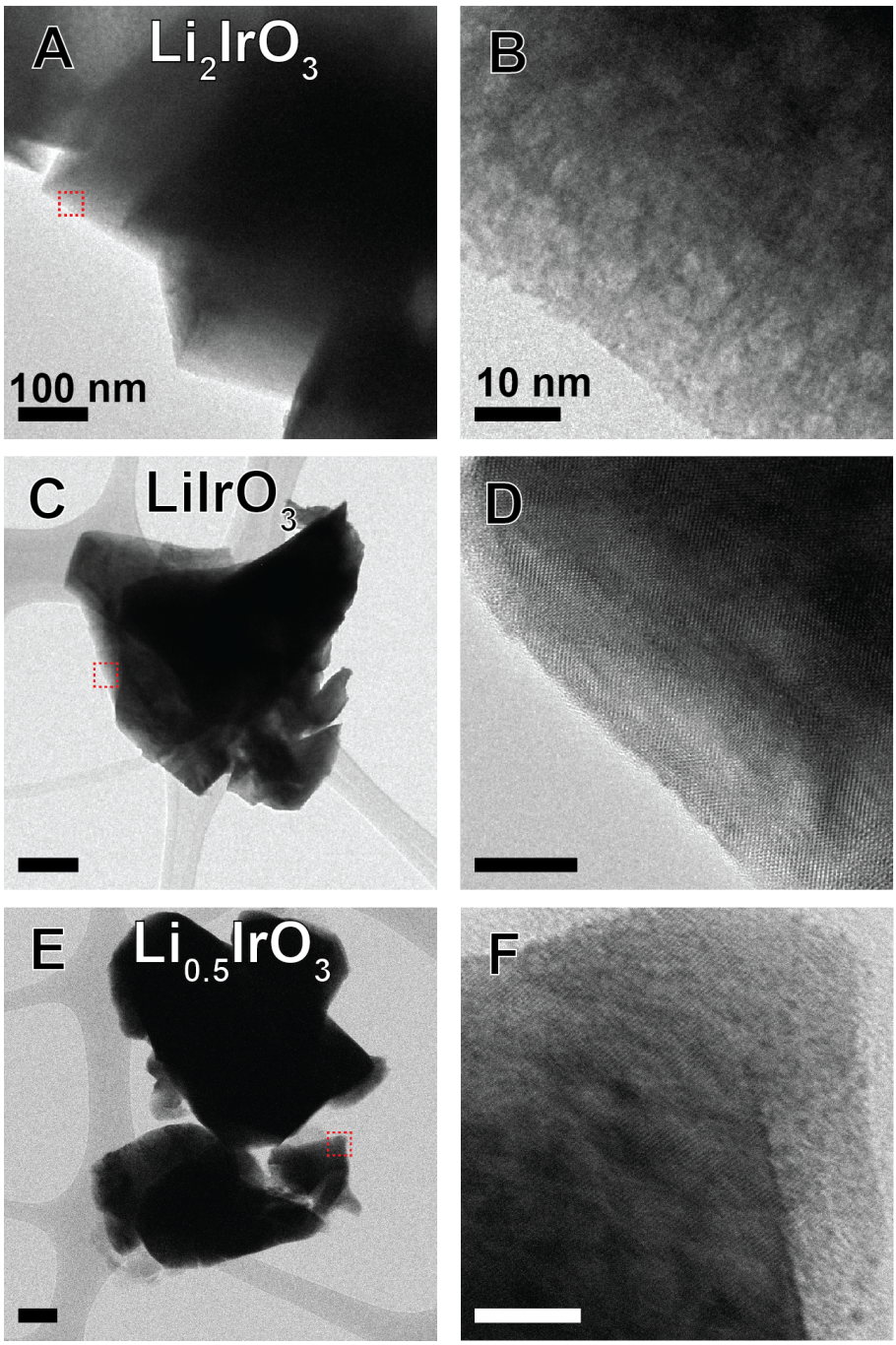

Figure 3.3. Initial TEM Analysis of $Li_{2-x}IrO_3$ (A,C,E) Low magnification TEM images of Li_2IrO_3, $LiIrO_3$, and $Li_{0.5}IrO_3$, respectively. (B,D,F) HRTEM images of Li_2IrO_3, $LiIrO_3$, and $Li_{0.5}IrO_3$, respectively. The red box in A,C,E indicates the imaged region for B,D,F. The scale bars for A,C,E are 100 nm and the scale bars for B,D,F are 10 nm.

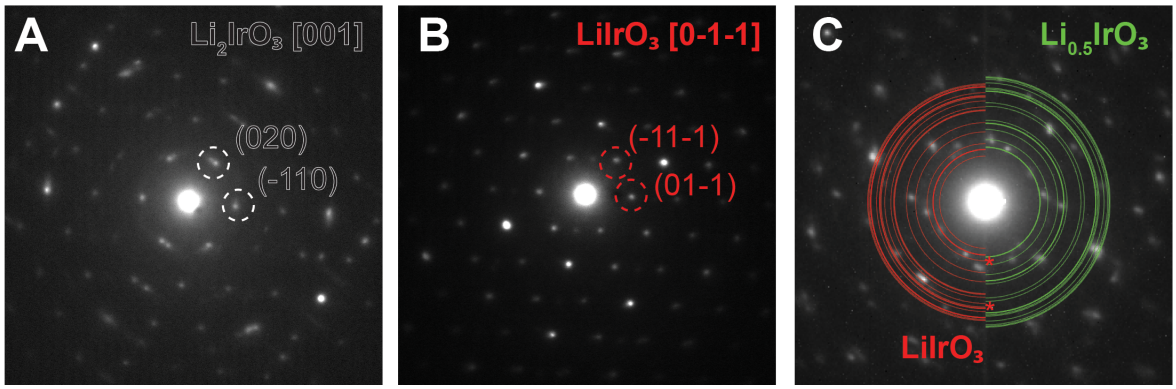

Figure 3.4. Initial SAED Analysis of $Li_{2-x}IrO_3$ (A) SAED of Li_2IrO_3 particle with [001] orientation (B) SAED of $LiIrO_3$ particle showing [0-1-1] orientation. (C) SAED of $Li_{0.5}IrO_3$ with indexed rings for $Li_{0.5}IrO_3$ (green) and $LiIrO_3$ (red).

asterisks). It is reasonable that some residual $LiIrO_3$ may be present in the $Li_{0.5}IrO_3$ sample at the nanometer scale, as extraction of 1.5 Li is reached at the upper cutoff voltage for electrochemical cycling, and the delithiation reaction may not have been fully completed across the entire sample.

3.4.2. Spectroscopic Analysis of $Li_{2-x}IrO_3$ and Oxygen Electrochemical Activity

TEM and SAED analysis confirmed the DFT structural predictions at different states of charge in the voltage profile. Determining changes in oxygen due to electrochemical cycling, however, requires some spectroscopic characterization and analysis. STEM-EELS is one method of examining the oxygen chemistry through careful study of the oxygen K (O-K) EELS edge, in combination with other EELS features of interest from $Li_{2-x}IrO_3$ such as the Li-K edge and the Ir N and O edges as listed in Table 3.1. Figure 3.5 shows

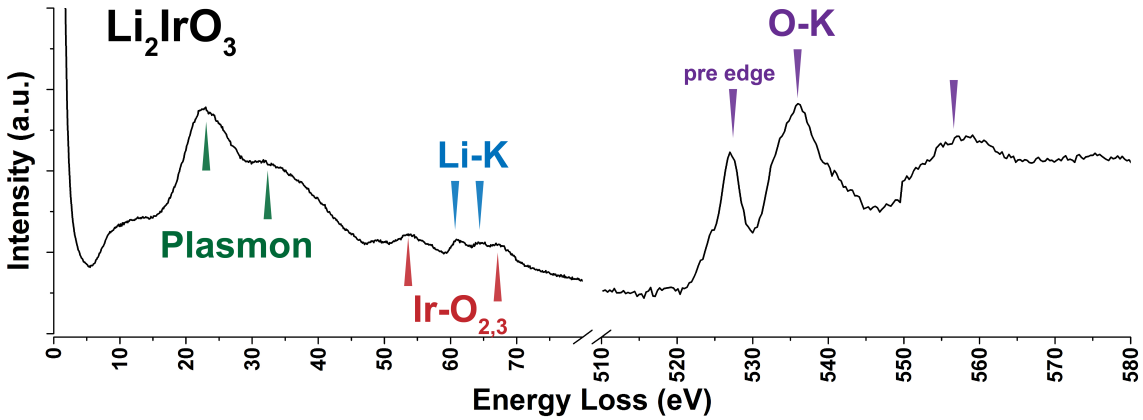

Figure 3.5. EELS Spectrum of Li_2IrO_3. Colored markers indicate the peak position of each elemental edge and feature of interest in the spectrum.

low-loss and core-loss EELS for pristine Li_2IrO_3 which had not been previously reported in the literature.

Element	EELS Feature	Energy Loss (eV)
Iridium	O_3 edge	54
	O_2 edge	67
Lithium	K edge	60
Oxygen	pre edge	528
	K edge	532

Table 3.1. EELS Features for the $Li_{2-x}IrO_3$ System

The Li-K edge can be used to determine the degree of lithiation in the sample. Typically, this feature is listed in the literature at a 55 eV energy loss. In this case, the Li-K edge has a delayed onset at approximately 60 eV, which is common. This edge is sandwiched between the iridium $O_{2,3}$ edges, and careful consideration of the lithium EELS must be taken due to the partial spectral overlap.

The major O-K edge, which corresponds to electron transitions from O 1s to high-level Ir s and p mixed with O 2p states, has an onset in intensity at 533 eV and reaches a maximum at about 538 eV. The O-K edge also has a pre-edge feature in the region from 525 eV to 531 eV, which is commonly known as the 'hole peak'. This feature corresponds to transitions from O 1s to O 2p states that are hybridized with the Ir d states, and is a potential identifier for changes in the oxygen redox state.[124–126]

EELS spectra were collected from the particles cycled to positions II, III, and IV on the voltage profile. The low-loss EELS signature of $Li_{2-x}IrO_3$ showed some changes during the delithiation process, as shown in Figure 3.6. Namely, the Li-K edge at 60 eV dramatically decreases in intensity as delithiation occurs. Closer examination also shows the presence of the iridium N_7 and N_6 edges at 63 eV and 68 eV, respectively. The change in intensity in these edges across the $Li_{2-x}IrO_3$ composition is largely due to the changing Li-K edge intensity which adds to the background signal. Moreover, the iridium O and N edges represent higher-order electronic transitions that are not well understood or interpretable.

Meanwhile, the change in the O-K edge is much more interesting as $Li_{2-x}IrO_3$ goes through different states of delithiation. This evolution in fine structure is shown in Figure 3.7A. There is not much change in the primary oxygen-K edge feature, however there is a significant change in the pre-edge feature between 523 and 531 eV, which is outlined in gray. As Li_2IrO_3 becomes increasingly delithiated, there is an observed peak splitting in the pre-edge feature, eventually becoming two separate peaks labelled α and β. The peak splitting is first observed in $LiIrO_3$ as a strong shoulder centered about 525 eV, and is a fully formed second α peak when 1.5 lithium formula units have been removed. The

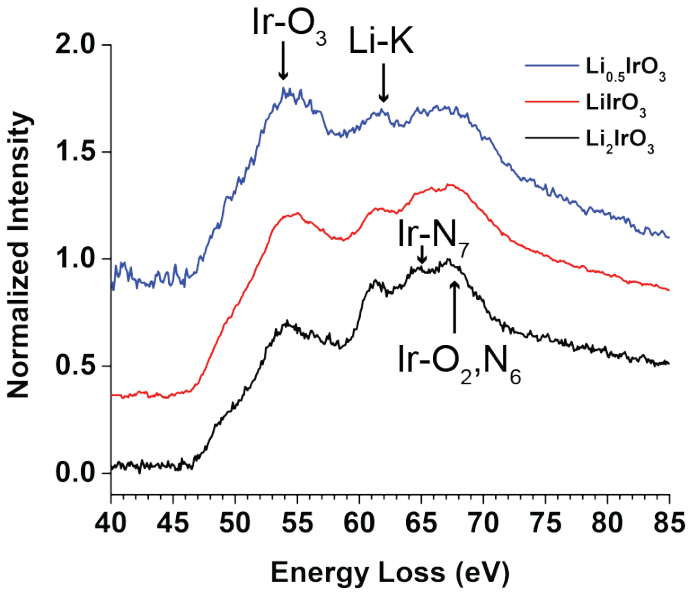

Figure 3.6. Low-Loss EELS Spectra of $Li_{2-x}IrO_3$ Samples Cycled to Different States of Charge

intensity of the pre-edge feature in the 525 eV - 531 eV energy window was integrated for Li_2IrO_3, $LiIrO_3$, and $Li_{0.5}IrO_3$ and the intensities relative to the Li_2IrO_3 intensity were plotted in Figure 3.7B. The presence of a α and β peak in $Li_{0.5}IrO_3$ resulted in a 30% increase in the intensity of this pre edge feature compared to the pristine Li_2IrO_3. This observation strongly suggests that there is a change in the oxygen electronic structure, more specifically an increase in the density of unoccupied states, as a result to the electrochemical cycling.[113]

XANES is an excellent complementary technique to EELS as both techniques probe the energy needed to promote electrons from a core state to an empty state.[127,92] XANES also has a higher achievable energy resolution than the 1 eV of STEM EELS. However, both spectroscopic techniques are useful as XANES provides bulk-level spatial resolution while EELS has achievable spatial resolutions of < 1 nm. As such, additional XANES

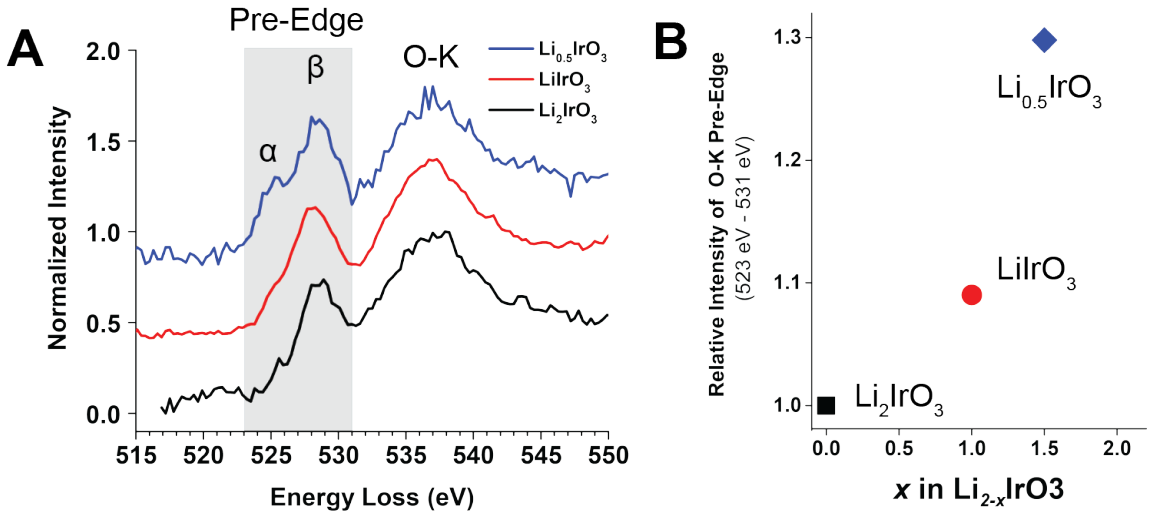

Figure 3.7. Analysis of O-K Edge EELS. (A) O-K edge for Li_2IrO_3, $LiIrO_3$, and $Li_{0.5}IrO_3$. The pre-edge peak region has been highlighted in grey, with the α and β peaks labelled. (B) Integrated intensity of the pre-edge region for Li_2IrO_3, $LiIrO_3$, and $Li_{0.5}IrO_3$.

analysis was carried out on the $Li_{2-x}IrO_3$ samples to confirm the EELS results and better understand the changes to oxygen and iridium during electrochemical cycling. The improved energy resolution would more clearly resolve the peak splitting in the O-K edge observed in Figure 3.7. Furthermore, XANES has the capability of probing the Ir M edge to understand changes to the iridium oxidation state that cannot be probed with EELS as the feature has an extremely high energy loss value with very poor signal.

Figure 3.8A shows the XANES analysis of the Ir M_3 edge at different states of charge, again marked with Roman numerals corresponding to the voltage profile in Figure 3.2. The Ir M_3 edge centroid shows a distinct blue shift from 2561.0 eV to 2561.9 eV as the degree of delithiation increases from Li_2IrO_3 to $LiIrO_3$, as plotted in Figure 3.8B. This blue shift indicates oxidation of Ir to compensate charge during lithiation, as may be expected. However, further delithiation to $Li_{0.5}IrO_3$ shows a slight red shift in the M_3

edge suggesting a decrease in the Ir oxidation state. Lithiation of the $Li_{2-x}IrO_3$ upon discharge shows hysteresis in the evolution of the Ir M_3 centroid, with a slightly lower energy position upon complete lithiation to Li_2IrO_3. The hysteretic nature in the Ir M_3 evolution suggests that Ir oxidation occurs from positions I to III, followed by a different charge compensation mechanism, possibly related to oxygen activity.

x

As previously discussed, the pre edge peak corresponds to electronic transitions between the O $2p$ orbitals and Ir d orbitals. The Ir d orbitals are split into both t_{2g} and e_g states, which result in the split α and β peaks, respectively. The increased intensity in the α peak with decreasing lithium content is typically related to the loss in Ir d electrons. Close meaurement of the α and β peak positions also shows an increase in the peak splitting from a 2.8 eV split at Li_2IrO_3, which matches previous literature reports, to a 3.6 eV split at $LiIrO_3$.[128,129] This increased peak splitting provides further evidence for the loss of Ir d electrons.[130,131] Further delithiation to $Li_{0.5}IrO_3$ results in almost no change in the peak splitting energy.

The combination of Ir M_3 edge shifting to higher energies and the observed peak splitting in the α and β peaks of the O-K edge in the delithiation process to $LiIrO_3$ suggests changes in the electronic states of both Ir and O, as opposed to just pure Ir oxidation from Ir^{4+} to Ir^{5+}. As Li_2IrO_3 is a Mott insulator, lithium removal causes electrons in oxygen $2p$ states to transfer to unoccupied Ir d states, increasing orbital mixing and resulting in additional holes in the oxygen orbitals.[129,132,133] This enhanced mixing explains the fine structure evolution in the O-K edge XANES and EELS during delithiation from Li_2IrO_3

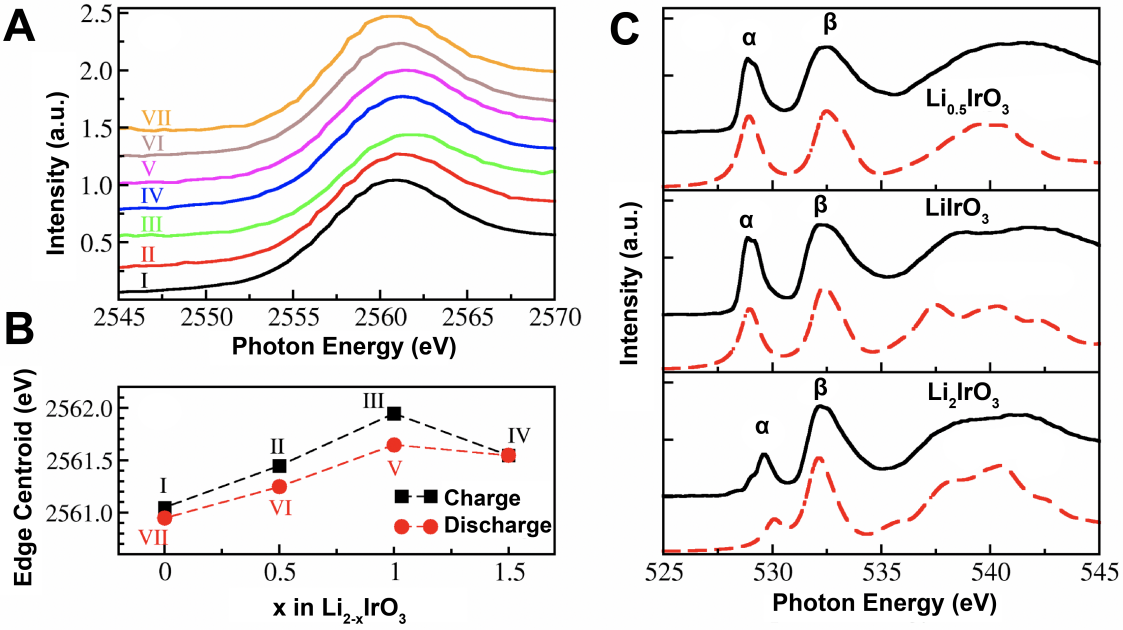

Figure 3.8. XANES Spectra Collected at Different Stages of Charge. (A) Experimental Ir M_3-edge XANES spectra. (B) Evolution of centroid energies of Ir M_3-edge at different states of charge. (C) Experimental bulk (total fluorescence yield) (solid black) and calculated (dashed red) O K-edge spectra. The simulated spectra are offset horizontally to align with experimental spectra, and offset vertically for presentation. The roman numerals in A,B correspond to the states of charge labelled in Figure 3.2.

to $LiIrO_3$. However, this charge redistribution does not correspond to additional charge compensation and charge capacity.

Additional DFT calculations of the electronic structure of iridium and oxygen help confirm the observed behavior. The calculated density of states for oxygen $2p$ states (red line) and iridium d states (black line) are shown in Figure 3.9A. Lithium removal from $Li_{2-x}IrO_3$ results in an increasing contribution of O $2p$ orbitals to the density of states immediately below the Fermi level (black dashed line). In fact, the heavily delithiated $Li_{0.5}IrO_3$ shows a larger contribution from the O $2p$ orbitals than the Ir d orbitals.

Bader charge analysis via DFT also provides information regarding changes to the iridium and oxygen oxidation states during delithiation. Figure 3.9B shows the Bader charges of Ir and O for $Li_{2-x}IrO_3$. During delithiation the Ir Bader charge shows an inflection point at 1 Li formula unit removed, demarcating two clear regions with differing slopes at higher and lower degrees of delithiation. Bader charge analysis indicates a Ir^{4+} oxidation state for pristine Li_2IrO_3, which increases during delithiation until reaching $LiIrO_3$, after which a slower rate of change is observed and there is a minimal change from $LiIrO_3$ to $Li_{0.5}IrO_3$. This indicates two different rates of oxidation in Ir before and after reaching the $LiIrO_3$ state. In contrast, the oxidation rate of oxygen becomes steeper after removal of one Li formula unit indicating increased contribution of O at deeper states of charge. Comparison to a structure with 1% oxygen loss, marked by green crosses, shows that there is a change to the Bader charge of Ir but not O, suggesting delithiation past $LiIrO_3$, into the second voltage plateau, results in oxidation of O and not Ir.

Knowing that O oxidation and partial oxidation loss might be expected based on the XANES and DFT analysis, we can use EELS to examine nanoscale spatial variation in the O-K fine structure signature. Figure 3.10A shows the EELS O-K edge evolution for $LiIrO_3$, collected as a linescan from the surface of the particle towards the bulk region. Observing both the primary O-K edge feature and the pre edge peak shows very weak intensity at the near-surface level, suggesting little oxygen presence in the first $\sim$ 20 nm. Strong signal in the O-K edge is seen afterwards, and variations of the fine structure related to the α (marked with black arrow) and β peaks are clear. This variation in EELS signature suggests the presence of minimal oxygen loss even during the delithation

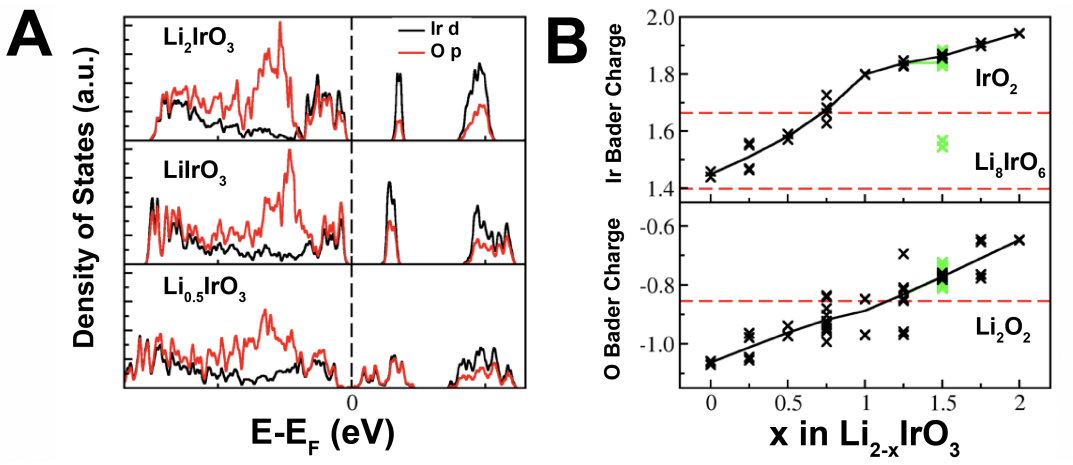

Figure 3.9. DFT Analysis of Oxygen Electrochemical Behavior. (A) DOS of $Li_{2-x}IrO_3$ (x=0, 0.5, 1 and 1.5), calculated from DFT with the HSE functional and including SOC. Black and red lines represent the DOS of Ir *d* and O *p* states, respectively. The Fermi level is set to zero and indicated by the vertical dashed line. (B) Bader charges of Ir and O in $Li_{2-x}IrO_3$, which are computed as the difference between the valence electron numbers of neutral atoms (9 and 6 for Ir and O, respectively) and Bader population. Different points correspond to different Ir and O atoms in each structure. The green crosses indicate the Bader charges of Ir and O in 1% oxygen deficient $Li_{0.5}IrO_3$. The lines are constructed by connecting the average Bader charges at each x. The red dashed lines indicate the Bader charges of Ir in IrO_2 and Li_8IrO_6, and of O in Li_2O_2, respectively.

process, and variations in the mixing of the oxygen and iridium orbitals shown via DFT and XANES.

Interestingly, examination of the oxygen fine structure of Li_2IrO_3 after a full lithiation and delithiation cycle, i.e. position VII in Figure 3.2, shows different O-K edge fine structure compared to the pristine Li_2IrO_3 O-K edge. Most notably, there is a strong α peak splitting that is observed throughout the linescan that is not present in the pristine Li_2IrO_3 spectrum. This suggests either some irreversibility in the orbital mixing between O 2*p* and Ir *d* states during the delithiation process, or an incomplete lithiation of the

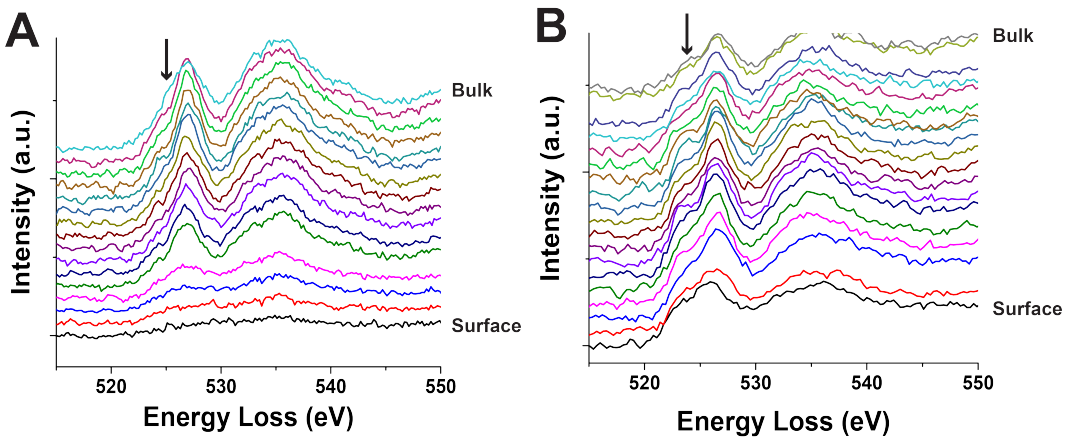

Figure 3.10. Spatial Variation of Oxygen EELS Signature. (A) O-K EELS linescan for $LiIrO_3$. (B) O-K EELS linescan for cycled Li_2IrO_3. Arrows in A,B mark the pre-edge peak splitting in the fine structure. The linescans extended from the particle surface into the bulk of the particle with 5 nm step sizes between each linescan.

particular particle analyzed. A comparison of the near-surface spectra of Li_2IrO_3 to $LiIrO_3$ shows a stronger O-K edge signature in the relithiated structure. As such, any oxygen loss that occurs during delithiation may be partially reversible, given the differences in EELS signature. However, even in Li_2IrO_3 there is still less oxygen signal at the surface, indicating only partial restoration of oxygen lost during delithiation. This is consistent with the behavior of Li-rich materials after cycling in general, and one of the primary challenges in utilizing oxygen in the charge compensation mechanism.

3.5. Summary and Outlook

Here, the chemical and structural behavior of $Li_{2-x}IrO_3$ was studied at different states of charge. As expected, $Li_{2-x}IrO_3$ has good structural stability during cycling, and no significant changes in morphology were observed by TEM. There were, however, notable changes to the oxygen chemistry during cycling. Careful analysis of the O-K edge of

$Li_{2-x}IrO_3$ through EELS, XANES, and DFT was able to reveal changing electronic structure as the degree of delithiation increased in the system. Although DFT suggests that oxygen $2p$ orbitals have increased contribution to the density of states near the Fermi level after just removal of 1 Li, oxygen oxidation does not occur until further delithiation to $Li_{0.5}IrO_3$. As such, the key takeaway is that changing electronic structure in oxygen, which can be detected experimentally through spectroscopy, does not immediately translate to oxygen activity and additional charge capacity.

Several questions related to oxygen oxidation and electrochemical activity still remain after this study. Changes to the oxygen electronic state were detected on the bulk level, but it is not known how much oxygen within a unit cell participates in charge compensation during cycling, and if specific oxygen atoms at different crystallographic sites have more or less activity and stability during cycling. This problem is also related to the issue of oxygen loss during cycling. That is, any oxygen loss that occurs in the structure leads to rapid performance degradation if the process is not reversible. Further experiments are needed to determine if oxygen oxidation is always commensurate with irreversible oxygen loss, and if its possible to decouple the two phenomena. It would also be beneficial to determine if it is possible to tune the potential at which oxygen oxidation contributes to charge capacity, as > 4 V cycling typically lies outside the electrochemical stability window of many liquid electrolytes used.

This work, of course, only focused on the model $Li_{2-x}IrO_3$ system, and not a more practical system like $Li_{2-x}MnO_3$ which does not feature a prohibitively expensive metal. However $Li_{2-x}MnO_3$ experiences sliding and other structural transformations which may affect the degree of oxygen activity and charge compensation during delithiation since the

oxygen stacking changes. More broadly, the fact that the presence of lithium inside the oxide layers changes the oxygen bonding begs the question of what other unexplored elemental dopants or alloying can be introduced to the structure to enhance charge capacity or improve cycling stability.

CHAPTER 4

Valence EELS: A Complementary Method to Conventional EELS Characterization of Lithium Ion Battery Materials

4.1. Chapter Overview

Previous chapters focused on revealing reaction mechanisms and the effects of crystal and electrode structure on chemical reactivity and distribution. Imperative to these studies was the ability to use EELS and other spectroscopic techniques for chemical analysis of key lithium ion battery elements. TEM, STEM, and EELS in particular have the huge advantage of sub-nanometer spatial resolution to provide local information on the nanoscale electrochemical processes at play. However, several factors frequently complicate proper EELS analysis of key lithium ion battery elements – sample thickness, unwanted sample-beam interactions and consequent beam damage, and spectral overlap of important EELS edges. Whether or not these issues can be avoided often changes on a case-by-case basis. Moving away from many of the model systems described so far and extending analyses to more complex, real-world materials samples will require improved techniques and methods for structure and composition characterization.

The work in this chapter describes a complementary EELS method to more routine EELS analysis. Focusing on the valence EELS region (see Section 1.6.5) of battery materials provides additional information that is useful in the cases when there is strong overlap of spectral features, poor signal-to-background ratios, or thicker and uneven sample areas.

For example, this work shows that the valence EELS features in maintain higher signal-to-background ratios than the Li-K edge, most notably when spectra are collected with minimal acquisition times or from thick sample regions. EELS maps of these valence features give comparable results to the Li-K edge EELS maps, and more accurately highlight morphology and composition distributions after only minimal spectral processing.

Moreover, utilizing the valence EELS region can enable low electron-dose composition studies of beam sensitive materials, and possibly enable higher temporal resolution studies of dynamic electrochemical properties.

The work described here is reproduced and adapted from Reference [134], with permission from Cambridge University Press.

4.2. Introduction

Rechargeable lithium ion batteries have enabled the portable electronics revolution of the last decade, but now bottleneck progress in advanced technologies like electric vehicles.[57,135] Achieving significant improvement in energy capacity or battery lifetimes requires new designs for both electrode and electrolyte materials. However, characterizing these new state-of-the-art lithium ion battery materials demands the ability to discern subtle atomic- and nano-scale changes in elemental composition, crystal lattice site occupancy, oxidation state, and bonding coordination.[136,137,39] As discussed throughout this dissertation, TEM and STEM provide an indispensable set of characterization techniques at these desired length scales. When it comes to studying lithium ion batteries, TEM and STEM can both routinely image important transition metal elements, but it is very challenging to image light elements important to lithium ion batteries like lithium and

oxygen. EELS, however, can analyze all of these key elements due to the high amount of core-loss excitations that can be detected by the EELS spectrometer.[74] The STEM EELS approach in particular combines very high spatial resolution with powerful chemical analysis methods.

Conventional EELS Analysis of LIBs. EELS functions by measuring the energy lost by an electron from the STEM electron beam after an inelastic scattering event with an atom in the sample (see Figure 1.6). Each element exhibits a characteristic EELS edge, and an element can have multiple EELS edges based on its electronic structure and the scattering event that occurs. The fine structure of these edges changes based on composition, electronic structure of the elements, and local coordination interactions with other elements. Moreover, the fine structure can be interpreted to gather critical information about elemental composition, bonding, and oxidation state. Often, EELS spectra from unknown samples are compared to reference spectra, and materials can be 'fingerprinted' based on this analysis of the line shape and edge-onset positions.[138–140] Figure 4.1 highlights the diverse EELS fine structure of several lithium cathode materials: layered $LiCoO_2$ and the $LiCo_{0.9}Ni_{0.1}O_2$ alloy, layered Li_2MnO_3 and spinel $LiMn_2O_4$, and orthorhombic $LiFePO_4$.

EELS edges from relatively low-energy scattering events, i.e. low-loss features, are shown in Figure 4.1A. The Li-K edge seen here is the only lithium EELS signature, which has an edge fine structure that is strongly dependent on Li coordination, and can vary in both onset energy (between 55 and 60 eV) and feature width.[75,77,102] The transition metal-M edges are also found in the low-loss region, which can provide some limited

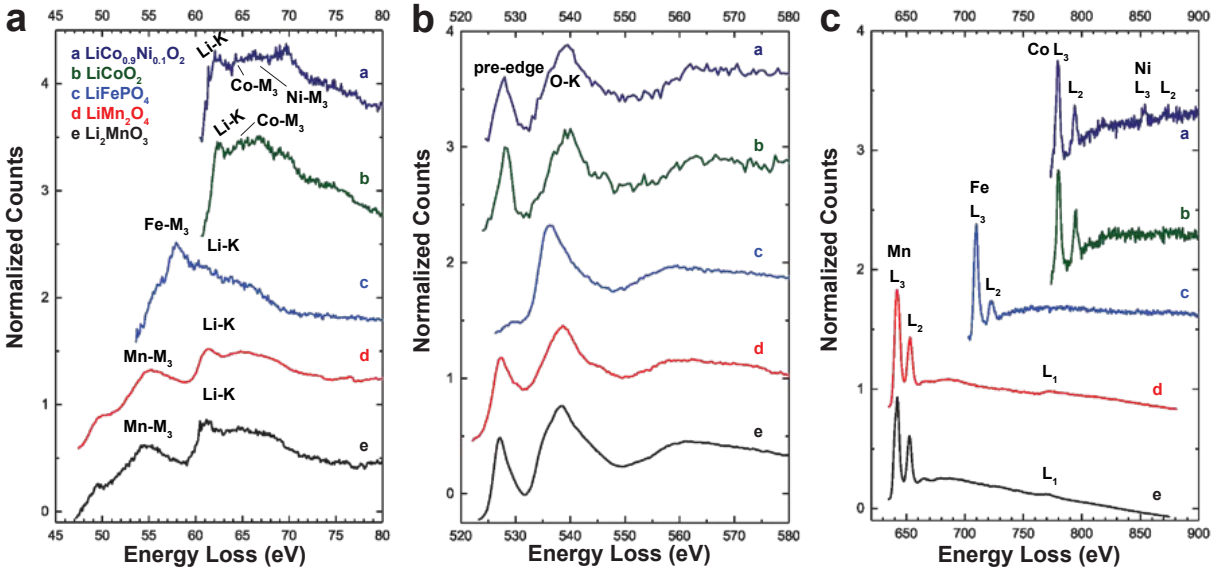

Figure 4.1. Characteristic EELS spectra of several cathode materials. (A) Low energy loss region that includes the Li-K edge and transition metal-M edges. Detailed labelling of the different low-loss features can be found in Table 4.1. (B) The O-K core-loss edges for each material. (C) The transition metal-$L_{3,2}$ edges. All spectra in (a,b,c) have been normalized with respect to the signal maximum and offset vertically for clarity.

information about the presence of the elements. The onset energies for both kinds of low-loss features in Figure 1a are listed in Table 4.1. Higher energy-loss features, i.e. core-loss features, such as the O-K and transition metal-L edges are seen in Figure 4.1B and 4.1C. These core-loss features are usually necessary for quantitative composition analysis and also reveal atomic coordination and cation valence state.[125,124,141,142,79] Chapters 2 and 3 featured careful analysis to this effect.

Although LIB materials have several noteworthy EELS edges that can be examined, acquisition and interpretation of the data is often challenging. Significant spectral overlap is possible for both low-loss and core-loss features, complicating any 'fingerprint' analysis, especially with materials containing lithium and transition metals. One prominent

Material	EELS Edge	Energy Loss (eV)
$LiCo_{0.9}Ni_{0.1}O_2$	Li-K	62.1
	Co-M_3	64.3
	Ni-M_3	67.8
$LiCoO_2$	Co-M_3	64.4
	Li-K	62.3
$LiFePO_4$	Fe-M_3	57.9
	Li-K	60.3
$LiMn_2O_4$	Mn-M_3	55.2
	Li-K	61.3
Li_2MnO_3	Mn-M_3	54.9
	Li-K	61.3

Table 4.1. Low-loss EELS edges of several cathode materials.

example in the field of lithium ion batteries is the complete overlap between the iron and lithium signal in $LiFePO_4$.[143]

Additional challenges come with collecting sufficient signal for proper analysis. EELS edges at higher energy-loss regions of the spectrum have much weaker signal since the scattering events they represent happen less frequently. This makes core-loss edges difficult to detect without long acquisition times, which causes more beam damage to the sample. Moreover, EELS is very sensitive to sample thickness, and analysis areas thicker than 100 nm can lead to strongly reduced signal for all EELS edges shown in Figure 4.1.

Valence EELS as a Complementary Approach. Outside of the primary core-excitation EELS edges shown in Figure 4.1, it is possible to garner information from a material in the valence EELS region between 5 eV and 30 eV. This region contains interband transition features ($<$ x10 eV) and plasmon features ($\sim$ 20 eV) that give insight to the complete compound and subcomponents as opposed to individual elements. These valence EELS features are commonly examined when studying electronic structure and properties of

semiconductors, but not usually considered for analysis of lithium ion battery materials.[144–146] However, valence EELS features were recently used to successfully discern between lithiated and delithiated states of $LiFePO_4$ and to map individual components of the solid electrolyte interface formed on a silicon anode.[147,148]

The wider use of valence EELS features in other fields, along with recent studies on lithium ion battery materials, prompted the question of how useful valence EELS analysis could be for studying lithium ion battery materials. Here, the valence EELS features of various lithium ion battery materials are explored, along with exploring the utility of analyzing these features alongside the core-loss EELS edges. These valence EELS features provide a robust complement to characteristic low energy core-loss EELS edges features like the Li-K edge, especially when there is a relatively low signal-to-background ratio in the spectra due to low electron beam dosages or very thick sample regions. In particular, we describe the EELS fine structure found in the interband transition region (2 - 10 eV), which can be used as a proxy for core-excitation features in a 'fingerprint' analysis. Furthermore, EELS mapping of these valence EELS features provide improved mapping results compared to the elemental EELS edges, especially in thick samples. As a result, this methodology can be useful in a wide range of experiments: from low-dose EELS of beam-sensitive LIB materials to in-situ analyses of samples with added "effective" thickness due to the encapsulating membrane thickness or liquid in the experimental set-up.[149]

4.3. Materials and Methods

4.3.1. Sample Preparation

The cathode samples discussed in this section ($LiFePO_4$, Li_2MnO_3, $LiCoO_2$, and $LiCo_{0.9}Ni_{0.1}O_2$) were prepared through solid state synthesis methods described in the literature.[150,151,39] Samples of γ-Fe_2O_3 and NiO were purchased commercially through Sigma Aldrich. All powders had average particle sizes of a few micrometers unless otherwise noted, as confirmed via prior TEM analysis. TEM samples were prepared by directly dispersing the powders onto copper-mesh lacey carbon TEM grids inside of a Ar glove box, without additional grinding or dispersion in a solvent.

4.3.2. TEM and EELS Analysis

TEM Settings. STEM imaging and EELS data was collected on a Hitachi HD2300 STEM with a 200 kV accelerating voltage.[152] The condenser lens apertures used during data collection provided a convergence angle range of 8 - 12 mrad.

EELS Acquisition Settings. EELS spectra were collected with a Gatan Enfina EELS spectrometer. A 2 mm entrance aperture was used for EELS collection, resulting in a 14 mrad collection angle. Typical energy resolution values of the EELS spectra, judged by the full-width at half-maximum value of the zero-loss peak(ZLP), were 0.8 eV $\pm$ 0.1 eV. The spectra were collected using a 0.1 eV dispersion.

Acquisition time was kept to a minimum to avoid beam damage, and to test the limitations of signal-to-background ratios on the interpretability of the EELS edges. Electron doses were calculated as outlined as such:[153]

$$dose(e^-/nm^2) = \frac{beam\ current(A) * acquisition\ time(s)}{electron\ charge(C/e^-) * pixel\ area(nm^2)}. \tag{4.1}$$

The calibrated beam current for the Hitachi HD2300 settings used during EELS acquisition was kept at 0.073 nA. The calculated dosages for EELS linescans are included in the Results and Discussion section.

4.3.3. Data Processing

Typical EELS data processing involves calibrating the spectrum using the zero loss peak, deconvolution of the spectra to remove plural scattering effects, and background subtraction of the region of interest to isolate the important EELS edges. This process is shown in Figure 4.2. The standard Fourier-log deconvolution routine from Gatan Digital Micrograph was used to deconvolute the low-loss EELS data shown in Figures 4.3, 4.5, and 4.6. Fourier-ratio deconvolution was used for core-loss features such as the O-K and transition metal-L edges.

A simple reflected-tail model was used in the deconvolution routine to remove the ZLP. Other methods ZLP removal, such as fitting a pre-measured ZLP, yielded similar results. Any drift in the ZLP across the spectrum image maps was corrected using the energy drift correction tool from the SITools package by D.R.G. Mitchell.[154]

A low-loss spectrum containing the ZLP was always collected from a neighboring region with similar thickness when deconvoluting core-loss spectra. A power-law background model was always utilized (red line in Figure 4.2) to extract the EELS signal of interest.

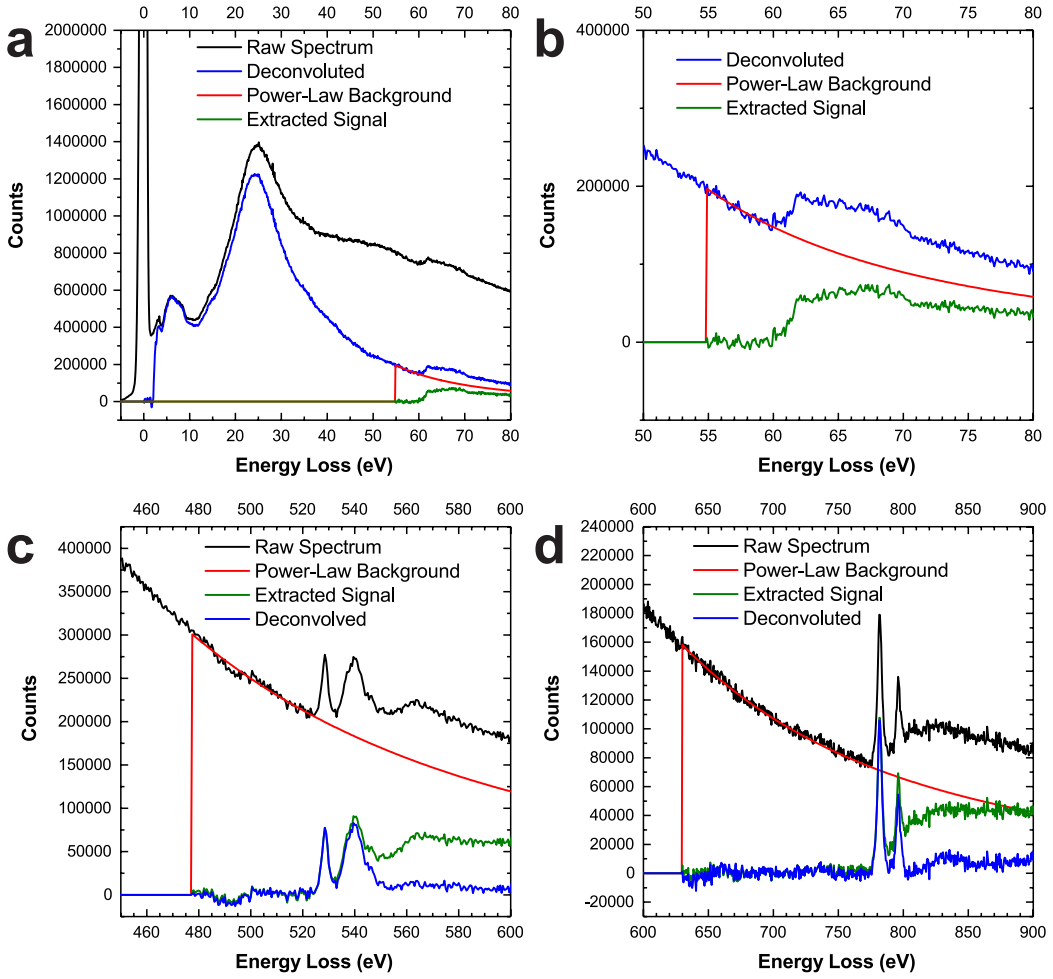

Figure 4.2. Example background subtraction and deconvolution routine for $LiCoO_2$. (A) Data processing routine for $LiCoO_2$ low-loss EELS spectrum, involving Fourier-log deconvolution of the spectrum followed by background subtraction from the Li-K and Co-M edges with a power-law model. (B) Magnified view of Li-K and Co-M edge processing from (A) to highlight the residual signal after background subtraction. (C) Data processing routine for $LiCoO_2$ O-K EELS edge, involving background subtraction using a power-law model. This was followed by Fourier-ratio deconvolution to remove plural scattering effects. (D) Data processing for the $LiCoO_2$ Co-$L_{3,2}$ EELS edge, which used the same method as in (C).

The second derivative calculations, as shown in Figure 4.8, were done using the second derivative numerical filter found in Digital Micrograph.

4.4. Results and Discussion

4.4.1. Valence EELS Features of Lithium Ion Battery Materials

Removal of the ZLP, along with Fourier-log deconvolution, is necessary for careful investigation into the valence EELS region. This spectral processing reveals the EELS fine structure after the trailing edge of the ZLP, which begins approximately at 2 eV. Figure 4.3 shows the valence EELS region of the LIB materials highlighted in Figure 4.1. Delithiated $FePO_4$, γ-Fe_2O_3, and NiO are also included for comparison to the lithiated compounds, but are also of interest as conversion-type anode materials as discussed in Chapter 2.[155,97] The 5 - 10 eV region in each case shows the interband transition features for each material. As noted, it is possible to distingiush between $LiFePO_4$/$FePO_4$ due to adistinct peak intensity difference in the valence EELS fine structure at 6 eV.[147] This 6 eV is an excellent alternative to the Li-K edge when it is inaccessible to due spectral overlap or poor signal. However, the remaining compounds in Figure 4.3 have strong interband transition features as well.

For example, $LiCoO_2$ has a strong 4 eV shoulder that lowers in intensity in $LiCo_{0.9}Ni_{0.1}O_2$. Li_2MnO_3 and $LiMn_2O_4$ have similar fine structure, however Li_2MnO_3 has a much stronger 8 eV peak. This valence EELS information can be important information used to identify a material's composition, especially when paired with analysis of other low-loss and core-loss EELS features. Nevertheless, applications of valence EELS analysis and examination of interband transitions in lithium ion battery materials are not

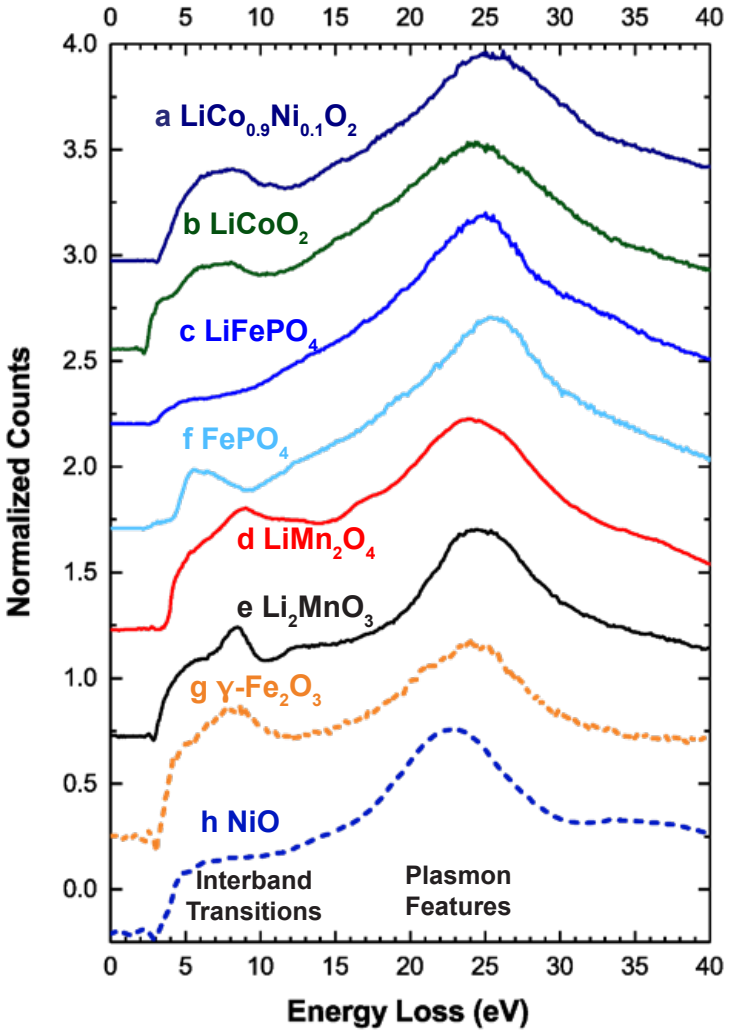

Figure 4.3. Valence EELS spectra of several LIB materials. Both the interband transition and plasmon regions can be seen. Dashed spectra are of reference transition metal oxides.

commonly found. Interpreting plasmon features is also viable, as differing compositions and size effects can cause changes to peak position energy and the plasmon peak width and fine structure.[156,157]

An important point to consider is the contribution of Cerenkov losses to the intensity and spectral features in the few-eV energy range. The effects of Cerenkov losses can

result in shifts in band-gap onset positions and dramatically alter the intensity of different valence EELS features.[158,159] The intensity of Cerenkov loss effects vary with the material being examined, but are most pronounced when high operating voltages are used and when spectra are collected from thick sample regions.[160] The EELS analysis here was carried out using an operating voltage of 200 kV, which is considered to be in the energy regime for Cerenkov losses. However, the spectra in Figure 4.3 were collected from thin sample regions with thicknesses < 0.5 inelastic mean free paths (λ), as estimated using the standard EELS log-ratio technique, and minimal effects due to Cerenkov losses are expected as a result.

4.4.2. Comparison of Valence and Low-loss EELS Features in Spectra with Low Signal-to-Background Ratio

Analyses of the interband transition features in LIB materials are an effective complement to analyzing core-excitation EELS edges, beyond cases like $LiFePO_4/FePO_4$ with a large peak intensity change at 6 eV. Interband transition features of LIB materials are, in general, unique enough for 'fingerprint' analysis when compared to a reference spectrum. Furthermore, these interband transitions are typically separated in energy-loss from other spectral features that often interfere with characteristic elemental edges. The bulk volume plasmon, which in thicker samples can overpower low-loss core-excitation features, is found at higher energy losses and does not interfere with the valence EELS region. The ZLP may interfere with some of the very low energy loss fine structure, but can be adequately removed in a variety of manners.[161] The zero-loss peak width is also less of an issue in TEMs and STEMs equipped with a cold-FEG source or a monochromator, as they can

have an energy spread of 0.1 eV or lower compared to the 0.8 eV spread on the microscope used in this work.

Figure 4.5 shows a series of low-loss EELS and valence EELS spectra to compare their signal-to-background ratio and accessibility. These features were collected from a sample of $LiCoO_2$, which is one of the prevalent intercalation cathode materials. Namely, the spectra were collected from sample regions with different thicknesses to examine the effect of thickness on the signal-to-background ratios of the two feature types. In addition, a minimal acquisition time of 1×10^{-6} seconds was used. These acquisition settings minimize the amount of damage to $LiCoO_2$ during collection and also test the interpretability limits of spectra with minimal signal.

Figure 4.4 shows BF and HAADF STEM images of the region from where the EELS data in Figure 4.5 was collected. The sample shown consists of 20 - 50 nm $LiCoO_2$ particles agglomerated into a region with increasing thickness. An EELS linescan, represented by the green arrow, was used to collect EELS data from a region of zero thickness (over the vacuum of space) through a very thick region. Spectra were collected from regions varying thicknesses measured by the number of inelastic mean free paths ($/lambda$), where $/lambda = 0.2$, 0.4, 0.6, 0.8, 1.0, 1.5, and 2.0. The linescan used a 1 nm^2 pixel size, resulting in a dose of 455 electrons/nm^2 based on the acquisition time and Equation 4.1.

The effect of sample thickness on the low-loss EELS signal is presented in Figure 4.5a. Here, the sample thickness of the different spectra ranges from 0.2 to 2 λ. The thicknesses were calculated from the EELS spectra using the standard log-ratio method. The Li-K and Co-M_3 edges from 60 - 70 eV become very hard to distinguish at thicknesses much higher than 1 λ due to the intense plasmon peak. The signal-to-background ratio of the

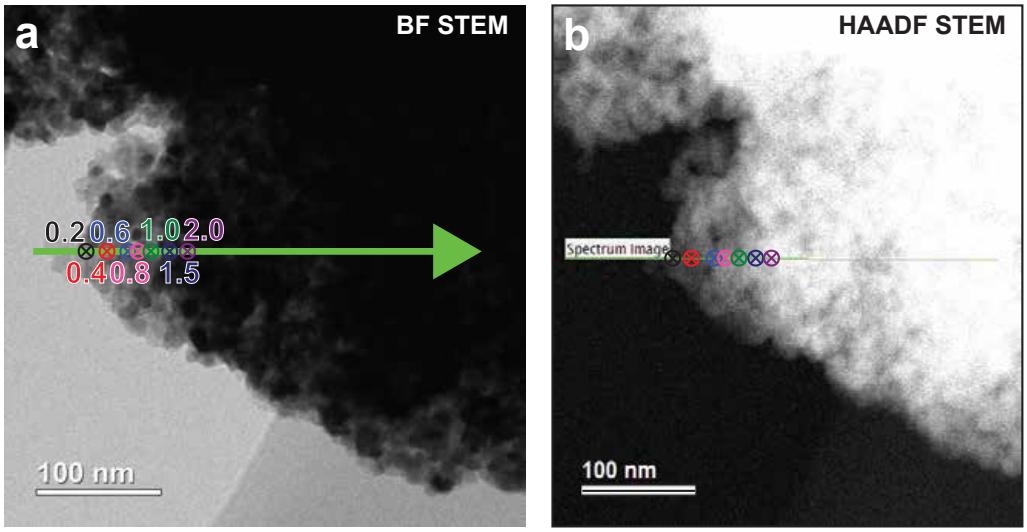

Figure 4.4. STEM images of $LiCoO_2$ and the EELS linescan region. (A) BF STEM image. (B) HAADF STEM survey image. The green line shows the range of the linescan with the arrow showing linescan direction. Markers along the linescan in (A,B) are positioned and colored to represent the location where each spectrum in Figure 4.5 was collected. The thickness of the sample (in λ) at each position is also labelled in (A).

Li-K edge was calculated to compare its intensity with varying thickness. Here, the signal-to-background ratio of the Li-K edge falls from ~2.45 with a thickness of 0.2 λ to a ratio of only ~2.05 when the thickness is 2 λ. These signal-to-background ratios would increase with longer acquisition times, but these results suggest a thickness of approximately 2 λ as the upper limit for any type of quantitative analysis of the Li-K edge features. In $LiCoO_2$, this upper thickness limit of 2 λ is approximately 250 nm, given an estimated $\lambda = 125$ nm.[162]

Standard Fourier-log deconvolution is typically used to remove plural scattering effects from low-loss EELS spectra, enabling improved analysis. Figure 4.5b compares EELS spectra collected from a thin (0.2 λ) and thick (1.0 λ) region of the sample, and shows

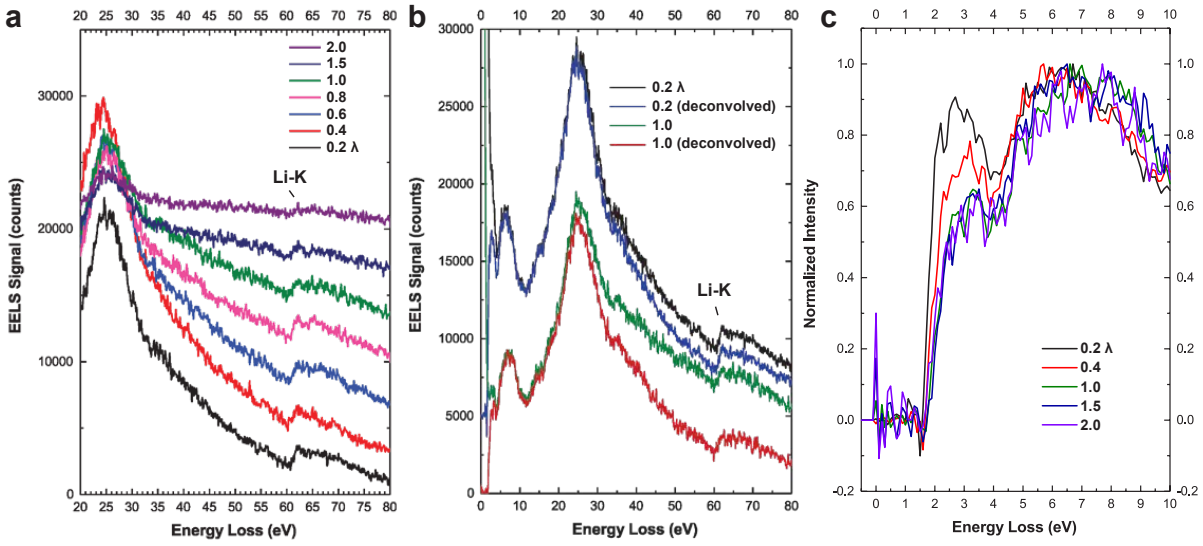

Figure 4.5. Effect of thickness on signal for low-loss and valence EELS regions. (A) Evolution of Li-K and Co-M low-loss signal with increasing thickness. (B) Low-loss EELS spectrum of a thin (0.2 λ) and thick (1.0 λ) sample area, with the Fourier-log deconvoluted spectra as comparison. (C) Deconvoluted EELS spectra of interband transition fine structure, collected from sample areas of differing thicknesses. All spectra were collected with a $1x10^{-6}$s acquisition time and a 0.1 eV/channel dispersion. Spectra in (A,B) are offset vertically to highlight the Li-K edge signal. Spectra in (C) were normalized with respect to the peak maximum at 6 eV.

the effects of Fourier-log deconvolution in both cases. Deconvolution of the thin spectrum does not show a significant effect. There is a slight decrease in the intensity of the trailing plasmon edge from 35 eV - 60 eV, and the signal-to-background ratio of the Li-K edge only slightly improves from ∼2.45 to ∼2.50. The thick spectrum, in contrast, shows a significant decrease in intensity of the plasmon edge in the same 35 eV - 60 eV region, with a curving slope in the trailing edge similar to the thin spectrum. The signal-to-background ratio also improves from ∼2.16 to ∼2.33.

Even though deconvolution of the thick sample somewhat improves the Li-K signal-to-background ratio, the fine structure of the Li-K and Co-M_3 edges is still not readily

interpretable. On the other hand, the interband transition region shown in Figure 4.5C does not degrade as significantly. The relative intensity of the 2.5 eV peak decreases with thickness compared to the wider 6 eV peak. However, both give good signal before and after spectral deconvolution. The 6 eV peak has a signal-to-background ratio of 2.81 even at sample thicknesses of 2 λ. Given that the interband transition features show improved signal over the Li-K edge in thick samples and at low signal and low dose conditions, they may be used as a proxy over other characteristic EELS edges to map the $LiCoO_2$ distribution in a sample.

Consideration of Cerenkov Radiation Effects when using Valence EELS. The features highlighted in Figure 4.5C are the most susceptible to Cerenkov loss effects, given that they are found in the < 10 eV region and were collected over a wide range of sample thicknesses. However, only minimal changes are observed in Figure 4.5C, with almost no change in the either the 2.5 eV peak or 6 eV peak as the thickness doubles from 1 λ to 2 λ. As a result, any Cerenkov losses present in this region appear to be minimal and do not affect the ability to use these valence EELS features for generating EELS maps, as discussed next.

4.4.3. Spectrum Imaging of $LiCoO_2$ with Valence EELS and the Li-K Edge

Standard EELS Spectrum Imaging. Figures 4.6 and 4.7 show an EELS spectrum image (SI) map of an $LiCoO_2$ sample and comparison of the mapping results of both the interband transition region and the Li-K and Co-M_3 edges. The SI maps used a 10 nm^2 pixel size and a $1x10^{-6}$ second acquisition, corresponding to dose of 45 electrons/nm^2. All SI maps were deconvoluted, and the pixel intensities were normalized to show a maximum

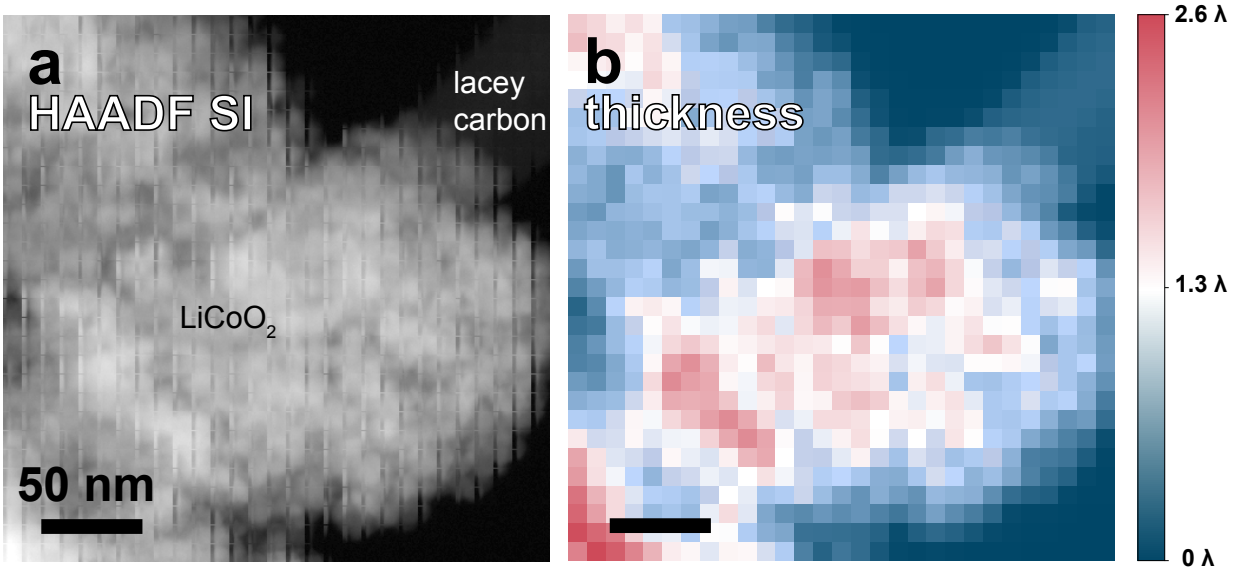

Figure 4.6. Characterization of $LiCoO_2$ region for SI Mapping. (A) EELS SI showing the morphology of $LiCoO_2$ agglomerated particle. (B) Thickness map of the sample, as determined by EELS. The color bar indicates the calculated sample thicknesses.The scale bar in both subfigures is 50 nm.

intensity as bright red and a minimum intensity as a deep blue. Figure 4.6a shows the HAADF STEM image collected from the SI mapping. The mapping region covers an area of $LiCoO_2$ with uneven thickness, which rests on the lacey carbon support grid. The thickness map in Figure 4.6B shows the range of thicknesses of the SI map area. Much of the $LiCoO_2$ in the map has thickness of less than 1 λ but does increase in thickness up to 2.6 λ.

The $LiCoO_2$ interband transition region (2 - 10 eV) is mapped in Figure 4.7A with the Li-K and Co-M_3 edge region (60 - 70 eV) mapped in Figure 4.7B. There is a significant 'edge effect' in the SI maps shown in both Figure 4.7A and B. The thin $LiCoO_2$ regions give the most EELS signal, which decays as the sample thickness increases. This results in an outline of the $LiCoO_2$ region rather than an accurate composition map, and could

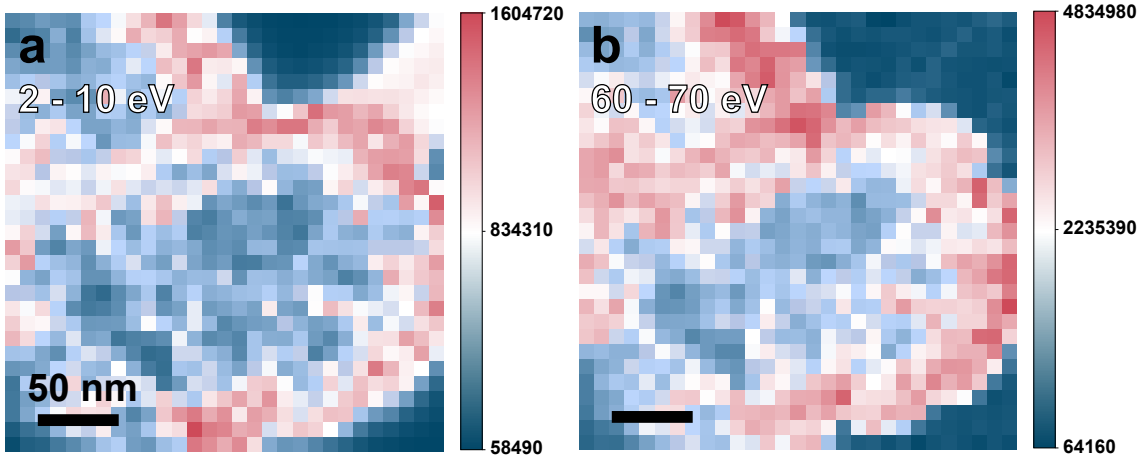

Figure 4.7. EELS mapping of Li-K and Valence EELS features in $LiCoO_2$. (A) Map of interband transition region of $LiCoO_2$ from 2 - 10 eV (B) Map of Li-K and Co-M edge signal, from 60 - 70 eV The color bar for (A,B) indicates the normalized intensities of the spectrum image. The scale bar in both subfigures is 50 nm.

be difficult to interpret in an unknown sample. However, both the interband transition region and the Li-K/Co-M_3 region produce relatively similar mapping results. Figure 4.7A also shows that the interband transition region captures some signal contribution from the lacey carbon support grid, which shows a bright feature in the top right corner of the map that is not seen in Figure 4.7B.

Second Derivative of the EELS Spectrum. Other EELS mapping reports have shown that calculating the 2^{nd} derivative of an EELS spectra can enhance separation of different spectral features to enable better EELS SI maps.[163] Taking the 2^{nd} derivative of the EELS spectra in each pixel of the SI map reveals the curvature of the fine structure, which is highly dependent on the different elemental components. Collecting low-loss EELS spectra from regions of pure lacey carbon and pure $LiCoO_2$, and subsequently taking the 2^{nd} derivative shows two spectra with peaks at different energy-loss

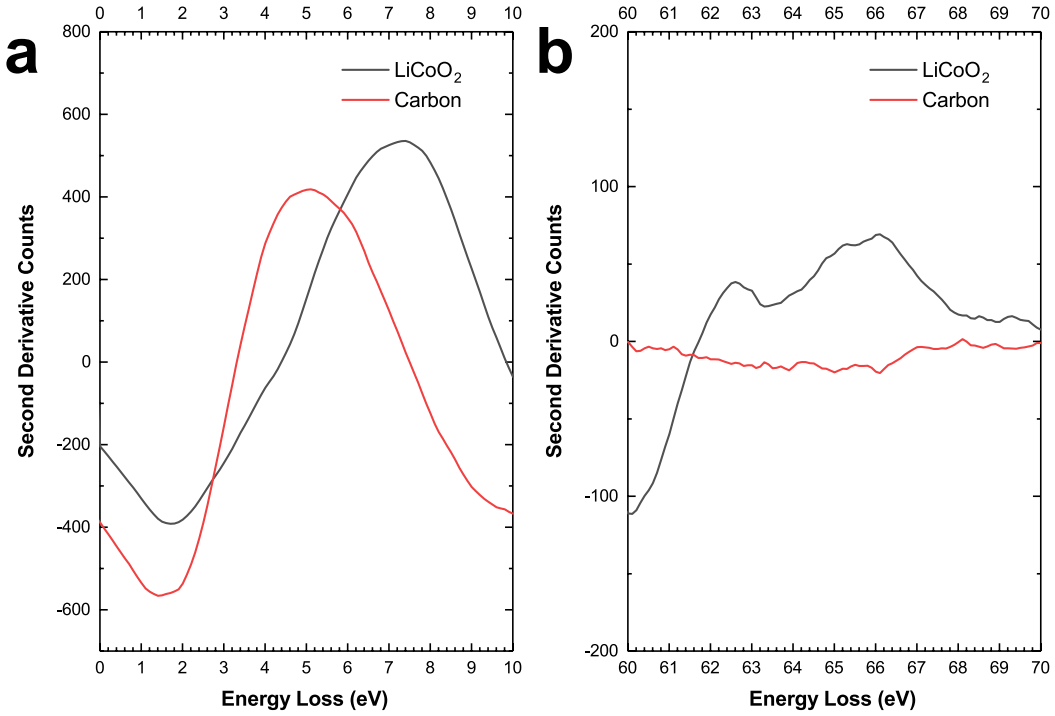

Figure 4.8. Second derivatives of EELS spectra collected from a region of $LiCoO_2$ and lacey carbon seen in Figure 4.7a. (A) Interband transition region (B) Low-loss region with Li-K and Co-M_3 edges.

values. These are shown in Figure 4.8. The lacey carbon regions of the SI map show a peak in second derivative centered about 5 eV, while the $LiCoO_2$ region shows a peak at 7 eV. The overlap between these two peaks from 4 - 7 eV explain why the 2 - 10 eV region plotted in Figure 4.7A highlight both $LiCoO_2$ and the lacey carbon. Furthermore, this result indicates that the 2^{nd} derivative processing should be able to separate the contributions of carbon and $LiCoO_2$ to the SI map shown in Figure 4.7A. Meanwhile, there is zero carbon signal after taking 2^{nd} derivative, as shown in Figure 4.8B, and no contribution to the SI map in Figure 4.7B.

Spectrum Imaging with the Second Derivative. Plotting the trailing edge of the 7 eV peak corresponding to $LiCoO_2$ produces the SI map in Figure 4.9A. In this case, the entire $LiCoO_2$ region is effectively mapped, even in the very thick areas of over 2 λ thickness. The 'edge effect' seen in Figure 4.7 is no longer present. Furthermore, there is a decrease in SI map intensity in the lacey carbon regions, caused by the exclusion of the carbon component. Overall, the SI map in Figure 4.9A more accurately depicts the morphology and composition of the $LiCoO_2$ region than mapping done using the Li-K edge. The same methodology was applied to the Li-K and Co-M_3 edges, and the resulting SI map is shown in Figure 4.9B. In this case, there is not a significant enhancement over the original SI map shown in Figure 4.7B. This SI map used a larger energy window than in Figure 4.9A, but isolating different regions of the second derivative spectrum with 1 eV windows also does not improve map quality. These results are demonstrated in Figure 4.10. Generating maps from 1 eV energy windows in the range from 60 - 70 eV shows maps with the same 'thickness effect' issue as the original map in Figure 4.7B, with some minor improvement in Figure 4.10C thanks to the intensity maximum in the 2^{nd} derivative as seen in Figure 4.8. The remaining maps have unimproved quality due to the worse signal-to-background ratio of the Li-K edge, even after deconvolution, resulting from a minimal exposure time and large sample thickness.

Ultimately, a high signal-to-background ratio is essential for deriving quantitative information from EELS spectra. Howefver, sample thickness and electron beam damage are often practical constraints to acquisition, which complicate the analysis of the Li-K edge and other core-loss excitations. As such, the valence EELS region may in these

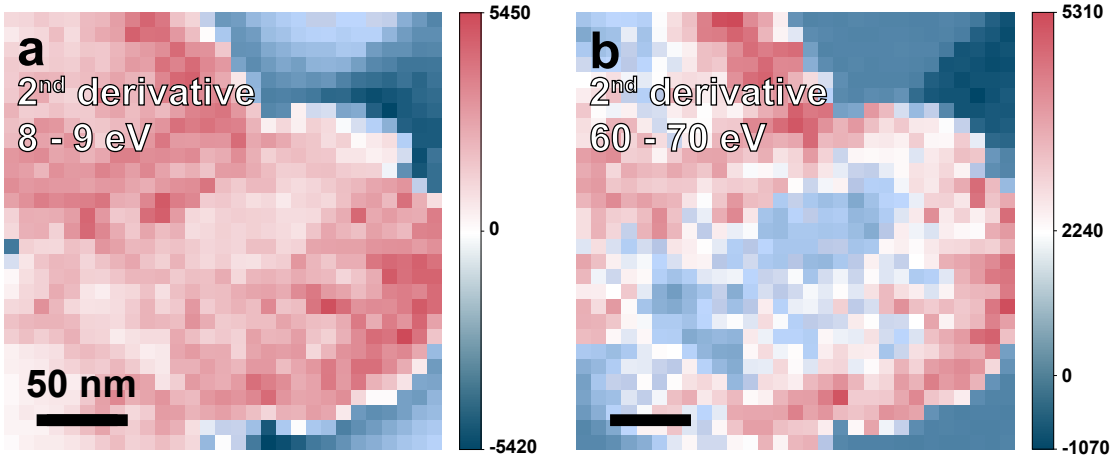

Figure 4.9. EELS mapping of Li-K and Valence EELS features in $LiCoO_2$ after 2^{nd} Derivative Processing. (A) Map of 2^{nd} derivative of valence EELS $LiCoO_2$ feature from 8 - 9 eV. (B) Map of 2^{nd} derivative of the Li-K and Co-M_3 edge signal, from 60 - 70 eV. Color bars to the right of the maps indicate the integrated intensity of the second derivative spectrum at each pixel. The scale bar in both subfigures is 50 nm.

cases provide important complementary information needed for characterization of a LIB material.

4.5. Summary and Outlook

The valence EELS region provides useful spectral features that are not often considered or taken advantage of when analyzing LIB materials. These features, though lacking in sharp edge structure, are unique enough to be used for 'fingerprint' analysis. This was seen to be the case for a variety of insertion cathode and conversion anode materials in Figure 4.3. Furthermore, the interband transition features have significant spectral intensity as they are found at very low energy-losses. The transitions demonstrate better signal-to-background ratios compared to characteristic edges found in the low-loss regime

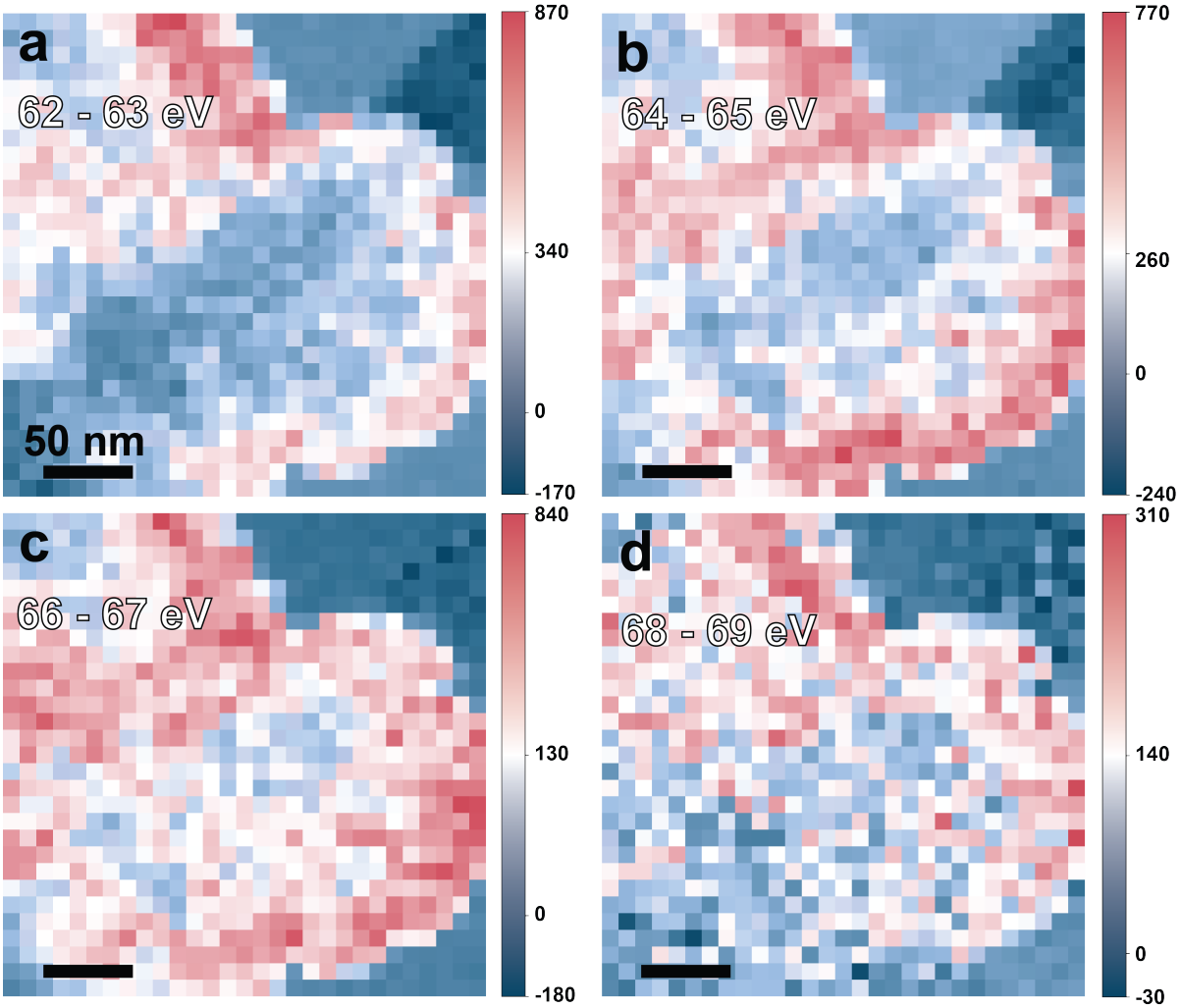

Figure 4.10. Spectrum imaging maps of the Li-K EELS edge, after taking the 2^{nd} derivative. The intensity of the 2^{nd} derivative spectra was integrated over (A) 62 - 63 eV, (B) 64 - 65 eV, (C) 66 - 67 eV, and (D) 68 - 69 eV to compare directly with Figure 4.9A. Color bars to the right of the maps indicate the integrated intensity of the second derivative spectrum at each pixel. The scale bar in all subfigures is 50 nm.

like the Li-K edge, and can act as alternative features of interest when important edges suffer from spectral overlap.

In $LiCoO_2$, the valence EELS features prove to be more robust than the Li-K and Co-M_3 edges before and after spectral deconvolution. This analysis was also done with a minimal acquisition time, further distinguishing the improvement of the valence EELS features over the Li-K edge. EELS SI imaging of the interband transitions gives similar mapping results as the Li-K and Co-M_3 edges. Taking the 2^{nd} derivative of the valence EELS spectra isolates the $LiCoO_2$ component to give more accurate mapping of the morphology and composition distribution, even when mapping very thick sample areas.

Applying valence EELS analysis to LIB materials beyond the $LiCoO_2$ system would provide several advantages. As it is possible to discern between spectral contributions from carbon and the material of interest, it may be possible to dig deeper into EELS studies on electrochemically-cycled materials that are intermixed with carbonaceous binders and conductive additives. Furthermore, experimental cases where signal is an issue would benefit from valence EELS analysis. Thicker samples on average can be examined through the EELS interband transitions, which may be useful for in-situ or in-operando analyses where the sample thickness is necessarily larger from any liquid and isolating membranes used in the experiment.

In this case, Cerenkov loss effects due to the high STEM operating voltage used, or large sample thickness, were found to be minimal. However, these effects must be always be carefully considered especially since in-situ or in-operando analyses often use high STEM operating voltages to examine thick samples. A comprehensive study of Cerenkov effects on the valence EELS features of lithium ion batteries would provide needed guidance for future researchers.

Valence EELS analysis would also promote further studies on beam sensitive materials. The abilities of having interpretable signal with extremely small acquisition times means enabling EELS studies with very small electron dosages. The small dosage would minimize structural beam damage and any beam-induced reactions. At the same time, smaller acquisition times essentially improve temporal resolution of EELS. As a result, dynamic time-resolved studies (e.g. in-situ and in-operando lithiation experiments) would also benefit from valence EELS analysis.

This methodology in general would improve as the interband transitions of different LIB materials are more closely characterized through additional spectroscopy and DFT calculations, and the energy resolution of the EELS spectrum is improved by advanced field-emission sources or EELS monochromators.

CHAPTER 5

Structural & Chemical Interface Challenges in Additional Lithium Ion Battery Materials of Interest

5.1. Chapter Overview

This chapter contains summaries of collaborative projects that were undertaken in addition to the main research work described so far. The work included in this chapter further explores the theme of interfacial structure in battery materials probed through advanced electron microscopy analysis. In addition to studying chemical evolution in future high-capacity materials, the work in this chapter examines facets of the mechanical behavior of electrode materials and interfacial stability of solid-electrolyte materials. The expertise in materials and techniques developed in the rest of the dissertation enabled the success of the collaborations discussed here.

5.2. Exploring Lithium-Cobalt-Nickel Oxide Spinel Electrodes for ≥3.5 V Li-Ion Cells

As previously described in Chapter 1, layered intercalation materials provide high cycling performance but have limited charge capacities due to structural instabilities caused by significant lithium removal (e.g. >0.5 Li units in $LiCoO_2$). However, substitution of different transition metals can tune the crystal structure to form integrated layered and spinel structural regions, improving stability at high levels of delithiation.[101,164,105]

Alloying of small amounts of nickel into $LiCoO_2$ to form $LiCo_{1-x}Ni_xO_2$ ($0 \leq x \leq 2$) introduces a spinel phase to the normally layered structure, thus improving the stability with deeper levels of lithium removal.[165] However, the complete structural behavior of the $LiCo_{1-x}Ni_xO_2$ is not fully understood, such as the dependence of the crystal structure on the synthesis temperature. Determining the structural phase diagram is challenging due to the structural similarity between layered $LiCoO_2$ and spinel $Li_2Co_2O_4$. Specifically, the oxygen lattice structure in the spinel and layered phases results in identical XRD patterns that makes them indistinguishable to bulk characterization.[166] Therefore, a combination of TEM, high-resoution XRD, and electrochemical analysis was carried out in order to elucidate the local structure of the $LiCo_{1-x}Ni_xO_2$ materials at two different synthesis conditions: low temperature (400°C) and high temperature (800°C).

The combined analyses showed that $LiCoO_2$ synthesized at the lower temperature contains a mixed layered and spinel crystal structure. The identification of these phases using HRTEM and FFT analysis is shown in Figure 5.1. However, substituting Co with Ni to form $LiCo_{1-x}Ni_xO_2$ ($x = 0.1, 0.2$) promotes the formation of primarily the spinel phase at the low temperature synthesis condition, as based on the electrochemistry and voltage profiles. Increasing the synthesis temperature of $LiCo_{1-x}Ni_xO_2$ ($x = 0.1, 0.2$)

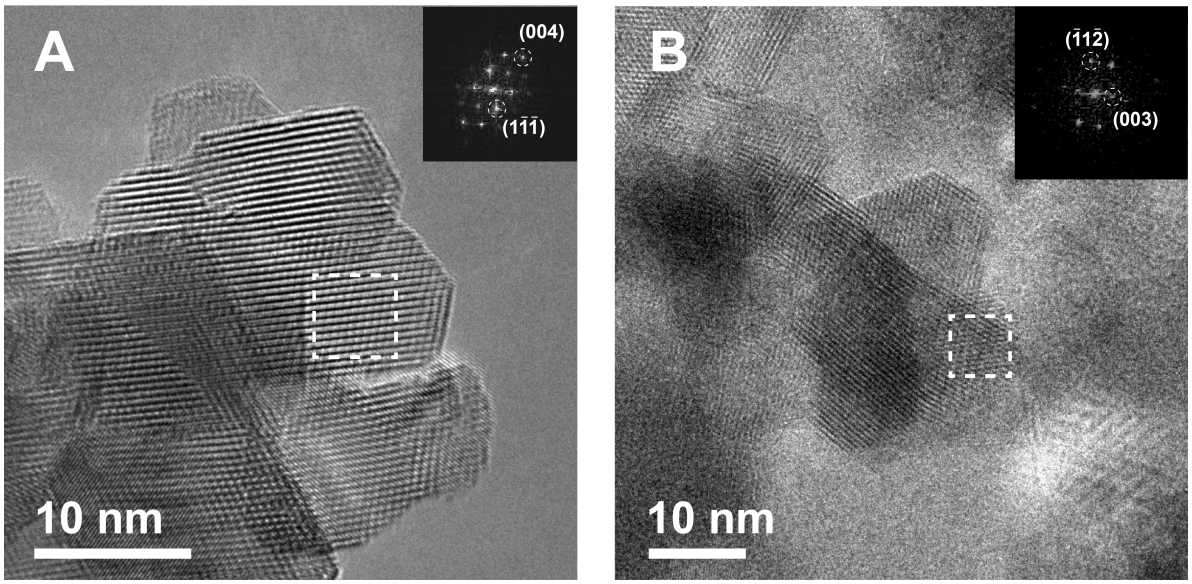

Figure 5.1. HRTEM and FFT images of a $LiCoO_2$ sample synthesized at 400°C, showing crystalline regions of (A) spinel and (B) layered structures.

to 600°C and 800°C showed more formation of the layered structure, which were again identified via TEM and electrochemical analysis.

Ultimately, this work provided further insight into the $LiCo_{1-x}Ni_xO_2$ material system and the field of intergrown layered/spinel structures for cathodes with higher cycling stability and operating potentials. Tuning the composition of the transition metals in the structure, along with synthesis temperature, outlines a method of controlling the prominence of layered and spinel structures and thus tuning electrochemical performance.

Further details of this work can be found in Reference [39].

5.3. The Mechanical Response of $Li_xMn_2O_4$ Interfaces to Electrochemical Delithiation

Lithiation and delithiation of intercalation electrodes causes expansion and contraction of the crystalline lattice that comes with associated stresses and strains. As a result,

the repeated and extended cycling of the electrode materials can lead to fracture and mechanical failure of the active material, resulting in capacity loss.[167,168,65,169] Understanding the relationship between stress, strain, and the resulting mechanical fracture is necessary for determining failure mechanisms and designing new battery systems with improved cycling performance. $LiMn_2O_4$ (LMO) is an insertion electrode with spinel structure, and its stress-strain response to lithiation and delithiation was previously studied to show an asynchronous response to changing lithium content. In particular, a significant stress build-up was observed in the material before an observed lattice expansion.[170]

In this work, the mechanism of stress build-up and the resulting mechanical fracture in LMO cathode materials was further examined. A combined DFT and SEM/TEM approach was utilized to predict the surface planes in LMO with the largest stress build-up during delithiation and to relate this stress buildup to the observed crystallographic orientation of particle fracture.

The surface stresses of the (111) and (001) planes at various stages of delithiation were calculated via DFT. These calculations suggested that the (001) surface had the largest increase in tensile stress at the surface as more lithium atoms were extracted from the crystal lattice. However, this (001) surface stress does not mean there would be fracture along the [001] crystallographic direction. To determine this crack orientation, cross section samples were prepared from cracked regions in particles and examined using EBSD and TEM. Figure 5.2 shows this analysis. Overall, both techniques showed significant cracking along the {111} planes in the sample. The inverse pole figure (IPF) analysis of Figure 5.2c shows a strong <111> crystallographic orientation in the x and y sample directions which are parallel and perpendicular to the particle cracks. Direct HRTEM

imaging of the cracked region, and consequent FFT analysis also show the particle cracking along the {111} planes as seen in Figure 5.2C,D.

Overall, this study furthers the body of knowledge regarding the mechanical behavior of LMO in order to aid in the design of future intercalation electrode materials with improved mechanical stability and longer cycling lifetimes.

This work is from: Warburton, R., Castro, F.C., Madsen, K., Deshpande, S., Bassett, K.L., Gewirth, A.A., Dravid, V.P., & Greeley, J.. "The Mechanical Response of $Li_xMn_2O_4$ Interfaces to Electrochemical Delithiation", *in preparation.*

5.4. Understanding the Effect of Interlayers at the Thiophosphate Solid Electrolyte/Lithium Interface for All-Solid-State Li Batteries

Lithium ion batteries require improvements to cycling stability and charge capacity– but also safety. A significant challenge facing the safety of lithium ion batteries is the use of liquid electrolytes which offer high ionic conductivity but are highly flammable, which lead to fires if there is any significant mechanical or chemical failure in the battery.[171,30] Solid electrolytes, on the other hand, are non-flammable and remove this safety issue entirely. However, they typically demonstrate lower ionic conductivities than liquid electrolytes and introduce transport barriers at the solid-solid interfaces between electrolyte and electrode.[172–174]

Thiophosphate-based solid electrolytes, namely found in $Li_7P_3S_{11}$ (LPS) and $Li_{10}GeP_2S_{12}$(LGPS), are promising materials in the field because their bcc sulfur sublattice enables ionic conductivites competitive with liquid electrolytes.[175–177]. Unfortunately, they also have more narrow electrochemical stability windows and are reduced when in

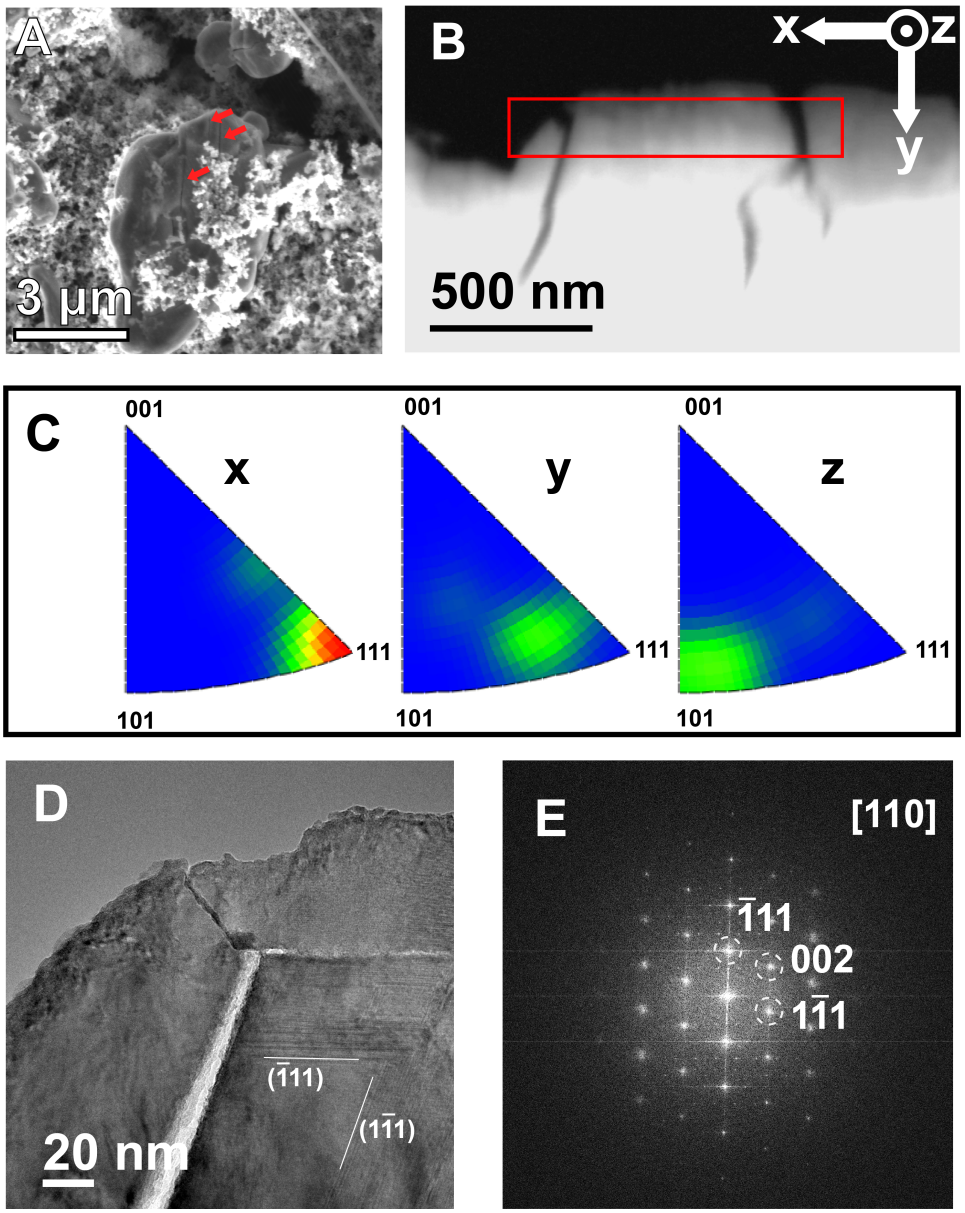

Figure 5.2. Determination of LMO Crack Orientation. (A) SEM image of cracked LMO particle. Red arrows highlight the location of cracking. (B) SEM image of cross-section sample extracted from the particle in A. The red box highlights the EBSD analysis region. The x,y, and z axes describe the sample orientation directions for EBSD analysis. (C) EBSD IPFs for the x,y, and z sample directions. (D) HRTEM image of the cracked region. This area corresponds to the left-most region analyzed via EBSD as marked in B. The {111} planes are marked. (E) FFT of sample region in D where {111} planes are marked.

contact with Li metal electrodes, forming insulating decomposition products. Naturally, introducing an interfacial layer between the solid electrolyte and electrode could help ameliorate the stability issues by removing direct anode-solid electrolyte contact and controlling the surface morphology. This work evaluates the effect of having Si interfacial layers between a LPS solid electrolyte and a lithium metal anode.

Cyclic voltammetry showed that lithium dendrites form in a bare LPS/Li interface after only 2-3 CV cycles, and cells with this interface morphology demonstrate poor electrochemical performance overall. In contrast, coating the LPS with a 20 nm Si interlayer and a 30 nm Au encapsulating layer results in a LPS/Si-Au/Li system with no significant degradation in electrochemical performance after 30 CV cycles. Electrochemical impedance spectroscopy analysis of a bare LPS/Li interface showed a two-fold increase in interfacial impedance after a single CV cycle.

STEM imaging and spectroscopy was used to observe the morphology evolution of the LPS/SiAu interface structure before and after cycling until cell shorting, as summarized in Figure 5.3. The main challenge is identifying the Si layer against the LPS electrode, as they have a similar average atomic number and provide little contrast in phase contrast or diffraction contrast TEM, and HAADF STEM imaging modes. HAADF STEM imaging clearly revealed the Au layer regions in both cases. EDS mapping followed by careful post-processing revealed the Si interlayer below the Au layer, and confirmed the expected morphology. However, extended cycling showed significant decomposition of the interlayer structure. Changes to the morphology of the Au layer were clearly seen in the HAADF image in Figure 5.3B, with EDS mapping showing similar distributions of Si.

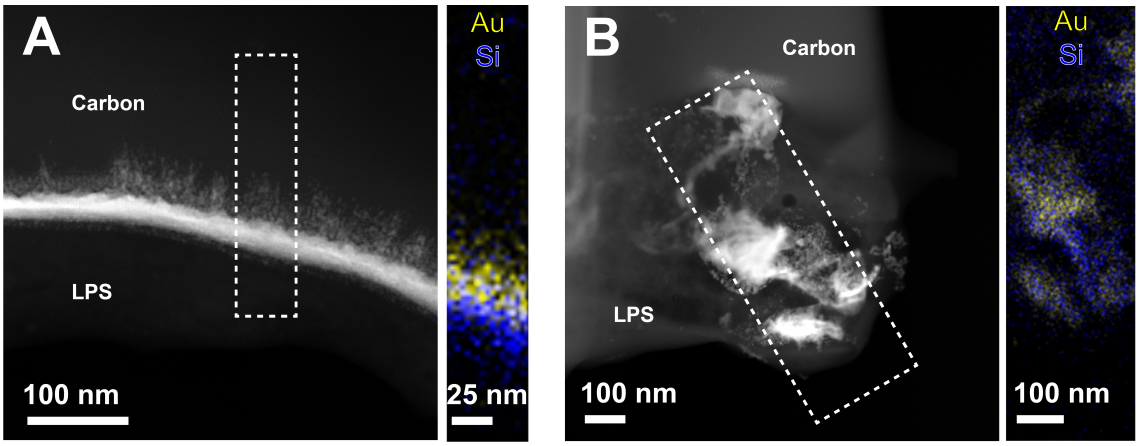

Figure 5.3. STEM Analysis of LPS/Si/Au. (A) HAADF STEM image of the (A) pristine LPS/Si/Au structure and (B) LPS/Si/Au structure after cycling. The white box in both images shows the EDS mapping region. The subfigure to the right of A, B shows the EDS map of Si and Au interlayers.

This observation is consistent with a rough surface seen via SEM and the formation of Li_2S by the surface via XPS.

Overall, introducing interlayers to the solid electrolyte/electrode interface improved interfacial stability and overall battery performance. However, further strategies are needed to maintain the structure of these interlayers and minimize the formation of reaction products which contribute to significant interfacial impedance.

This work is from: Sang, L., Bassett, K.L., Castro F.C., Young, M.J., Chen, L., Haasch, R.T., Elam, J.W., Dravid, V.P., Nuzzo, R.G., & Gewirth, A.A. "Understanding the Effect of Interlayers at the Thiophosphate Solid Electrolyte/Lithium Interface for All-Solid-State Li Batteries", Chem. Mater., 2018, *under review.*

CHAPTER 6

Closing Remarks

6.1. Summary and Conclusions

The research presented in this dissertation focused on studying alternative materials chemistries and structurally advanced materials for lithium ion batteries. Nearly all the materials systems were based on transition-metal oxides, highlighting a materials class capable of showing a varying range of properties and electrochemical phenomena within the field of lithium ion batteries. The tunability of their structure and chemistry enables oxides to be used both as anode and cathode materials, and the hope is that lessons learned in one particular system will provide insight into the more general class of oxides. Moreover, the same characterization techniques can be utilized to examine structural and chemical evolution in related systems under varying electrochemical conditions.

Several conclusions can be drawn based on the findings presented in this dissertation. With respect to the conversion reaction materials, the multilayer architecture provides much needed structural stability upon lithiation and delithiation. This is evident when comparing the structure evolution and volume expansion to the NiO/Ni nanowire, which showed significant volume expansion in addition to bending and buckling in the region unsupported by Ni. However, this structure also forms many inhomogeneities in both chemical state and elemental distribution, after just a single lithiation step. The dynamic properties were not fully characterized here and it is likely that these inhomogeneities

complicate their lifecycle evolution. Moreover, the field of conversion reaction materials seems to be stalled by their many complications, compared to alternative materials systems like silicon and lithium metal which boast much larger theoretical capacities and lower electrode potentials. Both sub-fields are still actively researched and silicon-based anode materials are beginning to enter the market as a commercialized technology through start-up companies like Sila Nanotechnologies & SiNode Systems. Conversion materials likely need to find a niche where the difficulty of controlling the chemistry is minimized or not as important. Structural control, like the multilayer architecture, is also likely needed for these materials, but through processing methods with higher through-put and easier manufacturability.

The possibility of oxygen electrochemistry to increase the charge capacity of either anode or cathode materials is definitely a promising route towards improving upon already commercialized intercalation materials. However, the work on $Li_{2-x}IrO_3$ showed that oxygen oxidation likely only contributed to charge compensation above 4 V vs. Li/Li^+potentials. This complicates use in a battery as many liquid electrolytes are unstable at such a high potential, and quickly result unwanted side reactions with lithium and capacity loss after few electrochemical cycles. Moreover, the EELS results suggest commensurate oxygen loss with the oxygen electrochemistry. The two behaviors must ideally be decoupled to take full advantage of the added charge capacity.

Lastly, the valence EELS analysis presented here enables additional routes to study beam sensitive materials and dynamic reactions, thanks to its high signal-to-background features at minimal acquisition times. Moreover, its demonstrated ability to improve mapping contrast between a material like $LiCoO_2$ and carbonaceous species make it especially

useful for looking at battery materials mixed into the necessary electrode slurrys, which contain multiple carbonaceous species. The main drawback to the valence EELS, at least in this discussion, is that compound-level information is provided, and not elemental-level information (e.g. the maps represent $LiCoO_2$ distribution, not Co or O distribution). This should only improve as more studies are done on the electronic structure of battery materials that give rise to the observed interband transitions in the valence EELS region, and monochromator technology improves the achievable EELS energy resolution.

6.2. Future Work

6.2.1. Research Directions for Battery Materials

Lithium ion battery materials play an important role for technology and sustainability in our society, and and any material for lithium ion batteries must be consistent with these ideals. Materials need to be sustainable, cost-effective, and also need to be processed in ways largely compatible with current manufacturing methods.[178,179] This is especially true for conversion materials that, in addition to challenges with their chemistry, face uncertainty with respect to cost-effectiveness and manufacturability.

To that end, one branch of research that seems effective is improving structure and chemistry control via synthetic methods, or forming composite materials, rather than imposing multilayer structures through complex deposition mechanisms. This would echo much of the work on silicon anodes to control the volume expansion and minimize the effects of high stress and strain during charge cycles.[180,181] Otherwise, making nanoscale layered structures puts battery materials more in the realm of advanced semiconductors for computer chips than cost-effective and powder-processed battery materials. For this

reason, exploring Li-rich materials and oxygen electrochemistry is a good research direction as it expands the realm of possibilities in already commercialized electrode materials.

6.2.2. Research Directions in Electron Microscopy

There are several important methods in which improvements in electron microscopy capabilities would lead to additional discoveries related to the nanoscale (and smaller) phenomena in battery materials. One of the largest challenges comes with the sensitivity of lithium ion battery materials to the intense energy flux from the electron beam during imaging or spectroscopy. This is especially true now that aberration corrected TEMs can achieve sub-angstrom resolution, but with huge electron doses per unit area. Thus, even though it may be possible to do atomic resolution imaging and chemical analysis of lithium ion battery materials, the amount of beam damage to the sample can be massive.

Future work in the field of electron microscopy must continue to find new ways of studying materials at the atomic scale while minimizing the electron dosage. Part of this comes with improved hardware – new direct electron detectors, such as the Gatan K3 camera, are sensitive enough to detect single electrons and acquire extremely low-dose images that would minimize sample damage. Furthermore, they would improve imaging techniques such as Annular Bright-Field Imaging, which utilizes a very small range of electron scattering to form an image where light elements like oxygen and perhaps lithium can be imaged.[182] The small collection angle produces very low signal images, which would be improved by better detectors. The field of machine learning is also starting to have an impact on this challenge, as new methods of using reduced-dose acquisition combined with data reconstruction algorithms are being actively developed to dramatically reduce beam

damage to samples with minimal losses in data fidelity.[183,184] Finally, cryo-TEM techniques were recently applied to lithium ion battery materials to stabilize the structure of lithium under the electron beam, which could open up new pathways to characterization of the structure and chemistry in beam-sensitive samples.[185]

Outside of dosage-lowering methodologies that need to be developed, new methods for studying reaction mechanisms and chemistry in lithium ion battery materials would be wildly beneficial. The dynamic TEM characterization shown in this disseration was based on in-situ techniques that provided little quantitative electrochemical information. In-operando techniques, on the other hand, would allow for imaging and analysis of dynamic phenomena during charge or discharge of materials while also providing information about the electrode current and potential during testing. These require the presence of liquid electrolytes in more advanced fluidic cell TEM holders, which increase the effective sample thickness and can form several beam-induced decomposition products that hinder analysis. For this reason, much of the liquid-cell work has been limited to larger micro-scale phenomena.[147,186] Advances in this field require the kind of low-dose solutions already described in addition to new holder designs to introduce liquid electrolytes into the TEM with minimal decomposition and artifacts.

TEM techniques essentially provide the spatial resolution needed to image each kind of element found inside lithium ion battery materials. What is now needed are new methods to improve the sensitivity and interpretability of the acquired data.

Bibliography

1. *Voltaic Pile* 2014. http://search.credoreference.com/content/entry/este/voltaic_pile/0.
2. Armand, M & Tarascon, J.-M. Building better batteries. *Nature* **451,** 652–657. ISSN: 0028-0836 (2008).
3. Palacín, M. R. Recent advances in rechargeable battery materials: A chemist's perspective. *Chemical Society Reviews* **38,** 2565–2575. ISSN: 03060012 (2009).
4. Mizushima, K., Jones, P. C., Wiseman, P. J. & Goodenough, J. B. Li_xCoO_2 ($0 < x \leq 1$): A new cathode material for batteries of high energy density. *Solid State Ionics* **3-4,** 171–174. ISSN: 01672738 (1981).
5. Ozawa, K. Lithium-ion rechargeable batteries with $LiCoO_2$ and carbon electrodes: the $LiCoO_2$/C system. *Solid State Ionics* **69,** 212–221. ISSN: 01672738 (1994).
6. Whittingham, M. S. Lithium batteries and cathode materials. *Chemical Reviews* **104,** 4271–4301. ISSN: 00092665 (2004).
7. Scrosati, B. & Garche, J. Lithium batteries: Status, prospects and future. *Journal of Power Sources* **195,** 2419–2430. ISSN: 03787753 (2010).
8. Nitta, N. & Yushin, G. High-capacity anode materials for lithium-ion batteries: Choice of elements and structures for active particles. *Particle and Particle Systems Characterization* **31,** 317–336. ISSN: 15214117 (2014).
9. Manthiram, A. An Outlook on Lithium Ion Battery Technology. *ACS Central Science.* doi:10.1021/acscentsci.7b00288 (2017).
10. Li, M., Lu, J., Chen, Z. & Amine, K. 30 Years of Lithium-Ion Batteries. *Advanced Materials* **1800561,** 1800561. ISSN: 09359648 (2018).
11. Kwade, A. *et al.* Current status and challenges for automotive battery production technologies. *Nature Energy* **3.** ISSN: 2058-7546. doi:10.1038/s41560-018-0130-3. https://www.nature.com/articles/s41560-018-0130-3 (2018).
12. Kraytsberg, A., Ein-Eli, Y., Kraytsberg, A. & Ein-Eli, Y. Higher, stronger, better ... A review of 5 volt cathode materials for advanced lithium-ion batteries. *Advanced Energy Materials* **2,** 922–939. ISSN: 16146832 (2012).
13. Zaghib, K. *et al.* Review and analysis of nanostructured olivine-based lithium recheargeable batteries: Status and trends. *Journal of Power Sources* **232,** 357–369. ISSN: 03787753 (2013).

14. Girishkumar, G., McCloskey, B., Luntz, A. C., Swanson, S. & Wilcke, W. Lithium-air battery: Promise and challenges. *Journal of Physical Chemistry Letters* **1,** 2193–2203. ISSN: 19487185 (2010).
15. Cabana, J., Monconduit, L., Larcher, D. & Palacín, M. R. Beyond intercalation-based Li-ion batteries: The state of the art and challenges of electrode materials reacting through conversion reactions. *Advanced Materials* **22.** ISSN: 09359648. doi:10.1002/adma.201000717 (2010).
16. Zhang, W. J. A review of the electrochemical performance of alloy anodes for lithium-ion batteries. *Journal of Power Sources* **196,** 13–24. ISSN: 03787753 (2011).
17. McDowell, M. T. *et al.* In situ TEM of two-phase lithiation of amorphous silicon nanospheres. *Nano Letters* **13,** 758–764. ISSN: 15306984 (2013).
18. Xu, W. *et al.* Lithium metal anodes for rechargeable batteries. *Energy Environ. Sci.* **7,** 513–537. ISSN: 1754-5692 (2014).
19. Goriparti, S. *et al.* Review on recent progress of nanostructured anode materials for Li-ion batteries. *Journal of Power Sources* **257,** 421–443. ISSN: 03787753 (2014).
20. Ramakumar, S, Deviannapoorani, C, Dhivya, L, Shankar, L. S. & Murugan, R. Progress in Materials Science Lithium garnets : Synthesis , structure , Li^+ conductivity , Li^+ dynamics and applications. *Progress in Materials Science* **88,** 325–411. ISSN: 0079-6425 (2017).
21. Huston, R. & Butler, J. N. The standard potential of the lithium electrode in aqueous solutions. *Journal of Physical Chemistry* **72,** 4263–4264. ISSN: 00223654 (1968).
22. Dahn, J. R. *et al.* Carbons and graphites as substitutes for the lithium anode. *Industrial chemistry library* **5,** 1 (1994).
23. Liu, C., Neale, Z. G. & Cao, G. Understanding electrochemical potentials of cathode materials in rechargeable batteries. *Materials Today* **19,** 109–123. ISSN: 18734103 (2016).
24. Nitta, N., Wu, F., Lee, J. T. & Yushin, G. Li-ion battery materials: Present and future. *Materials Today* **18,** 252–264. ISSN: 18734103 (2015).
25. Palacín, M. R. & De Guibert, A. Batteries: Why do batteries fail? *Science* **351.** ISSN: 10959203. doi:10.1126/science.1253292 (2016).
26. Dell, R. *Understanding batteries* ISBN: 1-84755-222-6 (Royal Society of Chemistry, Cambridge, 2001).
27. Tarascon, J. & Armand, M. Issues and Challenges Facing Rechargeable Lithium Batteries. *Nature* **414,** 359–367 (2001).
28. Zheng, J. *et al.* Li- and Mn-Rich Cathode Materials: Challenges to Commercialization. *Advanced Energy Materials,* 1601284. ISSN: 16146832 (2016).
29. Tsivadze, a. Y., Kulova, T. L. & Skundin, a. M. Fundamental problems of lithium-ion rechargeable batteries. *Protection of Metals and Physical Chemistry of Surfaces* **49,** 145–150. ISSN: 2070-2051 (2013).

30. Quartarone, E & Mustarelli, P. Electrolytes for solid-state lithium rechargeable batteries: recent advances and perspectives. *Chemical Society Reviews* **40,** 2525–2540. ISSN: 1460-4744 (2011).
31. Braga, M. H., Grundish, N. S., Murchison, A. J. & Goodenough, J. B. Alternative Strategy for a Safe Rechargeable Battery. *Energy Environ. Sci.* **10,** 0–6. ISSN: 1754-5692 (2016).
32. Larcher, D & Tarascon, J.-M. Towards greener and more sustainable batteries for electrical energy storage. *Nature chemistry* **7,** 19–29. ISSN: 1755-4349 (2015).
33. Ager-Wick Ellingsen, L. *et al.* Nanotechnology for environmentally sustainable electromobility Life-cycle assessment of EVs. *Nature Publishing Group* **11,** 1039–1051. ISSN: 1748-3387 (2016).
34. Deng, J., Luo, W. B., Chou, S. L., Liu, H. K. & Dou, S. X. Sodium-Ion Batteries: From Academic Research to Practical Commercialization. *Advanced Energy Materials* **1701428,** 1–17. ISSN: 16146840 (2017).
35. Xiang, X., Zhang, K. & Chen, J. Recent advances and prospects of cathode materials for sodium-ion batteries. *Advanced Materials* **27,** 5343–5364. ISSN: 15214095 (2015).
36. Xu, C *et al.* Secondary batteries with multivalent ions for energy storage. *Scientific reports* **5,** 14120. ISSN: 2045-2322 (2015).
37. Aurbach, D., Zinigrad, E., Cohen, Y. & Teller, H. A short review of failure mechanisms of lithium metal and lithiated graphite anodes in liquid electrolyte solutions. *Solid State Ionics* **148,** 405–416. ISSN: 01672738 (2002).
38. Agubra, V. & Fergus, J. Lithium ion battery anode aging mechanisms. *Materials* **6,** 1310–1325. ISSN: 19961944 (2013).
39. Lee, E. *et al.* Exploring Lithium-Cobalt-Nickel Oxide Spinel Electrodes for $\geq$3.5 V Li-Ion Cells. *ACS Applied Materials and Interfaces* **8,** 27720–27729. ISSN: 19448252 (2016).
40. Reimers, J. & Dahn, J. R. Electrochemical and In Situ X-Ray Diffraction Studies of Lithium Intercalation in Li_xCoO_2. *J. Electrochem. Soc.* **139,** 2–8 (1996).
41. Padhi, A., Nanjundaswamy, K. & Goodenough, J. Phospho-olivines as Positive-Electrode Materials for Rechargeable Lithium Batteries. *J. Electrochem. Soc.* **144,** 2–8 (1997).
42. Prosini, P. P., Lisi, M., Zane, D. & Pasquali, M. Determination of the chemical diffusion coefficient of lithium in $LiFePO_4$. *Solid State Ionics* **148,** 45–51. ISSN: 01672738 (2002).
43. Thackeray, M. M., Johnson, P. J., de Picciotto, L. A., Bruce, P. G. & Goodenough, J. B. Electrochemical extraction of lithium from $LiMn_2O_4$. *Materials Research Bulletin* **19,** 179–187. ISSN: 00255408 (1984).
44. Xia, Y. An Investigation of Lithium Ion Insertion into Spinel Structure Li-Mn-O Compounds. *Journal of The Electrochemical Society* **143,** 825. ISSN: 00134651 (1996).

45. Park, M., Zhang, X., Chung, M., Less, G. B. & Sastry, A. M. A review of conduction phenomena in Li-ion batteries. *Journal of Power Sources* **195,** 7904–7929. ISSN: 03787753 (2010).
46. Dahn J.R, Zheng T, Liu Y, X. J. Mechanisms for Lithium Insertion in Carbanaceous Materials. *Amercican Association for the Advancement of Science* **270,** 590–593 (1995).
47. Kamali, A. R. & Fray, D. J. Review on Carbon and Silicon Based Materials as Anode Materials for Lithium Ion Batteries. *Journal of New Materials for Electrochemical Systems* **13,** 147–160. ISSN: 14802422 (2010).
48. Chu, S. & Majumdar, A. Opportunities and challenges for a sustainable energy future. *Nature* **488,** 294–303. ISSN: 00280836 (2012).
49. Cano, Z. P. *et al.* Batteries and fuel cells for emerging electric vehicle markets. *Nature Energy* **3,** 279. ISSN: 2058-7546 (2018).
50. Li, H., Balaya, P. & Maier, J. Li-Storage via Heterogeneous Reaction in Selected Binary Metal Fluorides and Oxides. *Journal of The Electrochemical Society* **151,** A1878. ISSN: 00134651 (2004).
51. Tarascon, J.-M., Poizot, P., Laruelle, S., Grugeon, S. & Dupont, L. Nano-sized transition-metal oxides as negative-electrode materials for lithium-ion batteries. *Nature* **407,** 496–499. ISSN: 00280836 (2000).
52. Gao, X.-P. & Yang, H.-X. Multi-electron reaction materials for high energy density batteries. *Energy & Environmental Science* **3,** 174. ISSN: 1754-5692 (2010).
53. Wang, F. *et al.* Conversion Reaction Mechanisms in Lithium Ion Batteries: Study of the Binary Metal Fluoride Electrodes Conversion Reaction Mechanisms in Lithium Ion Batteries : Study of the Binary Metal Fluoride Electrodes. *J. Am. Chem.Soc* **133,** 18828–18836 (2011).
54. Luo, L., Wu, J., Xu, J. & Dravid, V. P. Atomic resolution study of reversible conversion reaction in metal oxide electrodes for lithium-ion battery. *ACS Nano* **8,** 11560–11566. ISSN: 1936086X (2014).
55. He, K. *et al.* Transitions from near-surface to interior redox upon lithiation in conversion electrode materials. *Nano Letters* **15,** 1437–1444. ISSN: 15306992 (2015).
56. Hu, R. *et al.* Dramatically enhanced reversibility of Li_2O in SnO_2-based electrodes: the effect of nanostructure on high initial reversible capacity. *Energy Environ. Sci.* **9,** 595–603. ISSN: 1754-5692 (2015).
57. Lin, D., Liu, Y. & Cui, Y. Reviving the lithium metal anode for high-energy batteries. *Nature Nanotechnology* **12,** 194–206. ISSN: 1748-3387 (2017).
58. Cheng, X. B. *et al.* A review of solid electrolyte interphases on lithium metal anode. *Advanced Science* **3,** 1–20. ISSN: 21983844 (2015).
59. Yan, K. *et al.* Ultrathin two-dimensional atomic crystals as stable interfacial layer for improvement of lithium metal anode. *Nano Letters* **14,** 6016–6022. ISSN: 15306992 (2014).

60. Zheng, G. *et al.* Interconnected hollow carbon nanospheres for stable lithium metal anodes. *Nature Nanotechnology* **9,** 618–623. ISSN: 17483395 (2014).
61. Qian, J. *et al.* High rate and stable cycling of lithium metal anode. *Nature Communications* **6.** ISSN: 20411723. doi:10.1038/ncomms7362 (2015).
62. Cheng, X. B., Zhang, R., Zhao, C. Z. & Zhang, Q. Toward Safe Lithium Metal Anode in Rechargeable Batteries: A Review. *Chemical Reviews* **117,** 10403–10473. ISSN: 15206890 (2017).
63. Zhao, J. *et al.* foil as an alternative to lithium metal anodes. **12,** 993–999 (2017).
64. Obrovac, M. N. & Chevrier, V. L. Alloy Negative Electrodes for Li-Ion Batteries. *Chemical Reviews* **114,** 11444–11502. ISSN: 0009-2665 (2014).
65. Liu, X. H. *et al.* Size-dependent fracture of silicon nanoparticles during lithiation. *ACS Nano* **6,** 1522–1531. ISSN: 19360851 (2012).
66. McDowell, M. T., Lee, S. W., Nix, W. D. & Cui, Y. 25th anniversary article: Understanding the lithiation of silicon and other alloying anodes for lithium-ion batteries. *Advanced Materials* **25,** 4966–4985. ISSN: 09359648 (2013).
67. Goldstein, J. *Scanning electron microscopy and x-ray microanalysis* 3rd ed.. ISBN: 0306472929 (Kluwer Academic/Plenum Publishers, New York, 2003).
68. Williams, D. B. & Carter, C. B. *Transmission Electron Microscopy: A Textbook for Materials Science* 2nd ed. ISBN: 978-0-387-76500-6. doi:10.1007/978-0-387-76501-3 (Springer US, 2009).
69. Reimer, L, Rennekamp, R, Fromm, I & Langenfeld, M. Contrast in the electron spectroscopic imaging mode of a TEM. *J. Microsc.* **162,** 3–14. ISSN: 13652818 (1991).
70. Fultz, B. & Howe, J. M. *The TEM and its Optics* 761. ISBN: 978-3-642-29760-1. doi:10.1007/978-3-642-29761-8 (2007).
71. Pennycook, S. J. Z-contrast stem for materials science. *Ultramicroscopy* **30,** 58–69. ISSN: 03043991 (1989).
72. Carter, C. B. & Williams, D. B. *Electron Diffraction and Phase Identification* 82–102. ISBN: 978-0-8493-7558-3. doi:doi:10.1201/9781420007800-c6. arXiv: arXiv:1011.1669v3. http://dx.doi.org/10.1201/9781420007800-c6 (2016).
73. Carter, C. B. & Williams, D. B. *X-Ray and EELS Imaging* 439–466. ISBN: 978-0-8493-7558-3. doi:doi:10.1201/9781420007800-c6. arXiv: arXiv:1011.1669v3. http://dx.doi.org/10.1201/9781420007800-c6 (2016).
74. Egerton, R. F. Electron Energy-Loss Spectroscopy in the TEM. *Reports on Progress in Physics* **72,** 16502. ISSN: 0034-4885 (2009).
75. Wang, F. *et al.* Chemical distribution and bonding of lithium in intercalated graphite: Identification with optimized electron energy loss spectroscopy. *ACS Nano* **5,** 1190–1197. ISSN: 19360851 (2011).
76. Krivanek, Ondrej L., Paterson, J. H. ELNES of 3d Transition-Metal Oxides. **32,** 313–318 (1990).

77. Graetz, J, Ahn, C. C., Yazami, R & Fultz, B. An Electron Energy-Loss Spectrometry Study of Charge Compensation in $LiNi_{0.8}Co_{0.2}O_2$. *Journal of Physical Chemistry B* **107,** 2887–2891. ISSN: 1520-6106 (2003).
78. Graetz, J., Ahn, C. C., Ouyang, H., Rez, P. & Fultz, B. White lines and d-band occupancy for the 3d transition-metal oxides and lithium transition-metal oxides. *Physical Review B - Condensed Matter and Materials Physics* **69,** 1–6. ISSN: 01631829 (2004).
79. Evmenenko, G. *et al.* Lithiation of multilayer Ni / NiO electrodes : criticality of nickel layer thicknesses on conversion reaction kinetics. *Physical Chemistry Chemical Physics* **19,** 20029–20039. ISSN: 1463-9076 (2017).
80. Reddy, M. V. *et al.* α-Fe_2O_3 Nanoflakes as an Anode Material for Li-Ion Batteries. *Advanced Functional Materials* **17,** 2792–2799. ISSN: 1616301X (2007).
81. Taberna, P. L., Mitra, S, Poizot, P, Simon, P & Tarascon, J.-M. High rate capabilities Fe_3O_4-based Cu nano-architectured electrodes for lithium-ion battery applications. *Nature materials* **5,** 567–573. ISSN: 1476-1122 (2006).
82. Gregorczyk, K. E., Liu, Y., Sullivan, J. P. & Rubloff, G. W. In Situ Transmission Electron Microscopy Study of Electrochemical Lithiation and Delithiation Cycling of the Conversion Anode RuO_2. *ACS Nano* **7,** 6354–6360 (2013).
83. Li, L., Meng, F. & Jin, S. High-Capacity Lithium-Ion Battery Conversion Cathodes Based on Iron Fluoride Nanowires and Insights into the Conversion Mechanism. *Nano Letters* **12,** 6030–6037. ISSN: 1530-6984 (2012).
84. Fister, T. T. *et al.* Real-time observations of interfacial lithiation in a metal silicide thin film. *Journal of Physical Chemistry C* **116,** 22341–22345. ISSN: 19327447 (2012).
85. Fister, T. T. *et al.* Lithium intercalation behavior in multilayer silicon electrodes. *Advanced Energy Materials* **4.** ISSN: 16146840. doi:10.1002/aenm.201301494 (2014).
86. Fister, T. T. *et al.* Dimensionally Controlled Lithiation of Chromium Oxide. *Chemistry of Materials* **28,** 47–54. ISSN: 15205002 (2016).
87. Evmenenko, G. *et al.* Morphological Evolution of Multilayer Ni/NiO Thin Film Electrodes during Lithiation. *ACS Applied Materials Interfaces* **8,** 19979–19986. ISSN: 1944-8244 (2016).
88. Hurst, S. J., Payne, E. K., Qin, L. & Mirkin, C. A. Multisegmented one-dimensional nanorods prepared by hard-template synthetic methods. *Angewandte Chemie - International Edition* **45,** 2672–2692. ISSN: 14337851 (2006).
89. Leapman, R. D. & Swyt, C. R. Separation of overlapping core edges in electron energy loss spectra by multiple-least-squares fitting. *Ultramicroscopy* **26,** 393–403. ISSN: 03043991 (1988).
90. Shuman, H. & Somlyo, A. Electron energy loss analysis of near-trace-element concentrations of calcium. *Science* **21,** 23–32 (1987).

91. Estradé, S *et al.* Distinguishing the core from the shell in MnO_x/MnO_y and FeO_x/MnO_x core/shell nanoparticles through quantitative electron energy loss spectroscopy (EELS) analysis. *Micron* **43,** 30–36. ISSN: 1878-4291 (2012).
92. Egerton, R. *Electron Energy-Loss Spectroscopy in the Electron Microscope* 3rd ed. ISBN: 978-1-4419-9582-7. doi:10.1007/978-1-4419-9583-4. http://link.springer.com/10.1007/978-1-4419-9583-4 (Springer US, Boston, MA, 2011).
93. Bard, A. J. *Electrochemical methods : fundamentals and applications* 2nd ed.. ISBN: 0471043729 (Wiley, New York, 2001).
94. Dickey, E. C. *et al.* Structure and bonding at Ni-ZrO_2 (cubic) interfaces formed by the reduction of a NiO-ZrO_2 (cubic) composite. *Microscopy And Microanalysis* **3,** 443–450. ISSN: 1431-9276 (1997).
95. Wang, C. M. *et al.* In situ transmission electron microscopy and spectroscopy studies of interfaces in Li ion batteries: Challenges and opportunities. *Journal of Materials Research* **25,** 1541–1547. ISSN: 0884-2914 (2010).
96. Wang, C.-M. In situ transmission electron microscopy and spectroscopy studies of rechargeable batteries under dynamic operating conditions: A retrospective and perspective view. *Journal of Materials Research* **30,** 326–339. ISSN: 0884-2914 (2015).
97. He, K. *et al.* Sodiation Kinetics of Metal Oxide Conversion Electrodes: A Comparative Study with Lithiation. *Nano Letters* **15,** 5755–5763. ISSN: 15306992 (2015).
98. Huang, J. Y. *et al.* In situ observation of the electrochemical lithiation of a single SnO2 nanowire electrode. *Science (New York, N.Y.)* **330,** 1515–1520. ISSN: 0036-8075 (2010).
99. Wang, C.-M. *et al.* In situ transmission electron microscopy observation of microstructure and phase evolution in a SnO_2 nanowire during lithium intercalation. *Nano letters* **11,** 1874–1880. ISSN: 1530-6992 (2011).
100. Zhong, L., Liu, Y., Han, W.-Q., Huang, J. Y. & Mao, S. X. In Situ Observation of Single-Phase Lithium Intercalation in Sub-25-nm Nanoparticles. *Advanced Materials* **1700236,** 1700236. ISSN: 09359648 (2017).
101. Thackeray, M. M. Lithiated Oxides for Lithium Ion Batteries. *Journal of The Electrochemical Society* **142,** 2558–2563 (1995).
102. Kikkawa, J. *et al.* Chemical States of Overcharged $LiCoO_2$ Particle Surfaces and Interiors Observed Using Electron Energy-Loss Spectroscopy. *The Journal of Physical Chemistry C* **119,** 15823–15830. ISSN: 1932-7447 (2015).
103. Aurbach, D. *et al.* On the capacity fading of $LiCoO_2$ intercalation electrodes: The effect of cycling, storage, temperature, and surface film forming additives. *Electrochimica Acta* **47,** 4291–4306. ISSN: 00134686 (2002).
104. Ohsaki, T. *et al.* Overcharge reaction of lithium-ion batteries. *Journal of Power Sources* **146,** 97–100. ISSN: 03787753 (2005).
105. Thackeray, M. M. *et al.* Li_2MnO_3-stabilized $LiMO_2$ (M = Mn, Ni, Co) electrodes for lithium-ion batteries. *Journal of Materials Chemistry* **17,** 3112. ISSN: 0959-9428 (2007).

106. Sathiya, M. *et al.* Reversible anionic redox chemistry in high-capacity layered-oxide electrodes. *Nature Materials* **12,** 827–835. ISSN: 1476-1122 (2013).
107. Sathiya, M *et al.* Origin of voltage decay in high-capacity layered oxide electrodes. *Nature materials* **14,** 230–8. ISSN: 1476-1122 (2015).
108. Li, B. *et al.* Understanding the Stability for Li-Rich Layered Oxide Li_2RuO_3 Cathode. *Advanced Functional Materials* **26,** 1330–1337. ISSN: 1616301X (2016).
109. Wang, J. *et al.* Lithium- and Manganese-Rich Oxide Cathode Materials for High-Energy Lithium Ion Batteries. *Advanced Energy Materials,* 1600906. ISSN: 16146832 (2016).
110. Phillips, P. J., Bareño, J., Li, Y., Abraham, D. P. & Klie, R. F. On the Localized Nature of the Structural Transformations of Li_2MnO_3 Following Electrochemical Cycling. *Advanced Energy Materials* **5,** 1–12. ISSN: 16146840 (2015).
111. Gu, M. *et al.* Probing the failure mechanism of nanoscale $LiFePO_4$ for Li-ion batteries. *Applied Physics Letters* **106,** 203902. ISSN: 0003-6951 (2015).
112. Rana, J. *et al.* Structural Changes in Li_2MnO_3 Cathode Material for Li-Ion Batteries. *Advanced Energy Materials* **4,** 1300998. ISSN: 16146832 (2014).
113. Luo, K. *et al.* Charge-compensation in 3d-transition-metal-oxide intercalation cathodes through the generation of localized electron holes on oxygen. *Nature Chemistry,* 1–17. ISSN: 1755-4330 (2016).
114. Seo, D.-h., Lee, J., Urban, A., Malik, R. & Kang, S. The Structual and chemical origin of the oxygen redox activity in layered and cation-disordered Li-excess cathode materials. *Nature Chemistry* **8,** 1–6. ISSN: 1755-4330 (2016).
115. Wang, R. *et al.* Atomic structure of Li_2MnO_3 after partial delithiation and relithiation. *Advanced Energy Materials* **3,** 1358–1367. ISSN: 16146832 (2013).
116. McCalla, E. *et al.* Visualization of O-O peroxo-like dimers in high-capacity layered oxides for Li-ion batteries. *Science* **350,** 1516–21. ISSN: 1095-9203 (2015).
117. Kresse, G. & Joubert, D. From ultrasoft pseudopotentials to the projector augmented-wave method. *Physical Review B* **59,** 1758–1775. ISSN: 1098-0121 (1999).
118. Dudarev, S. L., Botton, G., Savrasov, S. Y., Humphreys, C. J. & Sutton, A. P. Electron-energy-loss spectra and the structural stability of nickel oxide: An LSDA+U study. *Physical Review B* **57,** 1505–1509. ISSN: 1098-0121 (1998).
119. Sen, F. G. *et al.* Towards accurate prediction of catalytic activity in IrO_2 nanoclusters via first principles-based variable charge force field. *J. Mater. Chem. A* **3,** 18970–18982. ISSN: 2050-7488 (2015).
120. Heyd, J., Scuseria, G. E. & Ernzerhof, M. Hybrid functionals based on a screened Coulomb potential. *The Journal of Chemical Physics* **118,** 8207–8215. ISSN: 0021-9606 (2003).
121. Vinson, J., Rehr, J. J., Kas, J. J. & Shirley, E. L. Bethe-Salpeter equation calculations of core excitation spectra. *Physical Review B* **83,** 115106. ISSN: 10980121 (2011).

122. Wentzcovitch, P. G. *et al.* QUANTUM ESPRESSO: a modular and open-source software project for quantum simulations of materials. *Journal of Physics: Condensed Matter* **21,** 395502. ISSN: 0953-8984 (2009).
123. Gonze, X. *et al.* First-principles computation of material properties: the ABINIT software project. *Computational Materials Science* **25,** 478–492. ISSN: 09270256 (2002).
124. Kurata, H., Lefevre, E., Colliex, C. & Brydson, R. Electron-energy-loss near-edge structures in the oxygen K-edge spectra of transition-metal oxides. *Physical Review B* **47,** 763–768 (1993).
125. Grunes, L. A., Leapman, R. D., Wilker, C. N., Hoffmann, R. & Kunz, A. B. Oxygen K near-edge fine structure: An electron-energy-loss investigation with comparisons to new theory for selected 3d transition-metal oxides. *Physical Review B* **25,** 7157–7173. ISSN: 1098-6596 (1982).
126. Jiang, N. & Spence, J. C. H. Interpretation of oxygen K pre-edge peak in complex oxides. *Ultramicroscopy* **106,** 215–219. ISSN: 03043991 (2006).
127. Henderson, G. S., De Groot, F. M. F. & Moulton, B. J. A. X-ray Absorption Near-Edge Structure (XANES) Spectroscopy. *Reviews in Mineralogy & Geochemistry* **78,** 75–138. ISSN: 1529-6466 (2014).
128. Sohn, C. H. *et al.* Mixing between $J_{eff} = \frac{1}{2}$ and $\frac{3}{2}$ orbitals in Na_2IrO_3: A spectroscopic and density functional calculation study. *Physical Review B - Condensed Matter and Materials Physics* **88,** 1–5. ISSN: 10980121 (2013).
129. Gretarsson, H. *et al.* Crystal-field splitting and correlation effect on the electronic structure of A_2IrO_3. *Physical Review Letters* **110,** 076402. ISSN: 00319007 (2013).
130. Park, J. H. *et al.* Electronic aspects of the ferromagnetic transition in manganese perovskites. *Physical Review Letters* **76,** 4215–4218. ISSN: 10797114 (1996).
131. Yoshiya, M., Tanaka, I., Kaneko, K. & Adachi, H. First principles calculation of chemical shifts in ELNES / NEXAFS of titanium oxides. **3217** (1999).
132. J. Zaanen, G.A. Sawatzky, J. A. Band Gaps and Electronic Structure of Transition-Metal Compounds. *Physical Review Letters* **55,** 2674–2677. ISSN: 00319007 (1987).
133. Bisogni, V. *et al.* Ground-state oxygen holes and the metal-insulator transition in the negative charge-transfer rare-earth nickelates. *Nature Communications* **7,** 1–8. ISSN: 20411723 (2016).
134. Castro, F. C. & Dravid, V. P. Characterization of Lithium Ion Battery Materials with Valence Electron Energy-Loss Spectroscopy. *Microsc.Microanal.* 1–7 (2018).
135. Lu, J. *et al.* The role of nanotechnology in the development of battery materials for electric vehicles. *Nature Nanotechnology* **11,** 1031–1038. ISSN: 1748-3387 (2016).
136. Ellis, B. L., Lee, K. T. & Nazar, L. F. Positive Electrode Materials for Li-Ion and Li-batteries. *Chemistry of Materials* **22,** 691–714. ISSN: 08974756 (2010).
137. Tarascon, J.-M., Poizot, P, Laruelle, S, Grugeon, S & Dupont, L. Nano-sized transition-metal oxides as negative-electrode materials for lithium-ion batteries. *Nature* **407,** 496–499. ISSN: 00280836 (2000).

138. Mauchamp, V., Moreau, P., Ouvrard, G. & Boucher, F. Local field effects at Li K edges in electron energy-loss spectra of Li, Li_20 and LiF. *Physical Review B - Condensed Matter and Materials Physics* **77,** 1–9. ISSN: 10980121 (2008).
139. Mauchamp, V., Boucher, F. & Moreau, P. Electron energy-loss spectroscopy in the low-loss region as a characterization tool of electrode materials. *Ionics* **14,** 191–195. ISSN: 09477047 (2008).
140. Cosandey, F. in *Microscopy: Science, Technology, Applications, and Education* 1662–1666 (2010).
141. Jiang, N. & Spence, J. C. H. Core-hole effects on electron energy-loss spectroscopy of Li_2O. *Physical Review B* **69,** 115112. ISSN: 1098-0121 (2004).
142. Sigle, W., Amin, R., Weichert, K., van Aken, P. A. & Maier, J. Delithiation Study of $LiFePO_4$ Crystals Using Electron Energy-Loss Spectroscopy. *Electrochemical and Solid-State Letters* **12,** A151–A154. ISSN: 10990062 (2009).
143. Moreau, P. & Boucher, F. Revisiting lithium K and iron $M_{2,3}$ edge superimposition: The case of lithium battery material $LiFePO_4$. *Micron* **43,** 16–21. ISSN: 09684328 (2012).
144. Potapov, P. L., Zschech, E & Stöger-Pollach, M. Measuring the dielectric constant of materials from valence EELS. *Micron* **40,** 262–268 (2009).
145. Jiang, N. & Spence, J. C. H. Valence electron energy-loss spectroscopy study of $ZrSiO_4$ and ZrO_2. *Ultramicroscopy* **134,** 68–76 (2013).
146. Kikkawa, J & Takeda, S. Enhanced direct interband transitions in silicon nanowires studied by electron energy-loss spectroscopy. *Physical Review B* **75,** 245317 (2007).
147. Holtz, M. E. *et al.* Nanoscale imaging of lithium ion distribution during in situ operation of battery electrode and electrolyte. *Nano Letters* **14,** 1453–1459. ISSN: 15306992 (2014).
148. Boniface, M. *et al.* Nanoscale Chemical Evolution of Silicon Negative Electrodes Characterized by Low-Loss STEM-EELS. *Nano Letters,* 7381–7388. ISSN: 1530-6984 (2016).
149. Harks, P. P.R.M. L., Mulder, F. M. & Notten, P. H. L. In situ methods for Li-ion battery research: A review of recent developments. *Journal of Power Sources* **288,** 92–105. ISSN: 03787753 (2015).
150. Li, Z. *et al.* [100]-Oriented $LiFePO_4$ Nanoflakes toward High Rate Li-Ion Battery Cathode. *Nano Letters* **16,** 795–799 (2016).
151. Johnson, C. S., Li, N., Lefief, C., Vaughey, J. T. & Thackeray, M. M. Synthesis, Characterization and Electrochemistry of Lithium Battery Electrodes: $x\mathrm{Li_2MnO_3}$ $(1-x)$ $\mathrm{LiMn_{0.333}Ni_{0.333}Co_{0.333}O_2}$ $(0 \leq x \leq 0.7)$. *Chem. Mater.* **2,** 6095–6106 (2008).
152. Wu, J. S. *et al.* Imaging and elemental mapping of biological specimens with a dual-EDS dedicated scanning transmission electron microscope. *Ultramicroscopy* **128,** 24–31 (2013).
153. Abellan, P. *et al.* Factors influencing quantitative liquid (scanning) transmission electron microscopy. *Chem. Commun.* **50,** 4873–80. ISSN: 1364-548X (2014).

154. Mitchell, D. *Dave Mitchell's DigitalMicrograph Scripting Website* 2018. `http://www.dmscripting.com/contact.html`.
155. Zhu, X., Zhu, Y., Murali, S., Stoller, M. D. & Ruoff, R. S. Nanostructured Reduced Graphene Oxide/Fe_2O_3 Composite As a High-Performance Anode Material for Lithium Ion Batteries. *ACS Nano* **5,** 3333–3338. ISSN: 19360851 (2011).
156. Wang, Y. W., Kim, J. S., Kim, G. H. & Kim, K. S. Quantum size effects in the volume plasmon excitation of bismuth nanoparticles investigated by electron energy loss spectroscopy. *Applied Physics Letters* **88,** 143106. ISSN: 00036951 (2006).
157. Boniface, M. *et al.* Nanoscale Chemical Evolution of Silicon Negative Electrodes Characterized by Low-Loss STEM-EELS. *Nano Letters* **16,** 7381–7388. ISSN: 1530-6984 (2016).
158. Gu, L. *et al.* Band-gap measurements of direct and indirect semiconductors using monochromated electrons. *Physical Review B* **75,** 1–8 (2007).
159. Stöger-Pollach, M. Optical properties and bandgaps from low loss EELS : Pitfalls and solutions. *Micron* **39,** 1092–1110 (2008).
160. Horák, M. & Stöger-Pollach, M. The Čerenkov limit of Si, GaAs and GaP in electron energy loss spectrometry. *Ultramicroscopy* **157,** 73–78. ISSN: 18792723 (2015).
161. Stöger-Pollach, M., Laister, A. & Schattschneider, P. Treating retardation effects in valence EELS spectra for Kramers-Kronig analysis. *Ultramicroscopy* **108,** 439–444. ISSN: 03043991 (2008).
162. Malis, T., Cheng, S. & Egerton, R. EELS Log-Ratio Technique for Specimen-Thickness Measurement in the TEM. *Journal of Electron Microscopy Technique* **8,** 193–200 (1988).
163. Martin, J. M., Vacher, B., Ponsonnet, L. & Dupuis, V. Chemical bond mapping of carbon by image-spectrum EELS in the second derivative mode. *Ultramicroscopy* **65,** 229–238 (1996).
164. Bruce, P. G., Armstrong, A. R. & Gitzendanner, R. L. New intercalation compounds for lithium batteries: Layered $LiMnO_2$. *Journal of Materials Chemistry* **9,** 193–198. ISSN: 09599428 (1999).
165. Long, B. R. *et al.* Advances in Stabilizing 'Layered-Layered' $x Li_2MnO_3$-$(1-x)LiMO_2$ (M=Mn, Ni, Co) Electrodes with a Spinel Component. *Journal of the Electrochemical Society* **161,** A2160–A2167. ISSN: 0013-4651 (2014).
166. Rossen, E., Reimers, J. N. & Dahn, J. R. Synthesis and electrochemistry of spinel LT-$LiCoO_2$. *Solid State Ionics* **62,** 53–60. ISSN: 01672738 (1993).
167. Qi, Y., Xu, Q. & Van der Ven, A. Chemically Induced Crack Instability When Electrodes Fracture. *Journal of the Electrochemical Society* **159,** A1838–A1843. ISSN: 0013-4651 (2012).
168. Wang, D., Wu, X., Wang, Z. & Chen, L. Cracking causing cyclic instability of $LiFePO_4$ cathode material. *Journal of Power Sources* **140,** 125–128. ISSN: 03787753 (2005).

169. Zhang, Z. *et al.* Dual-doping to suppress cracking in spinel $LiMn_2O_4$: A joint theoretical and experimental study. *Physical Chemistry Chemical Physics* **18,** 6893–6900. ISSN: 14639076 (2016).
170. Çapraz, Ö. Ö., Bassett, K. L., Gewirth, A. A. & Sottos, N. R. Electrochemical Stiffness Changes in Lithium Manganese Oxide Electrodes. *Advanced Energy Materials* **7,** 1–7. ISSN: 16146840 (2017).
171. Li, J., Ma, C., Chi, M., Liang, C. & Dudney, N. J. Solid electrolyte: The key for high-voltage lithium batteries. *Advanced Energy Materials* **5,** 1–6. ISSN: 16146840 (2015).
172. Wang, L.-p. *et al.* Ameliorating the Interfacial Problems of Cathode and Solid-State Electrolytes by Interface Modification of Functional Polymers. **1801528,** 1–8. ISSN: 16146832 (2018).
173. Kamaya, N. *et al.* A lithium superionic conductor. *Nature materials* **10,** 682–6. ISSN: 1476-1122 (2011).
174. Bachman, J. C. *et al.* Inorganic Solid-State Electrolytes for Lithium Batteries: Mechanisms and Properties Governing Ion Conduction. *Chemical Reviews* **116,** 140–162. ISSN: 15206890 (2016).
175. Yamane, H. *et al.* Crystal structure of a superionic conductor, $Li_7P_3S_{11}$. *Solid State Ionics* **178,** 1163–1167. ISSN: 01672738 (2007).
176. Seino, Y., Ota, T., Takada, K., Hayashi, A. & Tatsumisago, M. A sulphide lithium super ion conductor is superior to liquid ion conductors for use in rechargeable batteries. *Energy and Environmental Science* **7,** 627–631. ISSN: 17545706 (2014).
177. Kuhn, A., Duppel, V. & Lotsch, B. V. Tetragonal $Li_{10}GeP_2S_{12}$ and Li_7GePS_8-exploring the Li ion dynamics in LGPS Li electrolytes. *Energy and Environmental Science* **6,** 3548–3552. ISSN: 17545692 (2013).
178. Li, J., Daniel, C. & Wood, D. Materials processing for lithium-ion batteries. *Journal of Power Sources* **196,** 2452–2460. ISSN: 03787753 (2011).
179. Wood, D. L., Li, J. & Daniel, C. Prospects for reducing the processing cost of lithium ion batteries. *Journal of Power Sources* **275,** 234–242. ISSN: 03787753 (2015).
180. Wu, H. & Cui, Y. Designing nanostructured Si anodes for high energy lithium ion batteries. *Nano Today* **7,** 414–429. ISSN: 17480132 (2012).
181. Zuo, X., Zhu, J., Müller-Buschbaum, P. & Cheng, Y. J. Silicon based lithium-ion battery anodes: A chronicle perspective review. *Nano Energy* **31,** 113–143. ISSN: 22112855 (2017).
182. Wen, Y., Shang, T. & Gu, L. Analytical ABF-STEM imaging of li ions in rechargeable batteries. *Microscopy* **66,** 25–38. ISSN: 20505701 (2017).
183. Hujsak, K., Myers, B. D., Roth, E., Li, Y. & Dravid, V. P. Suppressing electron exposure artifacts: An electron scanning paradigm with Bayesian machine learning. *Microscopy and Microanalysis* **22,** 778–788. ISSN: 14358115 (2016).

184. Hujsak, K. A., Roth, E. W., Kellogg, W., Li, Y. & Dravid, V. P. High speed/low dose analytical electron microscopy with dynamic sampling. *Micron* **108,** 31–40. ISSN: 09684328 (2018).
185. Li, Y. *et al.* Atomic structure of sensitive battery materials and interfaces revealed by cryo-electron microscopy. *Science* **358,** 506–510 (2017).
186. Mehdi, B. L. *et al.* Observation and quantification of nanoscale processes in lithium batteries by operando electrochemical (S)TEM. *Nano Letters* **15,** 2168–2173. ISSN: 15306992 (2015).

Vita

Fernando Cuauhtli Castro

EDUCATION

Northwestern University Evanston, IL

Ph.D. Materials Science and Engineering (2018)

Dissertation: Nanoscale Characterization of Oxide Materials and Interfaces for High Performance Lithium Ion Batteries

Advisor: Professor Vinayak P. Dravid

The University of Chicago Chicago, IL

B.S. Chemistry, with honors (2013)

Honors Thesis: Epitaxial Growth on Non-Planar Surfaces Using Nanoparticle Self-Assembly as a Model

Advisor: Professor Dmitri V. Talapin

AWARDS

Best Poster Award, Microscopy and Microanalysis Annual Meeting (2017)

Hierarchical Materials Cluster Program Fellowship, Northwestern University (2014)

ASU "Winter School on Electron Microscopy" Scholarship, Arizona State University (2014)

James Franck Institute Fellowship for Undergraduate Research, The University of Chicago (2011, 2012)

PUBLICATIONS

(10) Warburton, R.*, **Castro, F.C.***, Madsen, K., Deshpande, S., Bassett, K.L., Gewirth, A.A., Dravid, V.P., & Greeley, J., "The Mechanical Response of $Li_xMn_2O_4$ Interfaces to Electrochemical Delithiation", *in preparation.* (*equal contribution)

(9) Evmenenko, G., Fister, T.T., **Castro, F.C.**, Chen, X., Lee, B., Buchholz, D.B., Dravid, V.P., Fenter, P., & Bedzyk, M.J., "Initial Lithiation of NiO Thin Film Electrodes", *in preparation*

(8) Li, L., **Castro, F.C.**, Park, J.S., Li, H., Lee, E., Boyko, T.D., Freeland, J.W., Yao, Z., Fister, T.T., Vinson, J., Shirley, E.L., Wolverton, C., Cabana, J., Dravid, V.P., Thackeray, M.M., & Chan, M.K.Y. "Probing Electrochemically-Induced Structural Evolution and Oxygen Redox Reactions in Li-Rich Layered Cathode Materials", *in preparation.*

(7) Sang, L., Bassett, K.L., **Castro F.C.**, Young, M.J., Chen, L., Haasch, R.T., Elam, J.W., Dravid, V.P., Nuzzo, R.G., & Gewirth, A.A., "Understanding the Effect of Interlayers at the Thiophosphate Solid Electrolyte/Lithium Interface for All-Solid-State Li Batteries", Chem. Mater., 2018, *under review.*

(6) **Castro, F.C.**, & Dravid, V.P., "Characterization of Lithium Ion Battery Materials with Valence Electron Energy-Loss Spectroscopy", Microsc. Microanal., 2018, 24, 3, 214.
Additionally highlighted in Microscopy Today, 2018, 26, 4, 56.

(5) Nandwana, V., Ryoo, S.-R., Kanthala, S., Kumar, A., Sharma, A., **Castro, F.C.**, Li, Y., Hoffman, B., Lim, S., & Dravid, V.P., "Engineered Ferritin Nanocages as Natural Contrast Agents in Magnetic Resonance Imaging", RSC Advances, 2017, 7, 55, 34892

(4) Li, Y., Distefano, J.G., Murthy, A.A., Cain, J.D., Hanson, E.D., Li, Q., **Castro, F.C.**, Chen, X., & Dravid, V.P., "Superior Plasmonic Photodetectors Based on Au MoS_2 Core-Shell Heterostructures", ACS Nano, 2017, 11, 10, 10321

(3) Evmenenko, G., Fister, T.T., Buchholz, D.B., **Castro, F.C.**, Li, Q., Wu, J., Dravid, V.P., Fenter, P., & Bedzyk M.J., "Lithiation of Multilayer Ni/NiO Electrodes: Criticality of Nickel Layer Thicknesses on Conversion Reaction Kinetics", Phys. Chem. Chem. Phys., 2017, 19, 30, 20029

(2) Lee, E., Blauwkamp, J., **Castro, F.C.**, Wu, J., Dravid, V.P., Yan, P., Wang, C., Kim, S., Wolverton, C., Benedek, R., Dogan, F., Park, J.S., Croy, J.R., &

Thackeray, M.M., "Exploring Lithium-Cobalt-Nickel Oxide Spinel Electrodes for $\geq$ 3.5 V Li-Ion Cells", ACS Applied Materials & Interfaces, 2016, 8, 41, 27720

(1) Rupich, S.M., **Castro, F.C.**, Irvine, W.T.M., & Talapin, D.V., "Soft Epitaxy of Nanocrystal Superlattices", Nature Comm., 2014, 5, 5045

CONFERENCE PRESENTATIONS

(10) **Castro, F.C.**, & Dravid, V.P., "Analyzing Lithium Ion Battery Materials with Valence EELS", Microscopy and Microanalysis 2018 Meeting, Baltimore, MD, August 2018

(9) **Castro, F.C.**, Dravid, V.P., "Investigating the Electrochemical Reversibility of Transition Metal Oxide Conversion Materials Through STEM-EELS", Microscopy and Microanalysis 2017 Meeting, St. Louis, MO, August 2017 (*Best Poster Award*)

(8) Li, L, **Castro, F.C.**, Park, J.S., Lee, E., Freeland, J.W., Yao, Z., Fister, T.T., Vinson, J., Shirley, E.L., Wolverton, C., Dravid, V.P., Thackeray, M.M., Chan, M.K.Y., "Oxygen Redox Activity in Lithium-Rich Cathode Materials" Department of Energy, Office of Science, Energy Frontier Research Centers Principal Investigators' Meeting, Washington, D.C., July 2017

(7) **Castro, F.C.**, Li, Q., Wu, J., & Dravid, V.P., "Static and Dynamic S/TEM Analysis of Lithium Ion Battery Electrodes: Collaborative Battery Research at Northwestern University", Nanomaterials for Clean Energy and Environmental Sensors, Indo-US Science and Technology Forum, Bangalore, India, March 2017

(6) **Castro, F.C.**, Li, Q., Evmenenko, G., Buchholz, D.B., Wu, J., Bedzyk, M, Dravid, V.P., "Dynamics of Electrochemical Conversion of Nanoscale Metal-Metal Oxide Multilayer Architecture", Microscopy and Microanalysis 2016 Meeting, Columbus, OH, July 2016

(5) **Castro, F.C.**, Evmenenko, G., Li, Q., Buchholz, D.B., Wu, J., Bedzyk, M.J., & Dravid, V.P., "Lithium Conversion in Metal-Metal Oxide Multilayer Nano-Architectures", International Meeting on Lithium Ion Batteries, Chicago, IL, June 2016

(4) **Castro, F.C.**, Evmenenko, G., Li, Q., Buchholz, D.B., Wu, J., Bedzyk, M, Dravid, V.P., "Li-Ion Conversion Reaction Battery Anodes with Metal-Metal Oxide Multilayer Architecture", Materials Research Society Spring Meeting, Phoenix, AZ, March 2016

(3) **Castro, F.C.**, Li, Q, Wu, J., Evmenenko, G., Buchholz, D.B., Yao, Z, Wolverton, C., Fister, T.T., Bedzyk, M.J., Dravid, V.P., "Static and Dynamic Electron Microscopy of Conversion Electrode Materials In Li-Based Systems", Department of Energy, Office of Science, Energy Frontier Research Centers Principal Investigators' Meeting, Washington, D.C., October 2015

(2) Rupich, S.M., **Castro, F.C.**, Talapin, D.V., "Nanoparticle Epitaxy Using Self Assembled Nanoparticle Monolayers as a Substrate", Midstates Consortium for Math and Science: Undergraduate Research Symposium in the Physical Sciences, Mathematics and Computer Science, University of Chicago, Chicago, IL, November 2011

(1) Rupich, S.M., **Castro, F.C.**, Talapin, D.V., "Nanoparticle Epitaxy Using Self Assembled Nanoparticle Monolayers as a Substrate", Midwestern Symposium on Undergraduate Research in Chemistry, Michigan State University, East Lansing, Michigan, October 2011

PROFESSIONAL DEVELOPMENT

Management for Scientists and Engineers, Kellogg School of Management, Northwestern University, Evanston, IL (2018)

Skills and Careers in Science Writing, Medill School of Journalism & Science in Society Research Center, Northwestern University, Evanston, IL (2017)

Powering the Future: Innovation and Disruption in the Electric Power Sector, Institute for Sustainability and Energy, Northwestern University, Evanston, IL (2017)

Next Generation Electrochemistry Program, The Energy Initiative, University of Illinois at Chicago, Chicago, IL (2016)

RSG Research Communications Program, Northwestern University, Evanston, IL (2015)

Winter School on High Resolution Electron Microscopy, Arizona State University, Tempe, AZ (2015)

ACTIVITES

Graduate Student Leader, Center for Electrochemical Energy Science, Argonne National Laboratory, Argonne, IL (2014 - Present)

Executive Board Member, Northwestern Energy Technology Group, Northwestern University, Evanston, IL (2016 - 2018, Member 2015 - Present)

Graduate Speaker, Graduate Student Speakers Series Program, Northwestern University, Evanston, IL (2016 - 2017)

Mentor, Diversity and Inclusion Mentorship Program, The Graduate School, Northwestern University, Evanston, IL (2016)

Teaching Assistant (MSE 460: Electron Microscopy, MSE 466: Analytical Electron Microscopy), Department of Materials Science and Engineering, Northwestern University, Evanston, IL (2016)

Member, McCormick Graduate Leadership Council, McCormick School of Engineering, Northwestern University, Evanston, IL, (2014 - 2016)

Pen Pal, Letters to a Pre-Scientist, Northwestern University, Evanston, IL (2014 - 2015)

PROFESSIONAL MEMBERSHIPS

Microscopy Society of America

Microanalysis Society

Materials Research Society

NON-ACADEMIC PUBLICATIONS

(1) Castro, F.C., "Atomic Eyewitness: Illuminating the Battery Mystery", Helix Magazine, Science in Society, Northwestern University, November 24, 2017.